UC San Diego
UC San Diego Electronic Theses and Dissertations

Title
Etalon Arrays for Ultrafast Imaging and Spectrometry

Permalink
https://escholarship.org/uc/item/87h7v96j

Author
Huang, Eric

Publication Date
2018

Peer reviewed|Thesis/dissertation

UNIVERSITY OF CALIFORNIA, SAN DIEGO

Etalon Arrays for Ultrafast Imaging and Spectrometry

A dissertation submitted in partial satisfaction of the requirements for the degree

Doctor of Philosophy

In

Physics

By

Eric Huang

Committee in Charge:

        Professor Zhaowei Liu, Chair
        Professor David Kleinfeld, Co-Chair
        Professor Joseph Ford
        Professor Oleg Shpyrko
        Professor Douglas Smith

2018

The Dissertation of Eric Huang is

approved, and it is acceptable in quality and form for publication on

microfilm and electronically:

_____

_____

_____

_____

Co-chair

_____

Chair

University of California, San Diego

2018

EPIGRAPH

There are years that ask questions and years that answer.

-Zora Neale Hurston, *Their Eyes Were Watching God*

TABLE OF CONTENTS

LIST OF FIGURES

ACKNOWLEDGEMENTS

I would like to thank my advisor, professor Zhaowei Liu, for his role in my graduate studies. I have learned the value of never losing sight of what makes your research truly exciting. His endless supply of interesting project ideas and ability to always keep the big picture in mind have helped me throughout my stay here.

I would also like to thank my Ph. D. committee for their help in shaping my doctoral studies. Their comments and guidance have been greatly appreciated.

A huge debt of gratitude is also owed to my fellow group members. They have never hesitated to teach me in the lab when I needed help. I can only hope that in my time here, I have managed to help others in the same way.

Finally, I would like to thank my girlfriend, my family, and the people who call themselves my friends. I am fortunate to have had your support through this time in my life.

Chapter 2 and 3, in part, are reprints of the material as it appears in Scientific Reports, 2016, 6, 25240. Eric Huang, Qian Ma, Zhaowei Liu, "Ultrafast Imaging using Spectral Resonance Modulation". The dissertation author was the first author of this paper.

Chapter 5, in part, is a reprint of the material as it appears in Scientific Reports, 2017, 7, 25240. Eric Huang, Qian Ma, Zhaowei Liu, "Ultrafast Imaging using Spectral Resonance Modulation". The dissertation author was the first author of this paper.

VITA

2010   Bachelor of Science (Engineering Physics), Cornell University, Ithaca

2012   Master of Science (Physics), University of California, San Diego

2018   Ph. D. (Physics), University of California, San Diego

PUBLICATIONS

Bezryadina, Anna, Jinxing Li, Junxiang Zhao, Alefia Kothambawala, Joseph Ponsetto, Eric Huang, Joseph Wang, and Zhaowei Liu. 2017. "Localized Plasmonic Structured Illumination Microscopy with an Optically Trapped Microlens." *Nanoscale* 9 (39). Royal Society of Chemistry: 14907–12.

Ponsetto, Joseph L, Anna Bezryadina, Feifei Wei, Keisuke Onishi, Hao Shen, Eric Huang, Lorenzo Ferrari, Qian Ma, Yimin Zou, and Zhaowei Liu. 2017. "Experimental Demonstration of Localized Plasmonic Structured Illumination Microscopy." *ACS Nano* 11 (6). American Chemical Society: 5344–50.

Ma, Qian, Huan Hu, Eric Huang, and Zhaowei Liu. 2017. "Super-Resolution Imaging by Metamaterial-Based Compressive Spatial-to-Spectral Transformation." *Nanoscale* 9 (46). The Royal Society of Chemistry: 18268–74.

Huang, Eric, Qian Ma, and Zhaowei Liu. 2017. "Etalon Array Reconstructive Spectrometry." *Scientific Reports* 7: 40693. doi:10.1038/srep40693.

Huang, Eric, Qian Ma, and Zhaowei Liu. 2016. "Spectrum Engineering for Reconstructive Spectroscopy." In *CLEO: Applications and Technology*, AM1J--7.

Ma, Qian, Bahar Khademhosseinieh, Eric Huang, Haoliang Qian, Malina A Bakowski, Emily R Troemel, and Zhaowei Liu. 2016. "Three-Dimensional Fluorescent Microscopy via Simultaneous Illumination and Detection at Multiple Planes." *Scientific Reports* 6. Nature Publishing Group: 31445.

Huang, Eric, Qian Ma, and Zhaowei Liu. 2016. "Spectral Engineering for Reconstructive Imaging and Spectrometry (Conference Presentation)." In *Novel Optical Systems Design and Optimization XIX*, 9948:99480V.

Huang, E, Q Ma, and Z Liu. 2016. "Ultrafast Imaging Using Spectral Resonance Modulation." *Scientific Reports*. https://www.ncbi.nlm.nih.gov/pmc/articles/PMC4848519/.

Wei, Feifei, Dylan Lu, Hao Shen, Weiwei Wan, Joseph Louis Ponsetto, Eric Huang, and Zhaowei Liu. 2014. "Wide Field Super-Resolution Surface Imaging through Plasmonic Structured Illumination Microscopy." *Nano Letters* 14 (8). ACS Publications: 4634–39.

Shen, Hao, Eric Huang, Tapaswini Das, Hongxing Xu, Mark Ellisman, and Zhaowei Liu. 2014. "TIRF Microscopy with Ultra-Short Penetration Depth." *Optics Express* 22 (9). Optical Society of America: 10728–34.

ABSTRACT OF THE DISSERTATION

Etalon Resonance Sweeping for Ultrafast Imaging and Spectrometry

By

Eric Huang

Doctor of Philosophy

University of California, San Diego, 2018

Professor Zhaowei Liu, Chair
Professor David Kleinfeld, Co-Chair

High-speed imaging is invaluable in studying the dynamics of real-time ultrafast phenomena. However, conventional imaging techniques are ultimately limited by the electronic readout rate of the sensors. Compressive sensing (CS), a technique that allows for the reduction in the number of measurements needed to sample a signal, offers a method to bypass this limit. However, the lack of high-speed spatial light modulators provides a similar constraint on experimental realizations of CS cameras.

Etalons are optical structures that have unique and tunable transmission spectra. Ultrafast etalon array imaging uses an array of Fabry-Perot resonators to create a frequency dependent mask. This etalon array is combined with a method for high-speed frequency sweeping to generate high speed illumination patterns, which are used to sample an object. When combined with compressive sensing, it allows for a high-speed imaging capability. We demonstrate a proof of concept of this technology, showing high-speed tracking at a 12 ns exposure time and 25 kHz frame rate, and demonstrate an extension to high-speed particle tracking.

Also in this work, we demonstrate the capability for the etalon array to be used as a reconstructive spectrometer. The planar nature of the array allows for a spectrometer that is compact, robust, and potentially very inexpensive. We show a spectral resolution of 4 nm across a wide variety of visible wavelength bands, and explore extensions of the technology to hyperspectral imaging.

Chapter 1: Introduction

The focus of my thesis work is around the use of etalon arrays for reconstructive imaging and spectrometry. First, there will be a brief review of high speed imaging, and a short overview of the types of techniques that have been developed to address it. Secondly, there will be an overview of compressive sensing, its history, and the experimental compressive sensing technologies that have been developed. Finally, there will be a discussion of the requirements needed for a high-speed reconstructive imaging technology.

1.1 Review of high speed imaging technologies

Optical imaging is in use in nearly every field, from scientific uses such as astronomy, to industrial use in diagnostic and inspection tools, to more consumer-oriented fields such as digital photography. In common usage, much of the development has resolved around increases in resolution, such as the super-resolution techniques[1]–[6] that continuously driving us further and further past the diffraction limit. Much as in the way that an increase in spatial resolution allows for the ability to see details in an image that were previously hidden, however, increases in the imaging speed allow for the distinction of dynamics within the system being observed. Indeed, arguably the first 'film' ever recorded in 1878 was made to settle the question of whether a galloping horse ever lifted all four hooves off the ground [7]. As technology has developed, high-speed cameras and motion photography have expanded to allowed us to study in detail a huge variety of high-speed phenomena[8]–[14].
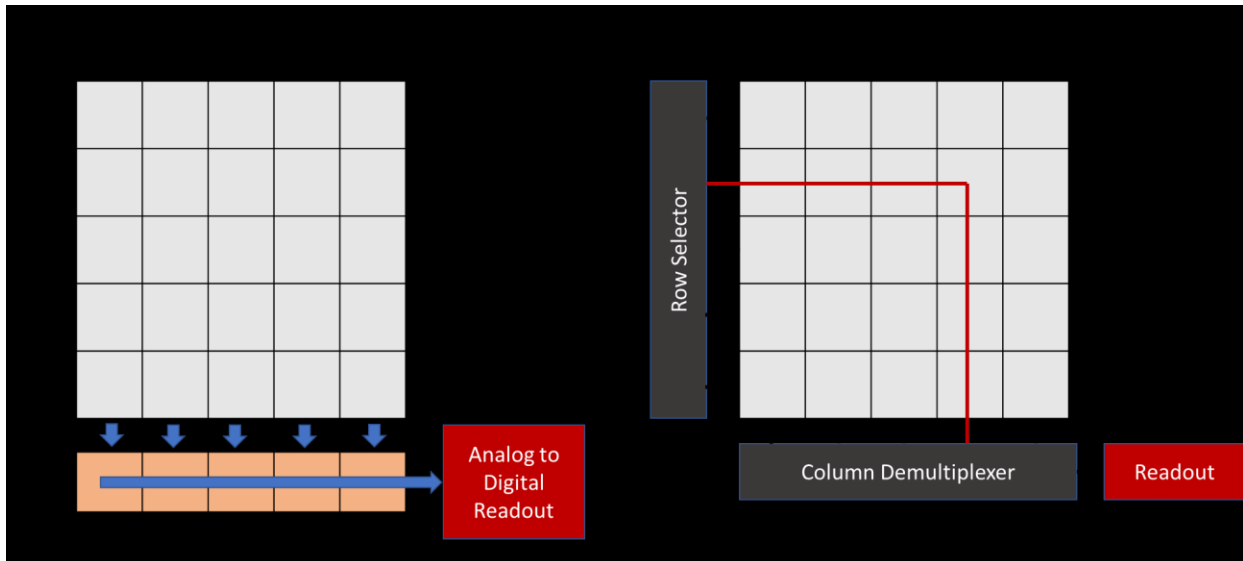
Figure 1: CCD and CMOS detectors. a) A CCD detector stores image data as charges on each detector element, then transfers the entire image downward one row at a time to a storage register, where it is then read out one column at a time. b) A CMOS detector has active electronics on each pixel, so it is able to address each pixel individually for readout.

With the advancement of integrated electronics, however, nearly all imaging today is done using either charge-coupled device (CCD) or complementary metal-oxide-semiconductor (CMOS) cameras (See Figure 1). CCDs are the more mature technology, and they consist of an array of photoactive regions, where charges are generated when light is incident. By applying a storage voltage, they are then able to accumulate a charge proportional to the intensity of light that is incident on that element. After an appropriate accumulation time, the charges can then be transferred row by row to a storage row, and then transferred one at a time to an analog to digital readout. CMOS detectors, on the other hand, have active electronics for each individual pixel, and so they can individually address each pixel element for readout. There are, of course, tradeoffs that can be made by reducing the total data being read by identifying smaller regions of interest or by binning multiple pixels together. However, the information must ultimately be recorded, and so the imaging rate for both types of cameras is ultimately constrained by the

electronic readout rate. Nevertheless, modern high-speed cameras can have electronic readout

rates in the GHz range, and can reach thousands of frames per second.
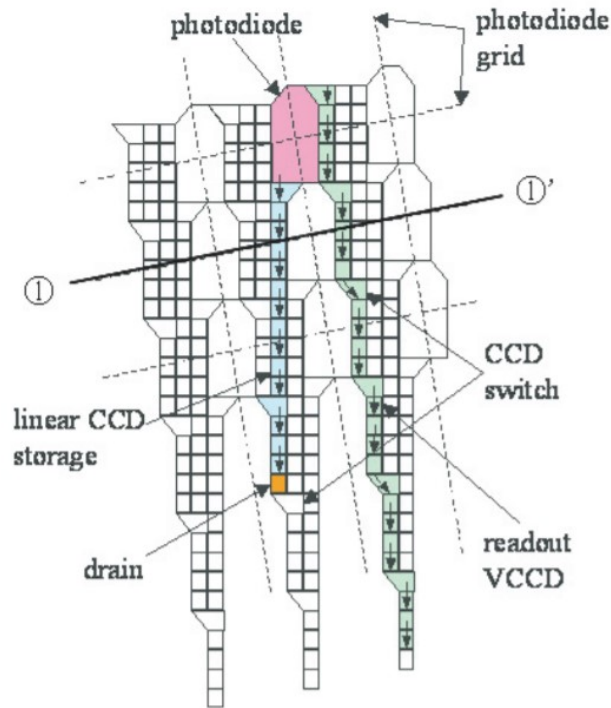
Figure 2: Chip diagram of the in-situ image sensor. The overview shows how charges are transferred from the photo-sensitive area to attached local CCD elements. Since the storage is local to each individual photodiode pixel, this can be done at extremely high speeds. [15]

One way to temporarily get around this is to build a camera that can store information

directly on the chip [15]. Since they can store elements from each pixel in parallel, they are now

constrained by readout rate of each individual charge storage unit, rather than the entire array as

a whole. With this trick, these cameras are limited to only the speed at which each CCD pixel

can transfer charges, which is typically 1 MHz. However, there are several tradeoffs to this

approach. As can be seen from Figure 2, the CCD storage areas of the chip must necessarily also

take up surface area on the device, which reduces the usable sensor area, resulting in a loss of

sensitivity. Furthermore, this also forces a tradeoff between sensor area and the number of CCD

storage units, meaning that a larger number of stored values will further reduce the available sensor area. On these cameras, a typical compromise is around 256 registers, and so the camera can only store 256 images before the images must be offloaded from the chip at a much slower rate. Therefore, while the camera can reach these very high speeds in short bursts, it cannot maintain this imaging speed for an arbitrary amount of time.
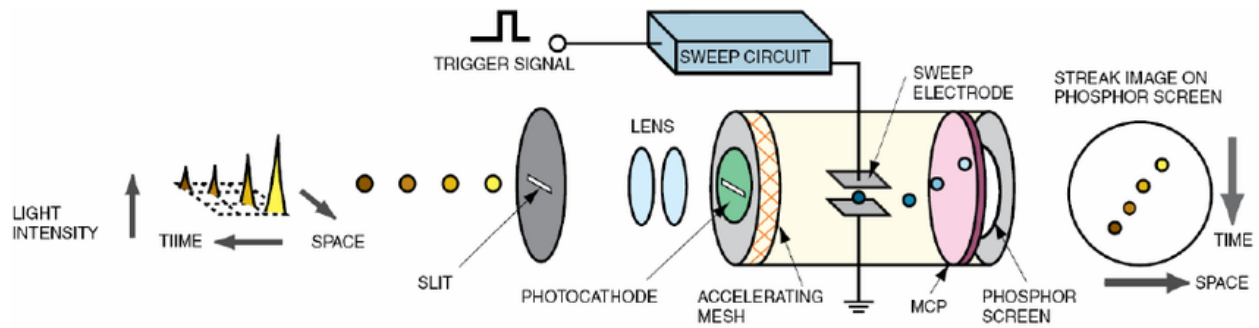
Figure 3: Streak camera. The light to be measured is sent through a slit, and focused onto a photocathode plate. The generated charges are accelerated and sent through an electrode deflector before hitting a phosphor screen at the end of the tube. The image on the phosphor screen then represents space in one dimension and time in the orthogonal direction. [16]

Another high-speed technology is the streak camera [17]. The way a streak camera works is that the light of interest hits a photocathode, where it generates charges that are accelerated down a vacuum tube. These charges are swept by a varying voltage before they hit a phosphor screen, where the image is then recorded by a conventional camera. In this way, the temporal dimension in spread out across a dimension in space. By doing this, streak cameras can reach truly ludicrous speeds, fast enough to even measure the travel of photons [18]–[20]. However, by sacrificing one dimension for time, this means that streak cameras can only image in one dimension. Furthermore, streak camera is inherently a single-shot process, confined to however much information can be projected onto the phosphor screen for collection by a conventional camera.

For many forms of scientific imaging, a form of pump-probe techniques can be used[21]–[24]. Pump-probe techniques rely on periodic phenomena that can be reliably replicated from period to period. By taking short snapshots at different parts of the period across many repeated waveforms, it is then possible to effectively build up a high-speed image sequence.

What all of these techniques have in common, however, is that they are either single-shot measurements, as in the streak camera and the in-situ image sensor, or that they require repetitive phenomena. Single shot cameras work very well for situations where the dynamics of the object of interest can be either predicted or reliably triggered, but cannot be reliable used for events that are either unpredictable or random. For these types of imaging tasks, the CCD/CMOS camera remains the most widely-used imaging method. Therefore, there remains a need for a faster, truly continuous imaging method.

1.2 Serial Time-encoded Amplified Imaging

One recently-developed method that was Serial Time-Encoded Amplified imaging (STEAM), demonstrated in 2009 [25]–[29]. The central idea behind STEAM is that since the ultimate imaging rate of a camera is related to the electrical readout rate, the electronic components of the system is simplified as much as possible: a single photodetector and an oscilloscope for measurement. For this type of system, the challenge is therefore to perform an all-optical serialization of the 2D imaging information, and to do this as quickly as possible. The solution to this problem is shown in Figure 4.
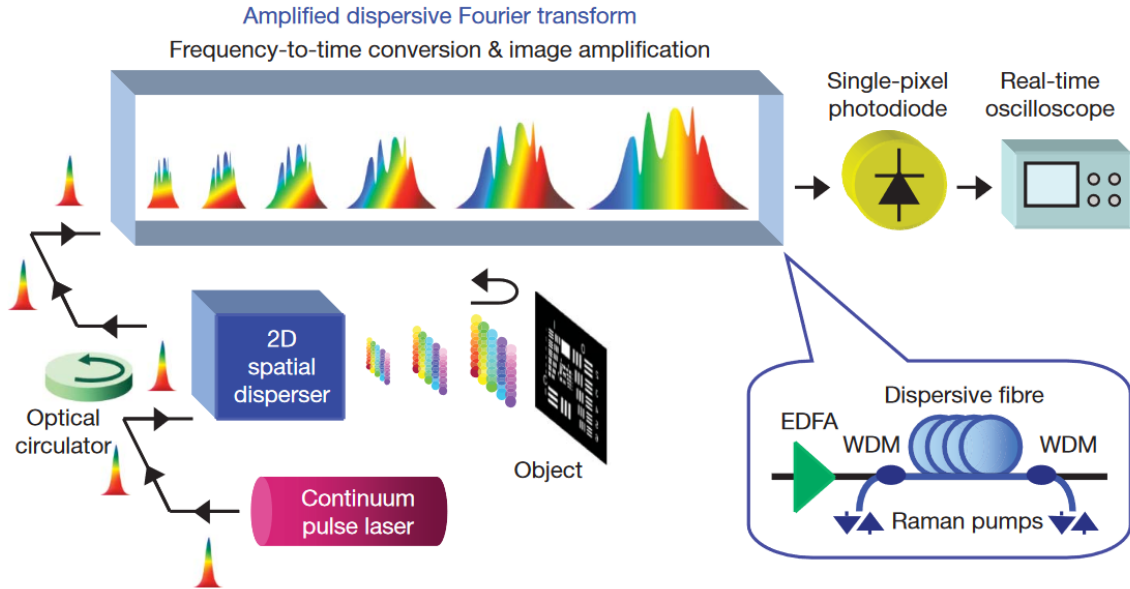
Figure 4: Experimental setup of Serial Time-encoded Amplified Imaging. A continuum pulse laser is sent to a 2D spatial disperser, which is a device that maps a wavelength band to each spatial location. This pulse is then reflected off an object, which is then recaptured by the imaging system and sent through a dispersive fiber. The dispersive fiber both disperses the wavelength components in time, as well as amplifying the signal using Raman pumping. The resulting optical waveform is measured by a high-speed photodiode and read out by an oscilloscope. [25]

The key component that allows this to take place is the amplified dispersive Fourier transform [27], which is illustrated in the insert of Figure 4. The core of the dispersive Fourier transformer is an optical fiber that is highly dispersive, or that different wavelengths of light travel through them at different speeds. This is typically considered a negative quality in fibers, and indeed the telecommunications industry dedicates an incredible amount of effort to reducing dispersion in communication fibers. In this case, however, the dispersion serves a very important purpose. If an incoming pulse of light contains a spectrum of frequencies, as it propagates along the fiber it will begin to spread out in space into its component wavelengths. By the time it exits the fiber, it has turned into a high-speed frequency sweep, with each moment in time representing the intensity of light at that wavelength band (see Figure 5). In short, the dispersive Fourier transform has taken the spectral data of the incoming pulse, and has serialized it in time.
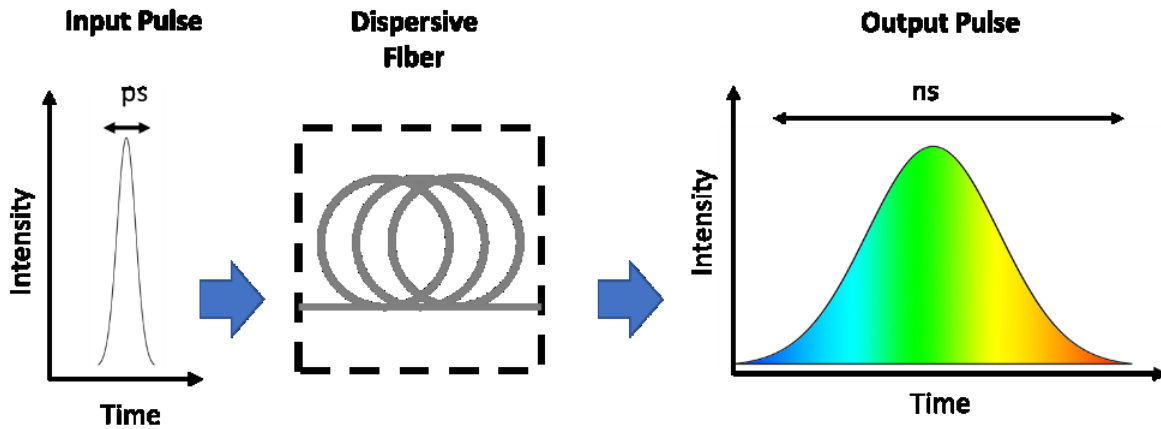
Figure 5: Diagram of the dispersive Fourier transform. The initial input into the fiber is a short broadband pulse. As each frequency component travels through the fiber at different speeds, when the pulse exits the fiber it is now a frequency sweep.

In order to convert this frequency sweep into an image, a 2D spatial disperser is needed to map each frequency band to a different pixel within the object area. This is done by arranging a virtually-imaged phase array and a diffraction grating at an orthogonal angle to each other, creating a so-called 'spectral shower'. This creates the 2D spectral map that is then focused onto the object plane by a microscope objective, and the resulting reflection is collected by the same microscope objective and sent through the dispersive fiber to the photodiode. Therefore, by simply reading the time-dependent signal collected by the photodiode, they are able to directly correlate the intensity at each moment in time with the intensity of the relevant pixel in the image.
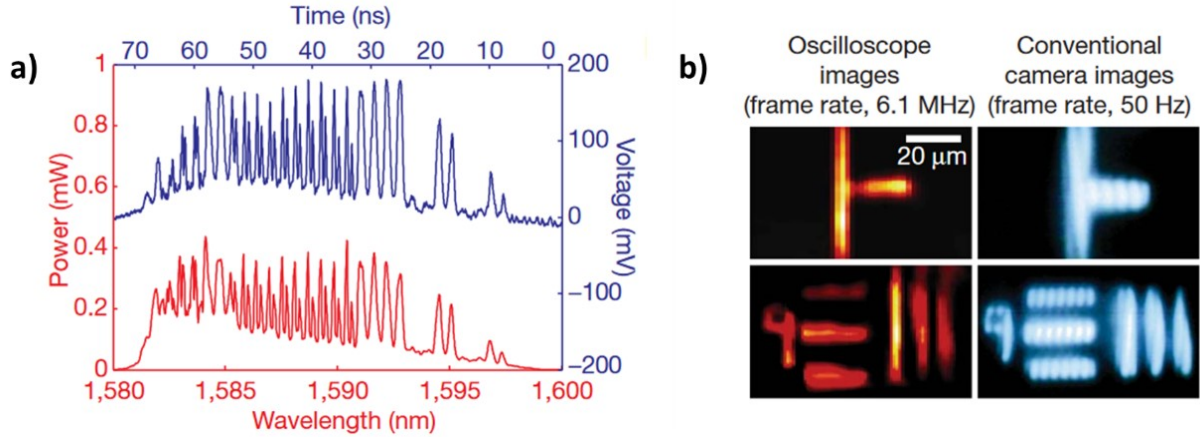
Figure 6: Experimental results for STEAM. a) The light intensity vs time measurement on the photodetector (blue) is a time-stretched copy of the spectrum, showing the success of the amplified dispersive Fourier transform. b) By mapping each point in time to a point in space, the object in the imaging plane can be recovered in a single pulse. The recovered image (orange) is compared with the CCD image on a conventional camera (blue).

From a systems perspective, this means that STEAM is able to take an individual laser pulse, and generate one image. The frame rate, therefore, is dependent on how much you need to stretch your pulse, and how fast your laser repetition rate is. For this experiment they used a photodetector with a bandwidth limit of 10 GHz, which is notably much faster than even the on-chip single-pixel CCD performance of ~1 MHz, with a total stretched pulse time of roughly 70 nanoseconds, taken at a frame rate of 6.1 MHz.

There are a few key takeaways from STEAM. The first is that ultimately, the continuous imaging speed of any system will be ultimately constrained by its maximum electronic bandwidth, so one method of maximizing the speed is to reduce all of the electrical components to a single high-speed photodiode. As a consequence of this, in order to maintain this speed, all of the information and array processing will need to be done optically, which can be done much faster than electronically or mechanically. So, how can we increase the speed of this even further?

1.3 Compressive sensing

1.3.1 Fundamentals of compressive sensing

The second key concept behind our work is called compressive sensing[30]–[34]. The concept behind compressive sensing can be summarized by the observation that most real-world signals are sparse in some basis. That is, there is a representative basis for the signal in which the number of degrees of freedom are notably smaller than the number of components in the signal. An equivalent statement would be that for most natural signals, there exists a basis in which many of its components are zero (or close to zero). Specifically for the case of images, this can be demonstrated by the fact that most images of interest can be heavily compressed (i.e. represented in a smaller number of elements) without significantly affecting the image quality.

If there is a way to represent an image in a vastly lower number of measurements, there must also exist a sensing method that can sample efficiently sample the signal of interest. For a serialized imaging method, this increased efficiency directly translates into an increase in speed. A 3:1 compression ratio, for example, would mean that we could increase the frame rate by a factor of 3x. Much more aggressive ratios are common in image compression, so how can we take advantage of this and implement a sensing method that takes advantage of this?

To illustrate this, let us consider a general mathematical form for the linear detection of a signal. If we have a discrete unknown image x_n with n pixels, sampled by a linear correlation to a series of functions A_m, where m denotes the number of sampling functions, to produce the

measurement values y_m. We can describe this sampling procedure as the following linear equation:

$$y_m = [A]_{m,n} x_n \qquad (1.1)$$

where y_m and x_n are both vectors of length m and n respectively, and A is a matrix of m rows and n columns. One potential sensing pattern is to take one measurement for each pixel, such as a conventional CCD camera might. For this type of sensing pattern, then each row in A must contain only a single element corresponding to a single pixel, correlating it with a single measurement in y, and A would be a square matrix with m=n. However, A and x can be in any linear basis, so sampling representations in other bases such as the discrete Fourier transform, the wavelet basis, or the discrete cosine transform can also be used to sample the image.

For situations where A is a nondegenerate matrix, then the reconstruction process is simple, as we can simply calculate the inverse of A and compute the following:

$$x_n = [A]^{-1}_{n,m} y_m \qquad (1.2)$$

However, we are interested in the situation what if we wanted to try to measure the object with fewer measurements than the object contains (m<n)? In this scenario, A is no longer a non-degenerate matrix, and the equation is now an ill-posed problem. This means that we have lost many degrees of freedom from our object to our measurement, and there are now potentially infinite number of solutions to the equation. At this point, it is not possible to exactly solve the equation, we must now make assumptions about the object, and apply some kind of minimization algorithm to search for a likely solution. Therefore, how can we recover the maximum amount of information about the object in a minimum number of measurements?

The answer for compressive sensing is to assume that the object in question can be efficiently represented in some basis. Let us assume that we can represent the object in a basis ψ, and that it is *sparse,* or that many of the components of base ψ are zero (or approximately near zero). The number of non-zero elements S in basis ψ is called the sparsity of the object. Obviously, if you simply were able to know which elements of ψ were non-zero, you could perfectly sample the object in only S measurements. But given that you do not know this information, what is the best way to acquire information about the object?

The answer to this question is related to the coherence of the basis between which the object is sparse (ψ), and the basis with which we are sampling the object (φ). The coherence of these two bases is:

$$\mu(\psi, \varphi) = \sqrt{n} \cdot \max_{1 \leq j,k \leq n} \left| \langle \psi_j, \varphi_k, \rangle \right| \tag{1.3}$$

The coherence of any two normalized bases is between 1 and $\sqrt{n}$. Basis pairs that have low coherence are ideal for compressive sensing, because the sparse information in ψ becomes widely distributed in φ, whereas for the extreme case that ψ= φ, the information would be minimally distributed. Thus, we get the result that if we know that the object is sparse in ψ, but we did not know which elements of ψ were non-zero, then ψ is in fact the worst basis to sample the object. There are many examples maximally incoherent pairs, such as the Fourier-Canonical basis, so for example if one knew the signal to be sparse in one domain, the other domain would make an ideal sensing basis.

Although it sometimes may be reasonable to know what basis your image may be sparse in (for example, in particle tracking you may know that across your field of view there are only a

few particles, so your image must be sparse in the real-space domain), it is not always possible to know this information, and so it is not realistic to be able to use a minimally coherent sensing pattern. However, there is a solution to this: random sensing matrices are overwhelmingly likely to be mostly incoherent with any particular basis. This is very important because this means that for any arbitrary object, a random sensing pattern is a more-or-less optimal basis in which to compressively sense an object. As any given vector of a random basis is likely to contain significant contributions from the object, the information will be efficiently distributed into the measurement. This leads to the rather surprising result that if a sensing pattern is very good, the received raw signal will look very similar to white noise.

1.3.2 Compressive sensing reconstruction

Given that we are solving an ill-posed problem, we can no longer hope to exactly calculate our original signal directly. As a result, we will need to implement an algorithm for the approximation of the signal. A comprehensive treatment of the optimization problem is beyond the scope of this thesis, but a large number of competing algorithms and different approaches have been developed to pursue this problem [32], [33], [35]–[37]. However, we can make a few generalizations about these compressive sensing algorithms.

First of all, what has become somewhat synonymous with compressive sensing algorithms are algorithms that seek to minimize the l1 norm:

$$\|x\|_{l1} := \sum_i |x_i| \tag{1.4}$$

The l1 minimization algorithms are valuable the l1 minimization constraint can be implemented as a linear program, allowing for a reasonably high-speed algorithm. Furthermore, using the l1 norm prioritizes sparse solutions. In the literature, we can say that the algorithm is likely to converge to a correct exact solution given the following condition[30]:

$$m \geq C \cdot \mu^2(\psi, \varphi) \cdot S \cdot \log n \tag{1.5}$$

where C is some positive constant. Although it is not possible to know exactly what C is when doing the measurement, the following conclusions will inform the design of a compressive sensing system:

1) The coherence of the bases is extremely important, and should be minimized. Given an unknown object, a random basis will be best.

2) If the coherence is low, then it should not matter which m elements are selected from the basis set. What matters is that the magnitude of m is high enough.

3) No prior information needs to be known about the object, except that it is sparse in some basis. For some signals this may be false. For example, if the signal looks like random noise, then it is not sparse in any basis, and cannot be sampled efficiently.

1.3.3 Single pixel cameras

For an experimental realization of compressive sensing, then, we need to take the incoming image we wish to acquire, apply many different linear sensing correlations to it, then measure the result of each one, knowing the basis vector behind each measurement. Experimentally, the most common method for realizing compressive imaging is known called

the single pixel camera[38]. The way that the single pixel camera achieves this is shown in

Figure 7.
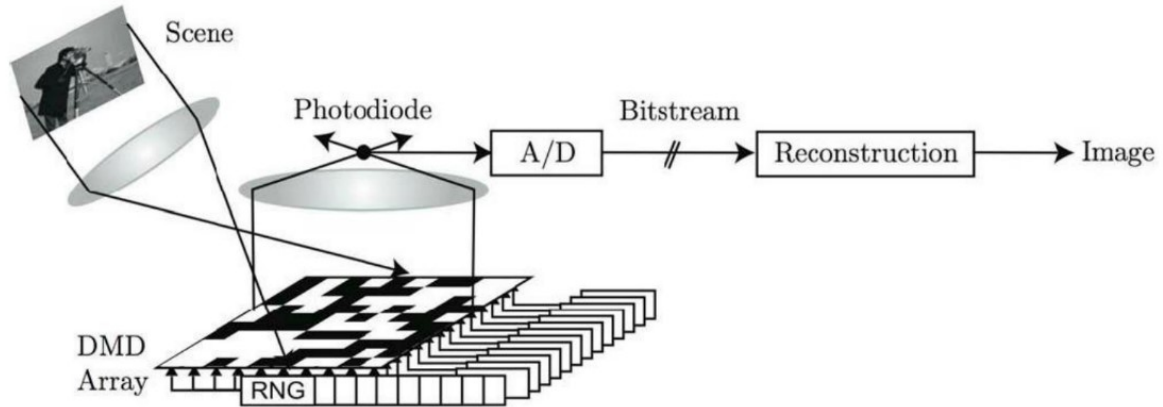
Figure 7: Overview of single-pixel camera. The scene to be imaged is focused onto a digital multimirror device, whose component mirrors can be individually addressed to turn the mirrors on and off. The DMD applies a series of patterns to the incident light, and the resulting light intensity is recorded a photodiode. This stream of intensity values is sent to a computer for reconstruction, and the image is recovered. [39]

In this single pixel camera, the image of the scene to be acquired is focused onto a digital

multimirror device, or DMD. The DMD is an array of small mirrors that can be individually

actuated into either an on or an off pattern. What this achieves is it allows a direct way to impose

a linear correlation of the pattern on the DMD array to the image of the object itself. The light

from the pixels that are selected to be on are then sent towards a collecting lens, which focuses

the light onto a single photodetector. Therefore, the signal received by this photodetector will be

the intensity sum of all of the 'on' pixels in the image of interest. This measurement process is

used to measure a single element of y_m. By cycling through a sequence of set patterns and

measuring the photodiode intensity after each one, we can build up the final y_m vector. Each

measurement pattern, then, corresponds to a single row of the A matrix. At the end of the

measurement, we will have the measured y_m and the known sensing matrix A. These

measurements are then sent to the reconstruction algorithm, and they can be reconstructed (See Figure 8).

(a) ideal image   (b) 205 wavelets   (c) 409 wavelets

(d) image on DMD   (e) 819 meas.   (f) 1600 meas.
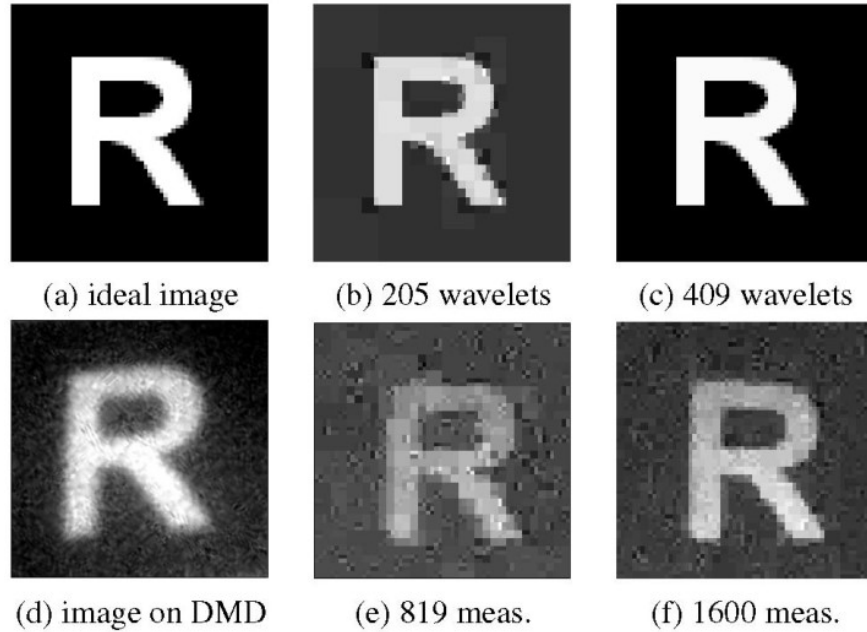
Figure 8: Experimental results of the single-pixel camera. a) The original image. b,c) The ideal image when only the largest 205 and 409 wavelet components, respectively, are kept. d) The image as it appears on a conventional camera. e.f) The compressive sensing reconstruction taken from 819 and 1600 measurements, respectively. [39]

The basic single pixel camera architecture, where an addressable spatial light modulator (SLM) is used to sample the object and the resulting light measured by a single pixel detector, has many advantages. First of all, only a single detector is required. One advantage is that this simplifies treatment of the imaging speed, as the system does not need to multiplex its sensing across multiple elements. The speed limit of the single-pixel camera is directly proportional to the speed of the detector. In more practical terms, the detector can be very inexpensive, as single-element detectors can be made very cheaply. Furthermore, this also potentially means that the camera may be available in wavelength bands where it is difficult to find cost-effective CCD or CMOS cameras, such as the mid-wave IR or terahertz frequency bands. Finally, since we can use

only a single large detector instead of an array of smaller detectors, the detector can also be significantly more sensitive than the sensor array, allowing for low-light detection.

1.3.4 Discussion of compressive sensing for high speed imaging

However, typical single-pixel cameras suffer from one major bottleneck: they require an active array of spatial modulators in order to perform their measurement. The DMDs used in the previous example can only hit speeds of up to 30 kHz, which is slower than many cameras. The reason is because the DMD is ultimately a mechanical technology, and switching each individual mirror from the ON position to the OFF position takes time to allow the mirror to settle. There are other spatial light modulators such as liquid-crystal SLMs, which use the controllable birefringence liquid crystals to apply their spatial modulation. These, however, are even slower, only capable of speeds of a few hundred Hz. In comparison, a typical photodiode may have an electronic bandwidth of tens of GHz- almost 5 orders of magnitude higher than these devices. So while compressed sensing may offer a large improvement in the imaging efficiency, it is more than outweighed by the vastly slower active-matrix arrays needed to actually perform the compressive sensing. While there are methods of compressive imaging that take shortcuts such as applying a streak camera to a time-shifted compressed sensing mask, a truly continuous compressed sensing camera seems out of reach so long as it requires active tunable arrays.

Chapter 2: Theory of Etalon Array Reconstructive Imaging

In review of the topics that have been covered, it is useful to state the important points: 1) Typical CCD/CMOS cameras are ultimately limited by their electronic readout rate. 2) STEAM is a method for optically transforming information from wavelength to time, allowing for very high speeds. 3) Compressive sensing single-pixel cameras can reduce the number of measurements needed- potentially increasing speed. 4) Single-pixel compressive sensing cameras ultimately rely on single photosensors, which can be very fast and highly sensitive. 5) In practice, single-pixel compressive sensing cameras usually use active-array light modulators that are actually many orders of magnitude slower than the photodetectors, presenting a massive bottleneck on the speed of the system.

The key here is that it may be impossible to perform a truly arbitrary high-speed spatial light modulation. However, due to the dispersive Fourier transform, it is possible to generate a very high-speed frequency sweep. The solution, then, is to create a modulator that is controlled by the frequency of light, rather than active electronics. Since there is no theoretical upper limit to how quickly we can generate a frequency sweep, and also no theoretical limit to how quickly a material can generate a transmission or reflection spectrum, this means that in principle, it is possible to create a high-speed passive spatial light modulator, as long as you have a frequency-sensitive element that you can use to control the transmission spectrum. We can imagine a situation, then, where we have an array of frequency-sensitive elements illuminated by a high-speed frequency sweep. At each individual frequency, some of the pixels would be highly

transmissive, and others would be very dark. For our ideal frequency-sensitive element, we would want the following properties:

1) It needs to have a very big contrast between where the transmission is high, and where the transmission is low. Since this structure needs to essentially act as a pixel element in an SLM, there needs to be a very big difference in brightness between when it is 'on' and when it is 'off'. The smaller the contrast is for each pixel, the higher the dynamic range requirements for our sensing, and the more critical the signal-to-noise ratio will be,

2) It must have relatively sharp spectral transmission changes. One way to think about the sensing pattern of the spectral modulator is that its transmission pattern is sampling the pixel in frequency space. The number of unique measurements it can make within that spectral bandwidth will be dependent on its ability to rapidly switch on and off.

3) It needs to be broadband. Different imaging applications may require using specific wavelength bands. For example, if we are targeting fluorescence imaging, we will need to the excitation bandwidth of the fluorophore, or if we are targeting a specific spectral signature, we will need to stay within that range. An ideal spectral transmission element would be able to be easily adapted to any required wavelength range.

4) The transmission needs to be easily tunable. Each 'pixel' in our array must have a unique transmission signature. Otherwise, it will be difficult for the reconstruction algorithm to distinguish between them.

Given these requirements, the structure that we chose to act as our frequency-dependent spectral pixel is the etalon, or Fabry-Perot cavity[40].

2.1 Principles of etalons

An etalon consists of two parallel semi-reflective surfaces. One of the most basic optical elements, it has been used for a huge variety of different tasks[41]–[43]. Etalons form the main optical resonance for laser cavities [44], [45], they are used to create dielectric mirrors for optical systems [46], they are used as multi-pass cavities for extremely sensitive gas and material sensing[47]–[49], and they have even been used to detect gravity waves[50], [51].
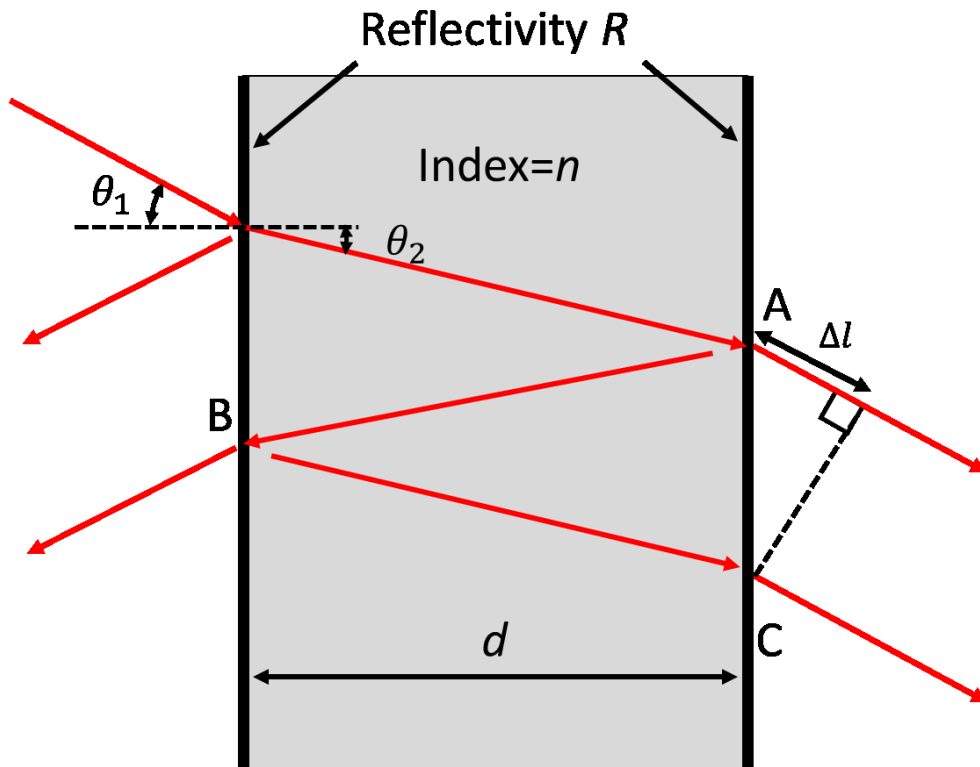
Figure 9: Diagram of an etalon. Light (shown in red) enters the etalon from the left, coming at an angle of θ_1 and internally refracting at an angle of θ_2. The index of refraction in the material is n, the reflectivity of the two surfaces is R, and the distance between them is d. Two outgoing paths are shown at A and C, with an outgoing path difference of Δl.

For the sake of simplicity, we will only consider etalons where both surfaces contain the same reflectivity R. Let us consider the case where light of wavelength λ is incident upon the cavity at an angle of θ_1. As the light hits the first reflecting surface, some of the light is reflected, while some light is transmitted into the etalon. Every time the light is transmitted, the amplitude is multiplied by $\sqrt{1-R}$, while every time it is reflected the amplitude changes by a factor of $\sqrt{R}$. The light that is transmitted into the etalon is refracted according to Snell's law. We will assume the initial amplitude of the light to be 1 and that the light is incident from air (n=1), the relationship between the two angles is $\sin\theta_1 = n\sin\theta_2$.

At point A, again some light is reflected and some is transmitted. The light that is transmitted from A now has a phasor of [52]

$$x_a = (1-R)e^{\frac{i2\pi dn}{\lambda\cos\theta_2}} \tag{2.1}$$

As the light reflects off of point B and arrives at point C, the light transmitted now has a phasor of

$$x_c = (R-R^2)e^{\frac{i6\pi dn}{\lambda\cos\theta_2}} \tag{2.2}$$

At the point where the two wavefronts match, the light from A will have travelled and additional distance

$$\Delta l = 2d\tan\theta_2\sin\theta_1 \tag{2.3}$$

The phasors can now be added:

$$x_a + x_c = (1-R)e^{\frac{i2\pi dn}{\lambda\cos\theta_2}+\frac{i2\pi\Delta l}{\lambda}} + (R-R^2)e^{\frac{i6\pi dn}{\lambda\cos\theta_2}} \tag{2.4}$$

The relative phase difference between the two components can be simplified to

$$\delta = \frac{4\pi dn}{\lambda}\cos\theta_2 \tag{2.5}$$

with an amplitude difference of R. Further reflections off of the surface will have the same amplitude and phase differences, so the jth iteration of reflection can be written as

$$x_j = (1-R)R^j e^{ij\delta} \tag{2.6}$$

The sum of all these components is then

$$x_{total} = \sum_{j=0}^{\infty}(1-R)R^j e^{ij\delta} = \frac{(1-R)}{1-Re^{i\delta}} \tag{2.7}$$

To get the total transmission of the etalon, we will take the square of the transmitted amplitude, which is equal to

$$T = \frac{(1-R)^2}{1+R^2-2R\cos\delta} \qquad \delta = \frac{4\pi dn}{\lambda}\cos\theta_2 \tag{2.8}$$

When plotted, this gives the following characteristic waveform.
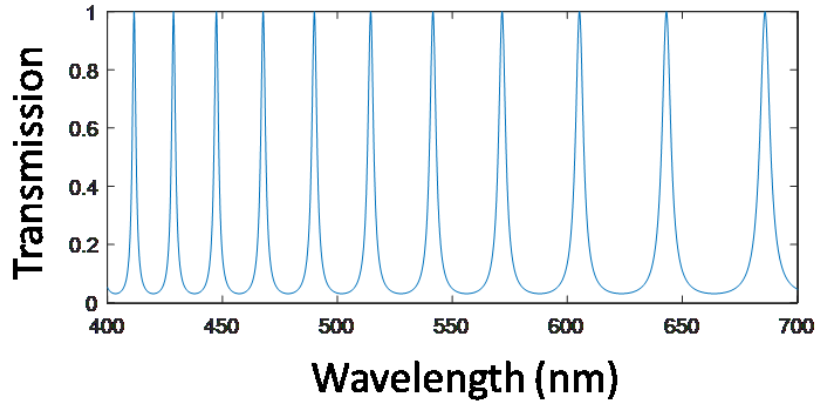
Figure 10: Example transmission of an etalon with n=1.5, d=3.5 um, θ=0, and R=.7

Already, we can see that the etalon possesses several properties that make it suitable for our spectral transformer- sharp peaks, high contrast, and a uniform behavior across a wide range of wavelengths.

For the sake of simplicity, let us consider the case where the incident light is normal to the etalon, or $\theta_1 = \theta_2$. In this case, it is easy to see that a transmission maximum occurs where $\frac{4\pi dn}{\lambda} = k$ where k is any integer. This is true whenever dn is equal to a multiple of the half-wavelength of light. The wavelength separation between peaks is called the free spectral range, and can be approximated as:

$$\Delta\lambda \approx \frac{\lambda^2}{2dn} \tag{2.9}$$

From this equation, we can see that for a given etalon, transmission peaks in the longer wavelength range will be separated by larger intervals.

The transmission peak will have an intensity of

$$T_{max} = \frac{(1-R)^2}{1-2R+R^2} \tag{2.10}$$

On the other hand, the transmission minima will be where $\frac{4\pi dn}{\lambda} = k + \frac{1}{2}$. The

transmission minimum will be

$$T_{min} = \frac{(1-R)^2}{1+R^2} \tag{2.11}$$

This means that our contrast between peak intensity and minimum intensity will be

$$\frac{T_{max}}{T_{min}} = \frac{1+R^2}{1-2R+R^2} \tag{2.12}$$
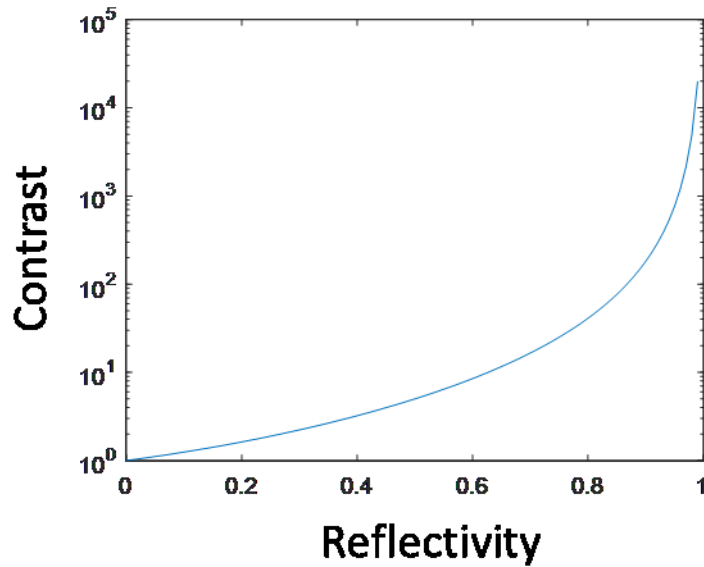
Figure 11: Contrast vs Reflectivity of an etalon

We can see here that the contrast is only a function of the reflectivity, and with moderate R of

around .7 it is possible to achieve contrast ratios above 10.

A related parameter is the *finesse* of the cavity, which is free spectral range (Δλ) divided by the full-width half maximum of a transmission peak δλ. The finesse of a relatively high-contrast etalon (R>.5) can be expressed as:

$$F = \frac{\Delta\lambda}{\delta\lambda} \approx \frac{\pi\sqrt{R}}{1-R} \tag{2.13}$$

As with the contrast, it can be seen that the finesse also is not a function of wavelength, which means that the relative sharpness of the peak of an etalon will be constant across all wavelengths.

To summarize, this means the etalon fulfils the requirements needed for our spectral pixel element. It can provide high-contrast, sharp transmission functions across a wide variety of bandwidths. It relies only on reflectivity an optical propagation, and does not require any special material properties. And finally, the transmission can be easily tuned just by altering the distance between the two reflective surfaces.
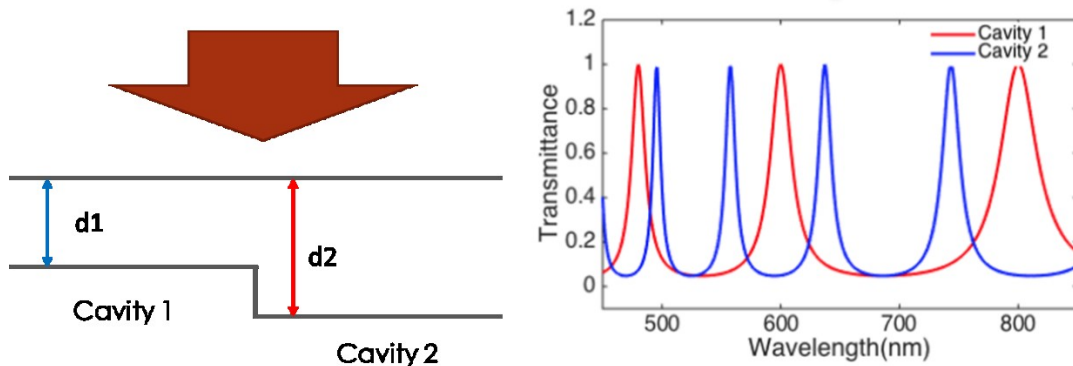
Figure 12: Illustration of the transmission spectrum of two etalons with different thicknesses

2.2 The etalon array
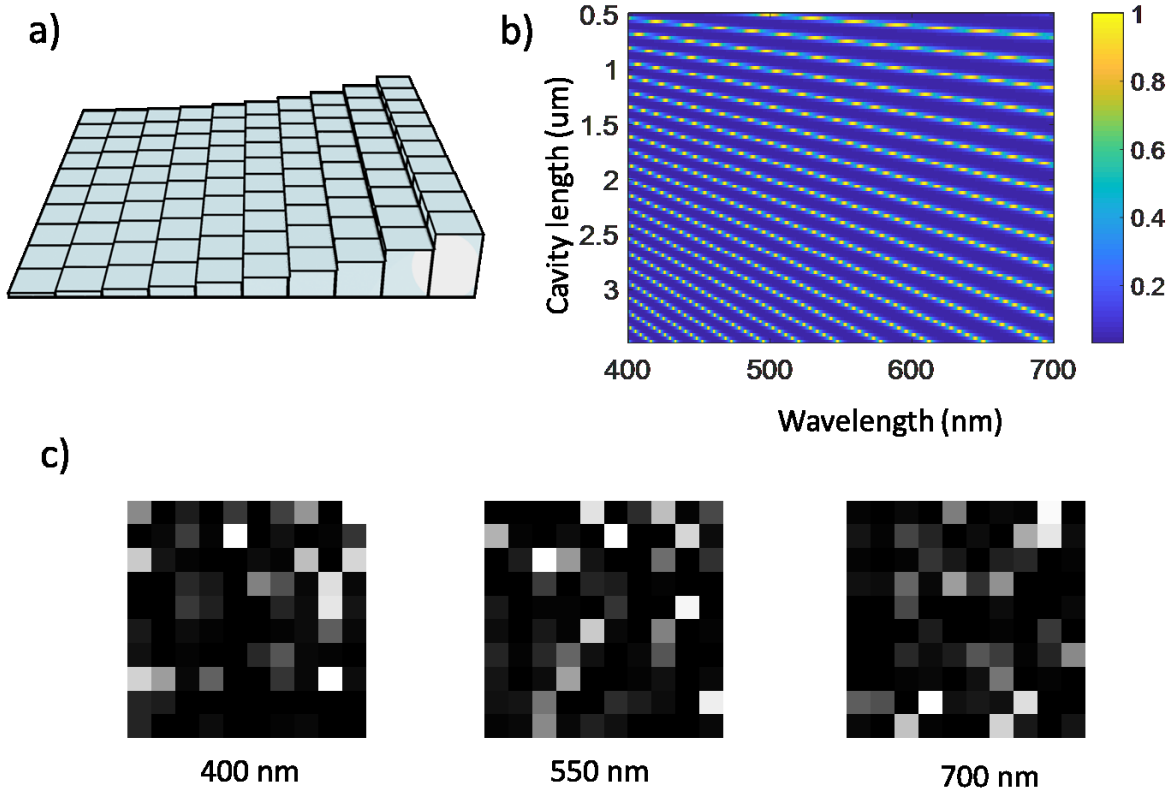
Figure 13: Diagram of the etalon array. a) An example 10 x 10 etalon array. b) Calculated spectral transmission for 100 different etalon thicknesses from .5 to 3.5 um. Each row is a different thickness. c) Simulated transmission images for an etalon rray at three selected wavelengths.

In order to use the etalon as a frequency-to-space encoding device, we will need to create an array of etalons (See Figure 13). In this way, each individual etalon acts as a spectral filter for the light that passes through it, and the etalon array as a whole serves as space-to-frequency encoding device. For this device, we will assume we have grid of etalons, each with a different length $d_i = d_1, d_2 \dots d_n$. To use this etalon array as an imaging system, we will use it in the following configuration:
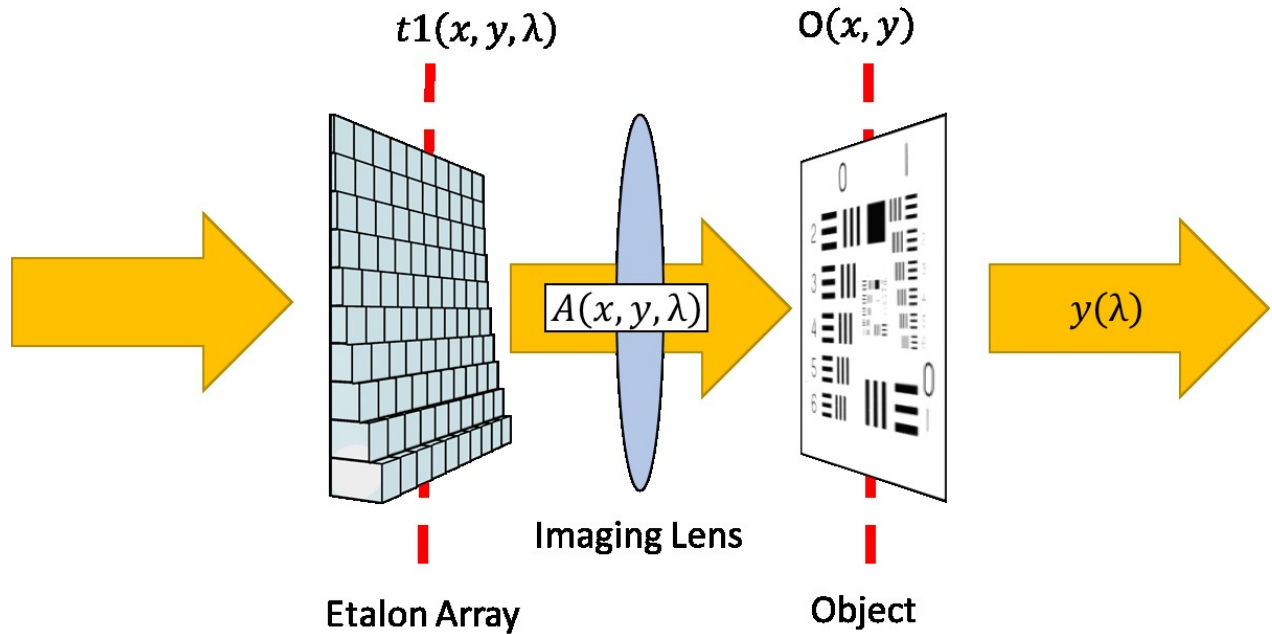
Figure 14: Overview of the etalon array sampling procedure. Incoming broadband light passes through the etalon array, which has a spatially dependent transmission spectrum (t1). The light coming from the etalon is now structured in x, y, and wavelength (A). The image of the etalon is then focused onto an object, which applies a spatial mask to the incoming light (O). The transmitted light is now encoded entirely in the frequency domain (y).

As Figure 15 shows, by illuminating the etalon with a broadband light source, and focusing the image of the etalon onto an unknown object, the resulting transmission will be entirely encoded into the spectrum of the transmitted light. The measurement process can be described here:

$$y(\lambda) = \sum_{x,y} A(x,y,\lambda) \cdot O(x,y) \qquad (2.14)$$

If we vectorize the x and y pixel positions to a single dimension i, and discretize the wavelength basis, we can re-write this into the standard matrix equation:

$$\begin{bmatrix} y_{\lambda_1} \\ y_{\lambda_2} \\ \vdots \\ y_{\lambda_m} \end{bmatrix} = \begin{bmatrix} A_{\lambda_1,1} & A_{\lambda_1,2} & \cdots & A_{\lambda_1,n} \\ A_{\lambda_2,1} & A_{\lambda_2,2} & \cdots & \vdots \\ \vdots & \vdots & \ddots & \vdots \\ A_{\lambda_m,1} & \cdots & \cdots & A_{\lambda_m,n} \end{bmatrix} \cdot \begin{bmatrix} O_1 \\ O_2 \\ \vdots \\ O_n \end{bmatrix} \quad i = 1 \ldots n, \lambda = \lambda_1 \ldots \lambda_m \tag{2.15}$$

From this perspective, we can see that for our sensing matrix, each column will represent one specific pixel of the 2D etalon array, and the transmission spectrum of each pixel at each wavelength is represented by the rows of the sensing matrix. Therefore, we have our framework for our frequency-to-space etalon compressive sensing system.

2.3 Simulated etalon array reconstructive imaging

We can now simulate the full imaging process of etalon array imaging by simply choosing appropriate parameters, simulating the measurement, and plugging the variables into the compressive sensing algorithm. For this simulation, we chose a 16 x 16 array of etalons with thicknesses ranging from 1000 to 4000 nm. We then simulated the spectral transmission of all of these etalons across a bandwidth from 400-700 nm at a resolution of 1 nm. We arranged the etalons to correspond with pixels in a 16 x 16 pixel image, and calculated the expected relative transmission through each pixel. Then, we chose a method for linearizing the 2D space into a 1D vector, so that the object becomes a vector of 256 instead of a 16 x 16 matrix, and the transmission matrix becomes a 300 x 256 matrix. The measurement is simply simulated by multiplying the sensing matrix and the object vector, resulting in 300 unit measurement vector. Then, we input the transmission matrix and measurement vector into the compressive sensing

algorithm[35], and it returns another 256-unit vector, which we un-scramble to become a 16 x 16 pixel image.
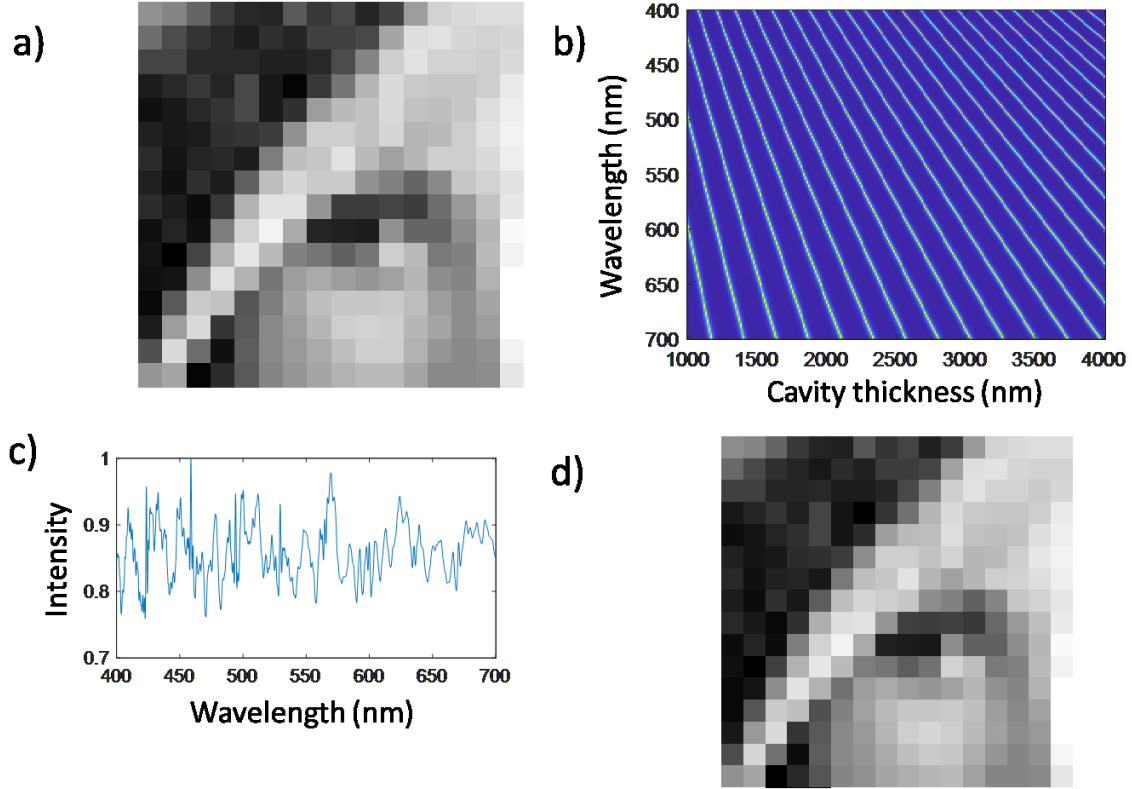
Figure 15: Simulation of an etalon-array imaging measurement. a) The original object. b) The calculated transmission spectra for an array of etalons with thicknesses from 1000 to 4000 microns. c) The resulting measured signal from correlating the etalon array with the image. d) The resulting signal

The result is shown in Figure 15, showing that we can use these approximate parameters to achieve an image.

2.4 Discussion of imaging speed limitations

Being a static device, the speed limit of our imaging process is no longer directly dependent on modulating the transmission mask. However, the etalon still does impose a

limitation to the ultimate imaging speed. It is perhaps best to view this from the perspective of a photon that enters the etalon resonator.

Once it is inside the etalon, for every time it reflects off the mirror it has a chance R to stay in the resonator and a chance (1-R) to exit the resonator. The fraction of photons that survive one round trip is R^2. The time it takes to make a round trip inside the cavity is $t_{round\ trip} = \frac{2dn}{c}$. The characteristic photon lifetime of a photon inside the cavity is therefore:

$$\tau_{photon} = \frac{\tau_{round\ trip}}{1 - surival\ fraction} = \frac{2dn}{c(1 - R^2)} \qquad (2.16)$$

Another way to view this is that for every photon that enters the etalon, there will be an uncertainty of τ_{photon} until it exits the etalon. Therefore, this uncertainty acts as a kind of low-pass filter for the etalon transmission, and is the fundamental limit to how quickly we can use the etalon array to do pattern generation. However, a back of the envelope calculation for R=.7, d=10 micrometers, and n=1.5 gives us a photon lifetime of approximately 2×10^{-13} seconds, corresponding to a frequency limit of about 5 terahertz (10^{12} Hz), which is far above the fastest available high-speed photodetectors, which have bandwidths measured in the GHz (10^9 Hz). Therefore, we can conclude that the etalon array will not be the bottleneck for our high-speed measurements.

2.5 Ultrafast swept-light source

However, the etalon array is merely an encoder from space to frequency. In order to do the ultrafast measurement, we must also do a transformation from frequency to time, which in this case means generating a high-speed frequency sweep. In order to generate our ultrafast

swept-light source, we will begin with the same general concept as in STEAM: Start with a short laser pulse, and time-stretch it into a chirped frequency sweep. However, we cannot do this in the exact same method. A back-of-the-envelope calculation shows that for visible fibers, typical dispersions are in the range of 800 ps/km*nm. Our photodetector has a bandwidth limit of 5 GHz, and so if we wanted to detect a signal with roughly 50 independent measurements, we would need to stretch out our signal to 10 ns. If we used a very large bandwidth of 200 nm, this means we would need around 6.25×10^4 km of fiber- not a practical number. Therefore, we need to find another method to generate the frequency sweep.

The method that we chose is called chromo-modal dispersion (CMD) [53], which uses a slightly different method for generating the frequency sweep. (See Figure 16) Instead of using the dispersive nature of a single-mode fiber to change the propagation speed of each wavelength, CMD instead uses a large-core multimode fiber, and couples in the different wavelengths at different angles. As a result, the geometric path length for each wavelength will vary, and the propagation time will be different for each wavelength.
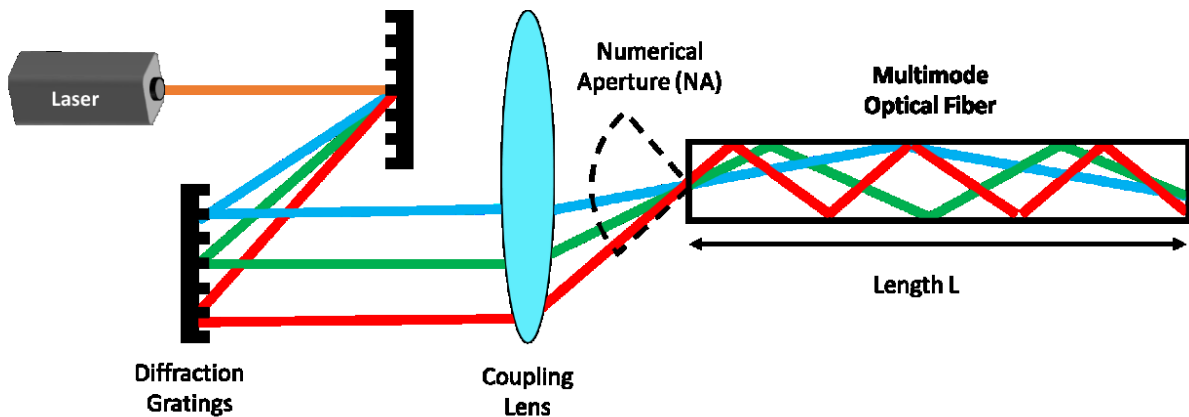
Figure 16: Overview of chromo-modal dispersion. A broadband light source is diffracted and collimated by a pair of diffraction gratings, which separates different wavelengths into parallel beams. Afterwards, a coupling lens focuses the different wavelengths into a multimode fiber. The

propagation speed down the fiber is now mainly a function of the geometrical path taken, rather than the local index of the fiber material.

The total amount of dispersion is now not limited by the dispersive properties of the fiber, but by path length differences taken by the different colors. Since the gratings can be fully tuned to select any arbitrary wavelength band, this means that this method is actually relatively insensitive to the exact wavelength band. Instead, the important parameters are, the numerical aperture (NA) of the fiber, as well as the length of the multimode fiber. Since CMD relies on using different modes for each wavelength, it is also important to choose a fiber core large enough to support the number of distinct wavelengths needed. For CMD, the fastest-travelling component will be the one normal to the direction of the fiber, and the slowest-travelling component will be the one travelling at the highest NA supported by the fiber. Another way to think about it is that one component will travel a much longer distance than the other. These path lengths are:

$$path_{min} = L, \qquad path_{max} = \frac{L}{\cos \theta} \tag{2.17}$$

where θ is the internal angle of the light at its maximum NA. We can find this through the relationship $NA = n \sin \theta$ or $\theta = \sin^{-1} \frac{NA}{n}$

Substituting that gives us

$$path_{max} = \frac{L}{\cos\left(\sin^{-1} \frac{NA}{n}\right)} = \frac{L}{\sqrt{1 - \frac{NA^2}{n^2}}} \tag{2.17}$$

The time delay will then be the difference between these two path lengths divided by the speed of light in the medium, or

$$\Delta t = \frac{n}{c}(path_{max} - path_{min}) = \frac{nL}{c}\left(\frac{1}{\sqrt{1 - \left(\frac{NA}{n}\right)^2}} - 1\right)$$

(2.18)

A back-of-the-envelope calculation with n=1.5, NA=.48, and L=100 m shows that this would result in an expected maximum time delay of around 28 ns- within the range of values that we are seeking.

2.6 Conclusion

In this section, we have explored theoretically the components needed to use etalons as the basis for an ultrafast spatial-light modulator for high-speed imaging. The etalon array possesses a unique combination of easy tunability, high contrast, sharp features, and easy adaptation across any range of wavelengths.

Chapter 2, in part, is a reprint of the material as it appears in Scientific Reports, 2016, 6, 25240. Eric Huang, Qian Ma, Zhaowei Liu, "Ultrafast Imaging using Spectral Resonance Modulation". The dissertation author was the first author of this paper.

Chapter 3: Experimental demonstration of etalon array imaging

3.1 Experimental Imaging Setup
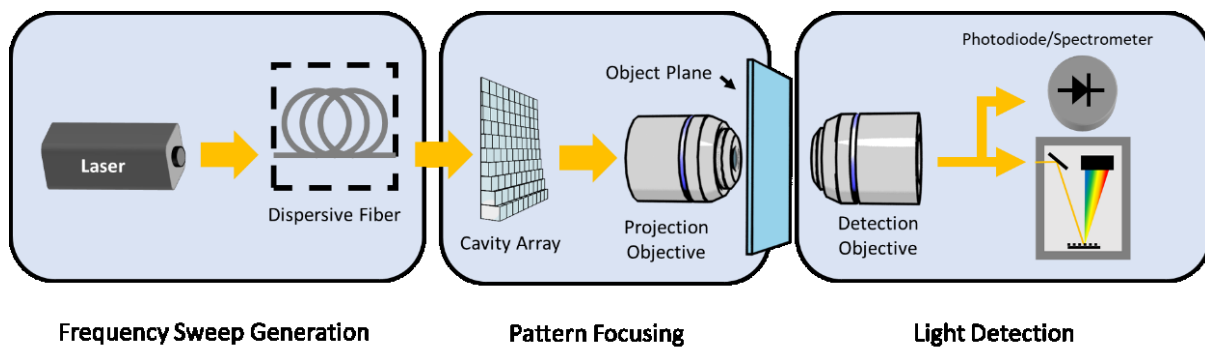
Figure 17: Schematic of an ultrafast etalon imager. The imaging system can be broadly divided into three parts: The frequency sweep generation, the optics for focusing of the etalon array into the object plane, and the light detection and measurement.

In order to produce a functioning imaging system, the experimental setup will need to integrate all of the following components: 1) Generating the high-speed frequency sweep, 2) Transmitting it through the etalon array to produce the ultrafast pattern generation, 3) Focusing the transmitted pattern onto the object of interest, and 4) collecting the resulting light using a high-speed photodetector and synchronizing the measurement with the laser to extract the relevant values, and 5) collecting these measurements with a computer to calculate the reconstruction. This is illustrated in Figure 17.

3.1.2 Ultrafast swept-light source.
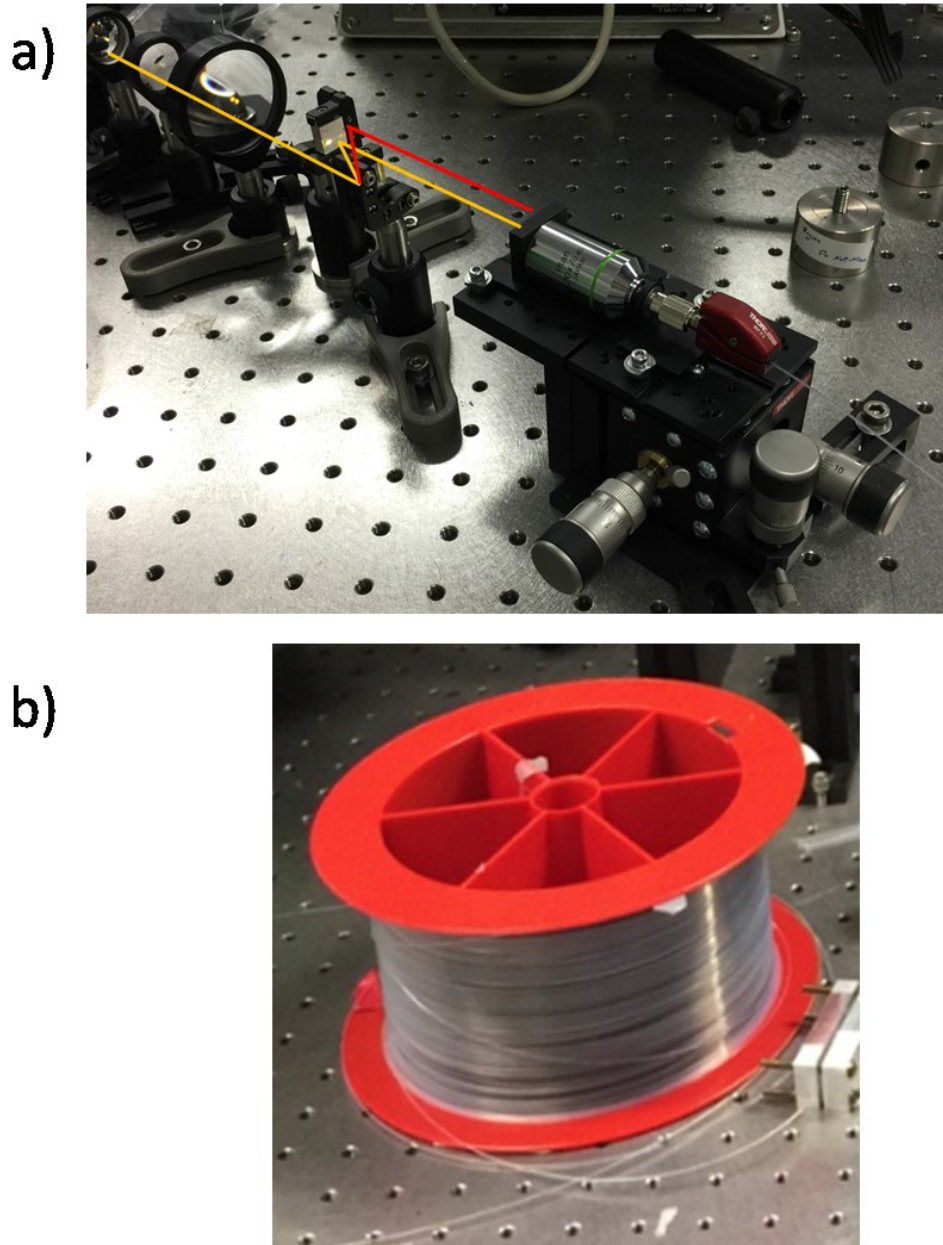
Figure 18: Ultrafast frequency sweeping setup. a) The apparatus for incoupling the laser to the chromo-modal dispersion fiber, showing the reflections off of two gratings, through the microscope objective, and into the fiber. Two parallel paths are shown for different wavelengths. b) The 100m .48 NA 400 um core fiber used to disperse the laser pulse. The mode scrambler can be seen in the lower right.

The setup used for our swept light source is illustrated in Figure 18. The first component of our light source is that we must have a short pulsed source containing the frequencies necessary to generate the transmission patterns through the etalons. The laser we used is an NKT photonics SuperK COMPACT supercontinuum laser that has an output from around 450nm to 2400 nm, a pulse output time of around 500 ps, and tunable repetition rate of up to 25 kHz. Furthermore, it is paired with an NKT VARIA tunable bandpass filter, that allows us to freely choose what range of wavelengths we will use for our measurement.

Afterwards, we need to disperse the different wavelengths and couple them into the fiber at different angles (See Chapter 2, Chromo-Modal Dispersion). The way we achieved this was by using a pair of diffraction gratings (Thorlabs, 300 grooves/mm separated by 10 cm) to separate the wavelengths in space and then re-collimate them, creating a linear spread of wavelengths. Afterwards, they are fed into a microscope objective lens (20x Olympus Plan Achromat, .39 NA), which focuses the beam onto the end of the fiber, with each wavelength being coupled in at a different angle.

The core component of the chromo-modal dispersion is the optical fiber used to generate the frequency sweep. In order to get as high of a dispersion between the highest and lowest angle as possible, it is desirable to select a fiber with a very high numerical aperture. In addition, the fiber core must be large enough to support the number of modes necessary. As a result, we have used a 400 um core fiber with a .48 NA output (Thorlabs BFL48-400). However, since this is not a single-mode fiber, there will also be intra-mode dispersion, due to defects in the fiber core as well as bending of the fiber itself. As a result, this means that over a sufficiently long fiber, the different modes will begin to mix, and no longer produce the dispersive action that is required. For our fiber, we found the best results after about 100m in length.

Finally, when the light reaches the end of the fiber, although they are dispersed in time, they still occupy different spatial modes. Since we would like each wavelength to be uniform in space, a final mode scrambler is clamped onto the fiber near its output to normalize the modes. The results of the chromo-modal dispersion, as well as results before and after scrambling, are shown in Figure 19 and Figure 20.
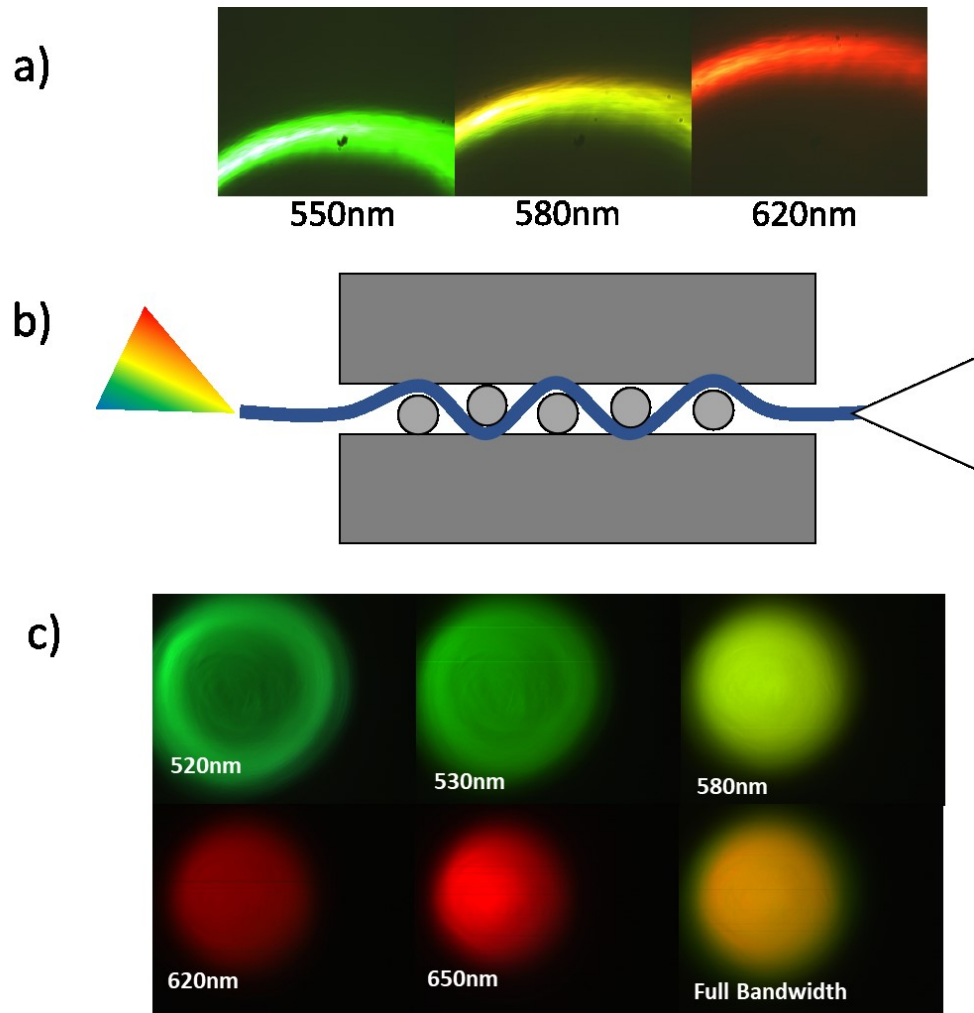
Figure 19: Spatial output profile of chromo-modal dispersion. a) Camera images showing the different numerical output angles when the tunable filter is set to different wavelengths. b) A diagram of the mode scrambler, showing the fiber core clamped between two jaws, forcing several tight turns. This mixes the different modes together. c) Camera images showing the uniform output profile at different wavelengths.
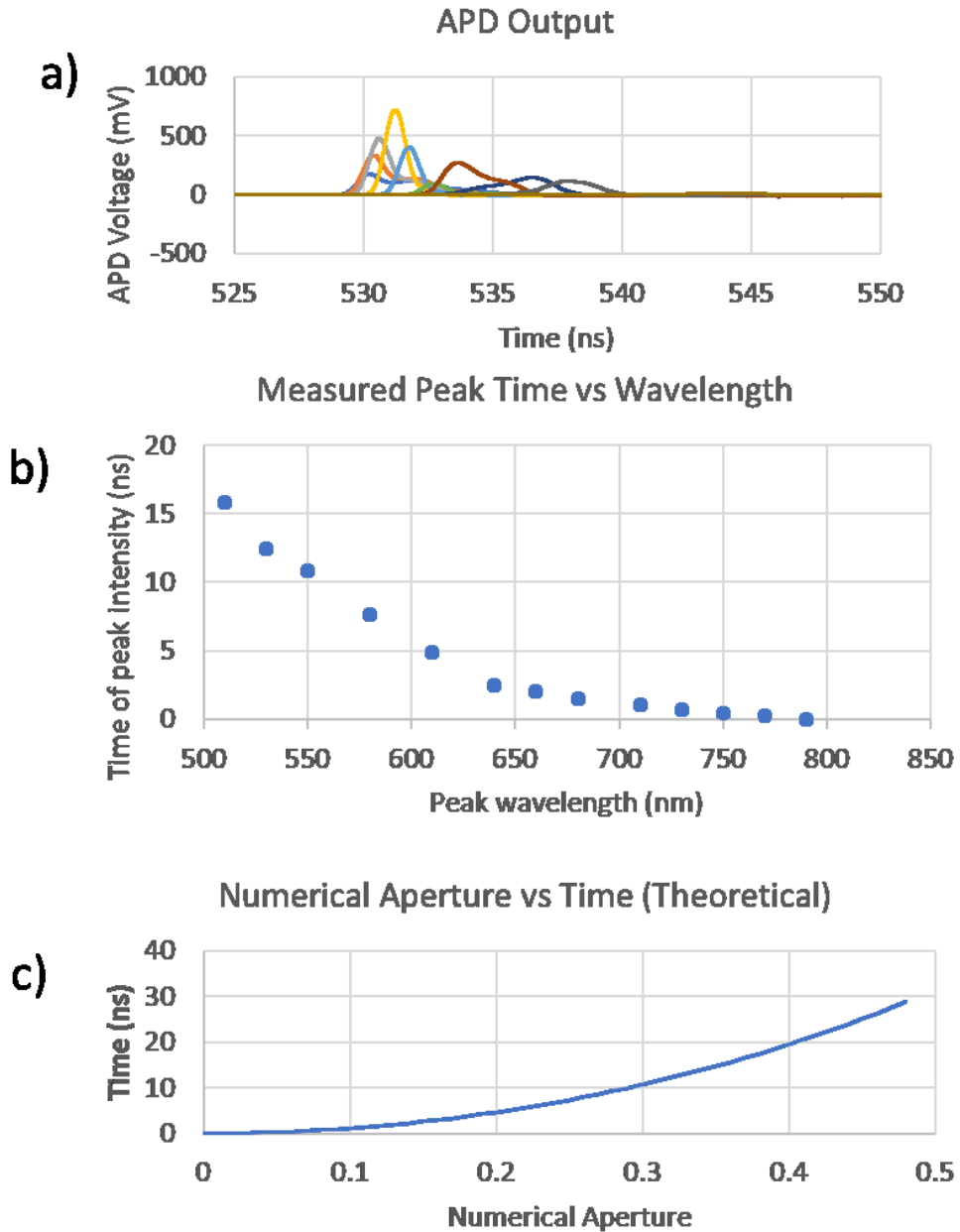
Figure 20: Experimental measurement of chromo-modal dispersion. a) Time vs voltage from APD with laser tuned to several different wavelength peaks. Time is measured from initial pulse from laser. b) Peak wavelength vs time of peak intensity, showing a dispersive shift of 15 ns from lowest to highest wavelength. c) Theoretical plot of delay time vs numerical aperture for 100m fiber.

3.2.2 Optical setup

Our imaging setup must be configured so that the object plane is conjugate to the image of the etalon array. We do this using a standard tube lens and infinity-corrected microscope objective, with the etalon array at the focal length of the tube lens (See Figure 21). Once the light has been focused on the object, it is then collected by a second objective, and then the light can be either focused onto an avalanche photodiode (APD) for temporal measurements (MenloSystems APD210), or sent to a second optical fiber connected to our spectrometer (Andor Shamrock 303i with an Idus 420 CCD). The signal from the APD, as well as the trigger signal from the laser, are sent to an oscilloscope for viewing and measurement.
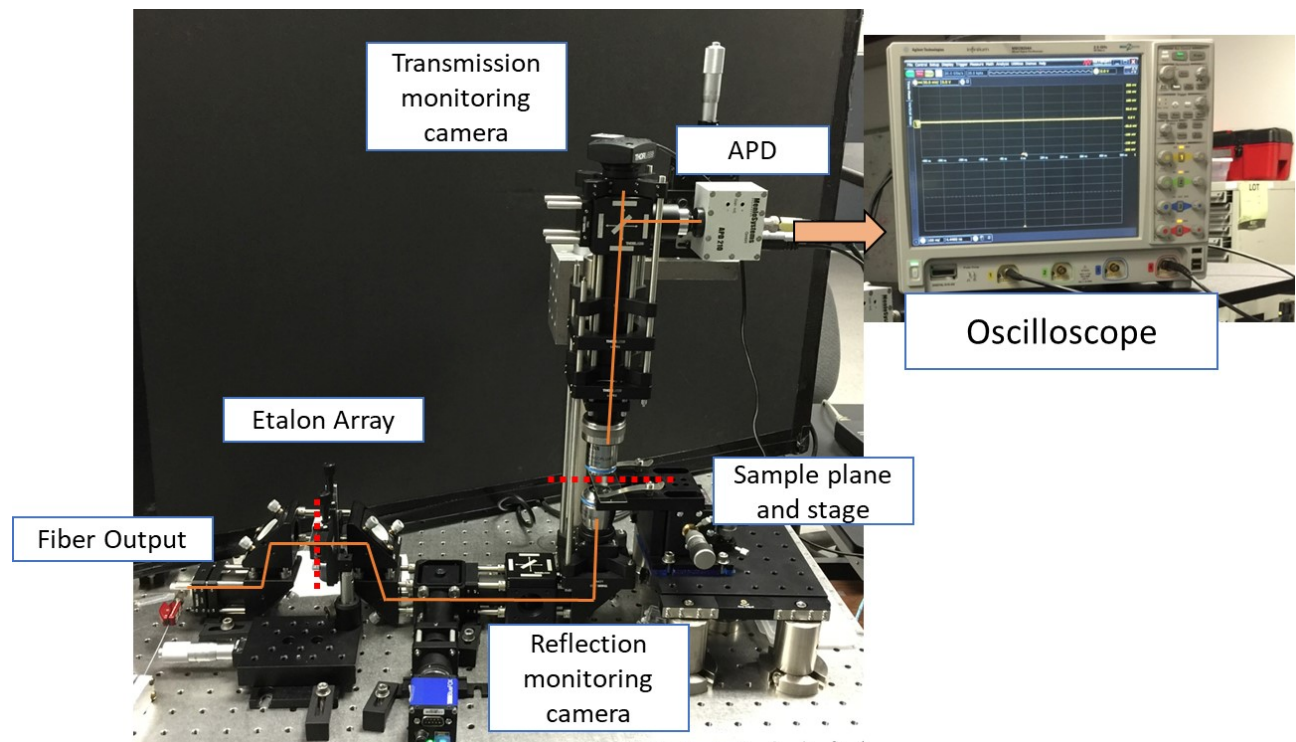
Figure 21: Overview of the optical system and microscope. The fiber from the chromo-modal disperser is sent from the left, and through the etalon array. The microscope objective then focuses the image of the etalon array into the sample plane, where an object can be placed. Finally, the

transmitted light is captured by another microscope objective and sent to the APD and oscilloscope for measurement.
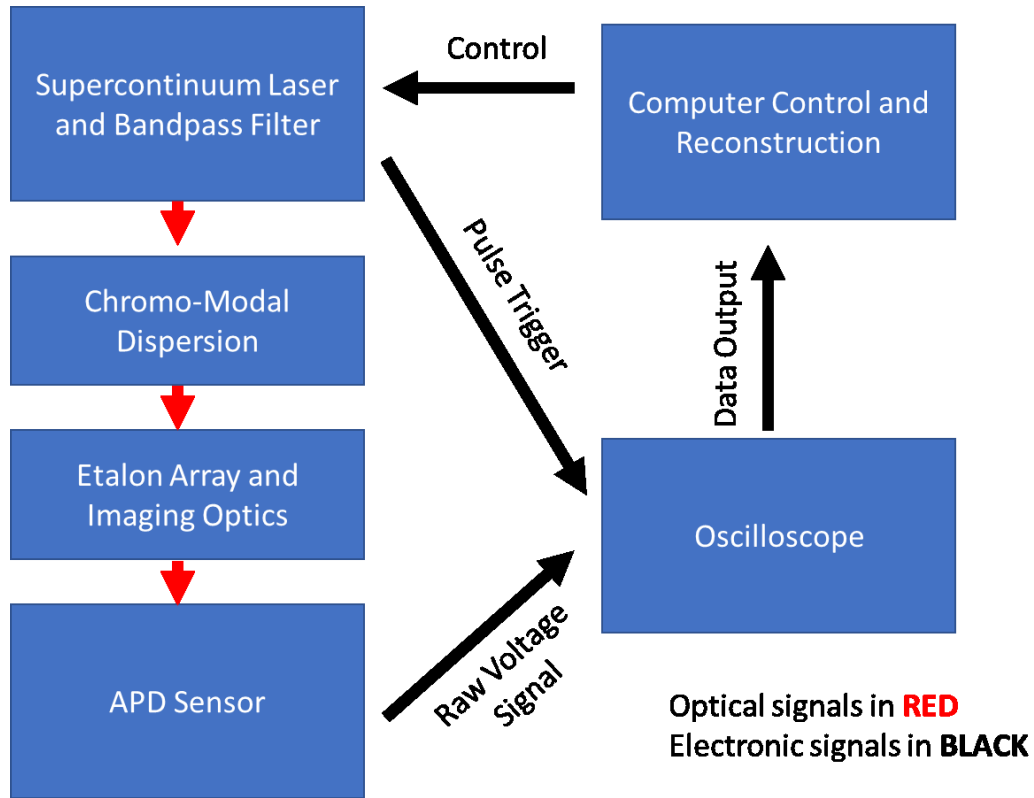
Figure 22: Hardware control diagram.

3.2 Etalon array design and fabrication

Although the key concepts behind the etalon array are quite simple, in practice they are bound by experimental limitations. To realize this structure, we will need to fabricate a 3D staircase pattern with extremely fine control over the depth of the cavities. Early attempts using 3D printing, electrostatic discharge machining with thermoplastic imprinting, and photochemical etching did not produce samples good enough for imaging. However, the ultimate process used to fabricate our etalon array was grayscale electron beam lithography.

3.2.1 Grayscale electron beam lithography

In conventional electron beam lithography, a resist is spatially written with an electron beam and developed, producing 2D patterns. For a typical positive resist such as poly-methyl methacrylate (PMMA), this works because the electron beam dose damages the polymers, allowing them to be selectively washed away with an appropriate developer (MIBK for a typical development).

However, for low electron beam voltage and a thick resist later, the dose per volume decreases as you go thicker into the resist. By carefully controlling the dose, it is therefore possible to etch 3D layers into the resist [54]–[59] (see Figure 23).

Figure 23: Overview of grayscale electron beam lithography. a) Two areas (shown in red) of a thick PMMA layer are exposed to different doses of the electron beam. After development, they have etched away to different thicknesses.

In order to develop the grayscale electron beam lithography procedure, we started with the thickest resist material I was able to use, which was Microchem 950 PMMA A9. By spin-coating at a low speed (100 rpm for 45 seconds), we produced a 2.8 micron thick resist later. Afterwards, we exposed different areas of the resist to different electron beam doses and found that the etch depth asymptotically approached about 2 microns with increasing electron beam

doses. This meant that using the current method, we can achieve a maximum variation of 2

microns from the shallowest etalon to the thickest etalon (See Figure 24)
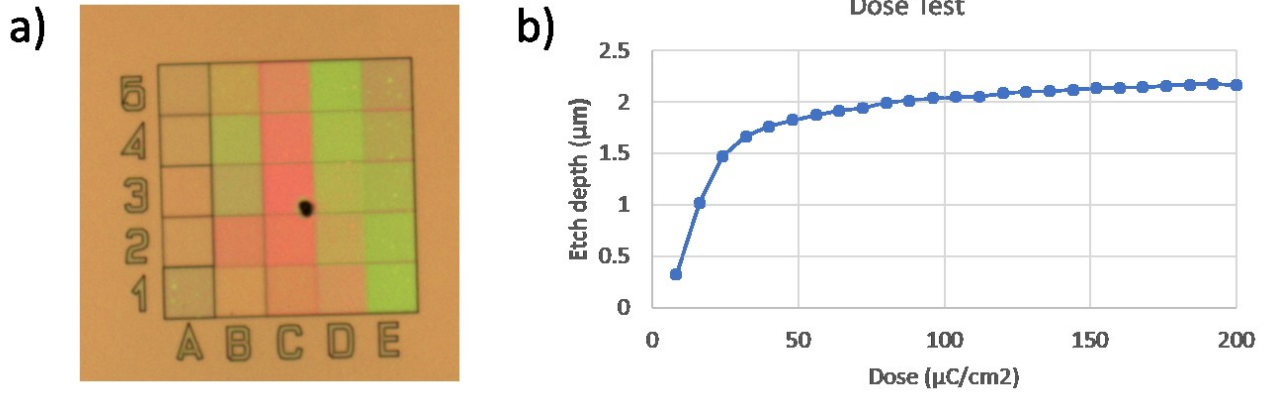
Figure 24: Dose test for a grayscale electron beam lithography with PMMA. a) Visual reflection image of a 5 x 5 area with different electron beam doses. b) Corresponding etch depth vs dose chart, showing an asymptotic etch limit of around 2.15 uC/cm^2

3.2.2 Etalon array fabrication procedure
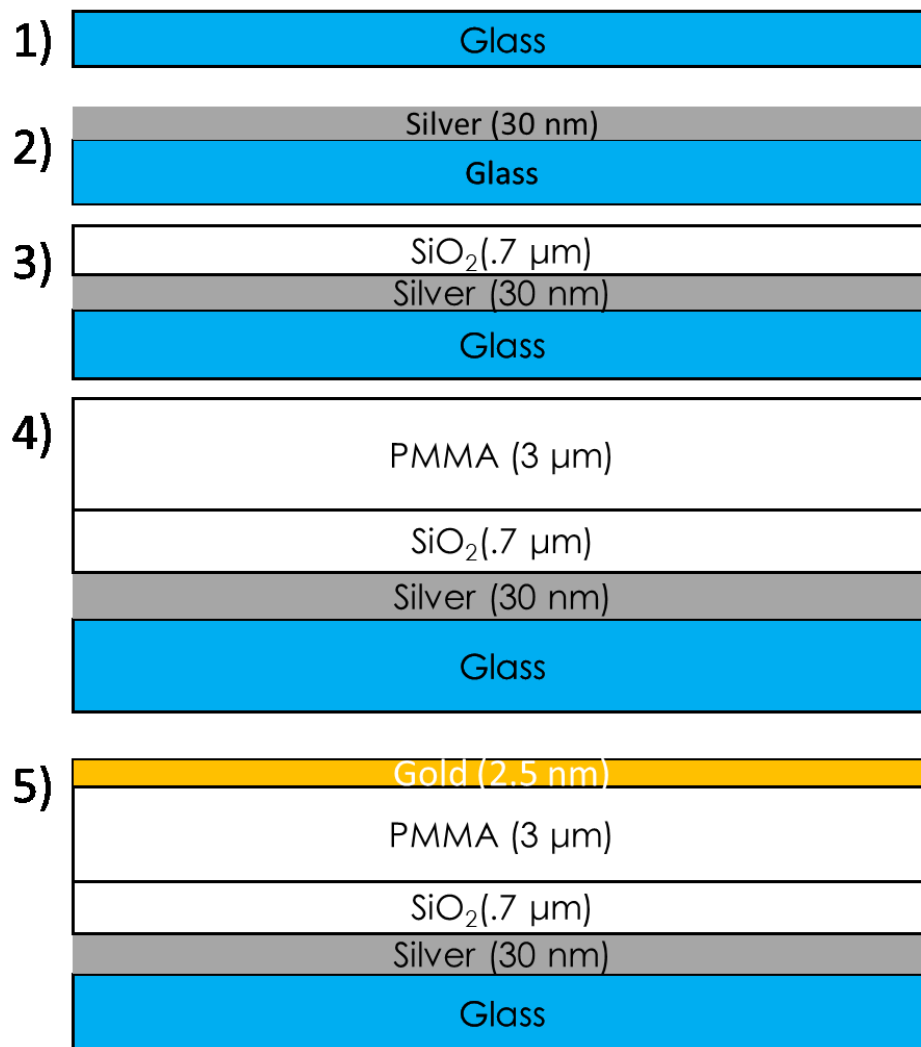
Figure 25: Etalon array fabrication part 1. 1) Glass substrate. 2) Initial silver film (and protective layer) are sputtered on. 3) Thick SiO2 layer deposted using PECVD. 4) PMMA spin coated. 5) Thin Au film sputtered on.
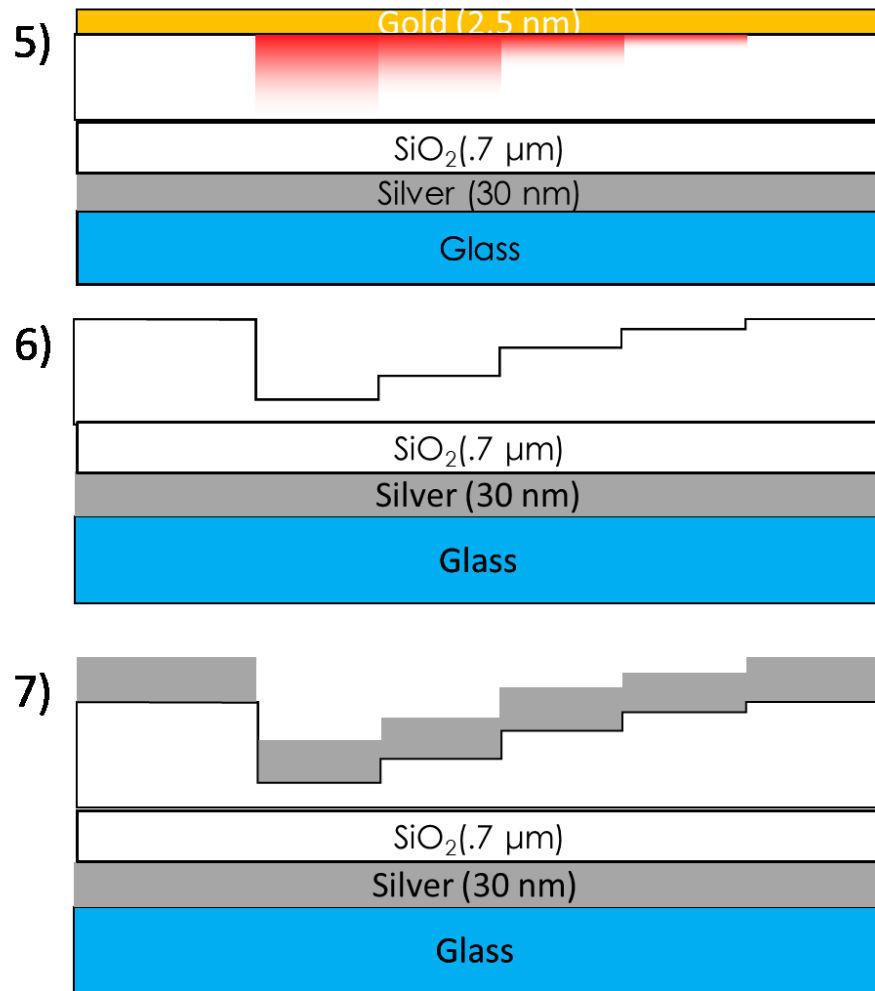
Figure 26: Etalon fabrication part 2. 5) Electron beam exposure. 6) Au etch and MIBK development of PMMA. 7) Final silver film deposition and protective layer.

Our fabrication procedure is shown in Figure 25 and Figure 26. Given the limitations of our fabrication, and based on simulated transmission patterns, we decided to aim for a total thickness range from roughly 1.5-3.5 microns in a 10 x 10 array, for a step size of roughly 20 nm. For our etalon, we chose an etalon dimension of 250 um x 250 um, for a total array size of 2.5mm by 2.5 mm. In order to preserve a reasonable transmissive efficiency, we aimed for a reflectivity of around .7, which translated into silver thickness of around 30 nm. Silver was chosen due to its broadband reflectivity and low loss. Our substrate was a glass microscope slide, which was cleaned and sputtered with 30 nm of silver, with an additional 30 nm protective SiO2

layer (Denton Discovery 18). The protective layer was necessary to prevent the silver from oxidizing during the following step. Since we desired a slightly thicker Afterwards, we used PECVD (Oxford Plasmalab PECVD) to deposit 700 nm of SiO2 onto the substrate. Finally, we spin-coated the PMMA onto the surface, and coated the top with a thin 2.5 nm layer of gold. Then we used the electron beam lithography machine (Raith GmbH Raith50) to do the exposure with doses varying from 1.4 uC/cm^2 to 80 uC/cm^2. After exposure, the substrate was briefly washed with potassium iodide to remove the gold layer, and then the array was developed for 5 minutes in methyl isobutyl ketone (MIBK) to remove the exposed PMMA, and followed by a 30 second rinse with isopropanol. Finally, after drying under N$_2$, we then used sputtering to add the final 30- nm silver layer along with a second protective 30 nm SiO2 layer. The finished etalon array, is shown in Figure 27.
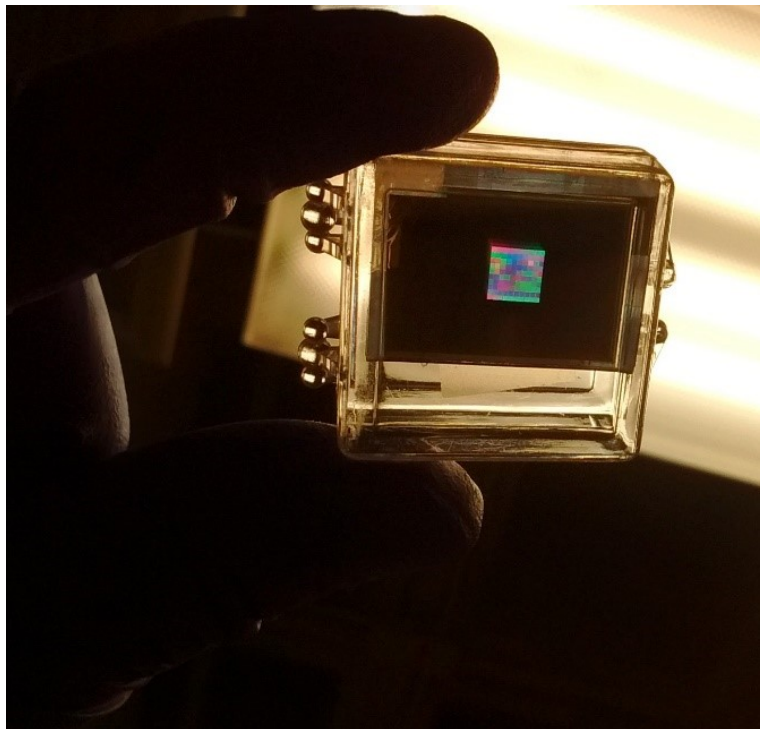
Figure 27: Camera image of final fabricated etalon array.

3.3 Experimental imaging

3.3.1 Calibration

In order to successfully reconstruct the image, we must first know our sensing matrix very well. To do this, we need to measure the temporal and spectral output of the laser through each individual etalon. We achieved this by putting an aperture in the object plane. By aligning the aperture with each etalon individually and measuring both the APD output and spectrum, we can build our sensing matrix for reconstruction. The sensing patterns for both the spectrometer and the APD are shown in Figure 28.
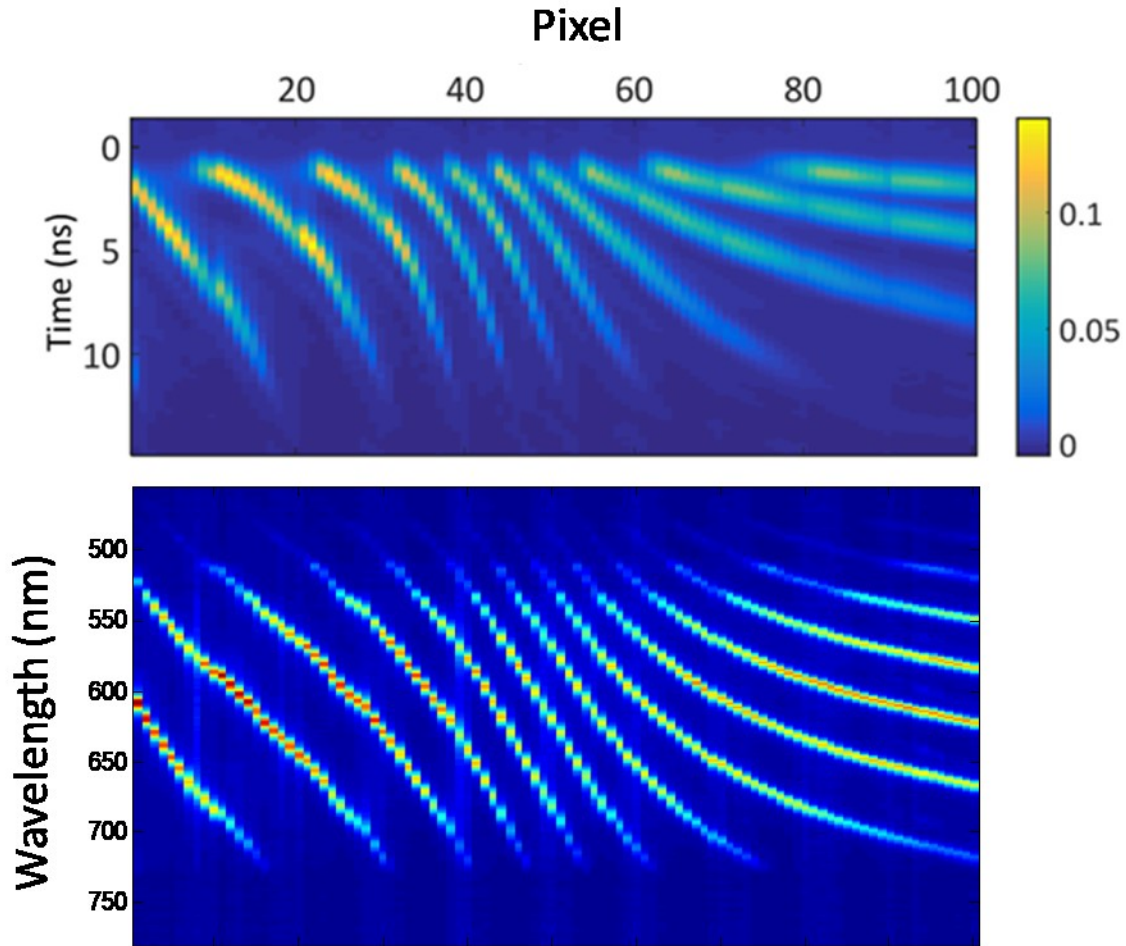
Figure 28: Calibration results and sensing matrix. Top: Detected APD waveform for each pixel. Bottom: Measured spectrum for eah pixel. These measured waveforms are directly used as the sensing matrix for the compressive sensing.

3.3.2 Spectral Imaging Results

In order to first test that our etalon array is capable of producing images, we fabricated a few chromium test images using photolithography. Our imaging procedure was to place these masks in the imaging plane and align them with image of the etalon array. Afterwards, we simply recorded the transmitted spectrum of light with the spectrometer. Since we already had

the sensing matrix from our previous calibration, we can then directly input the spectrum of the

light into the compressive sensing algorithm. The results are shown in Figure 29.
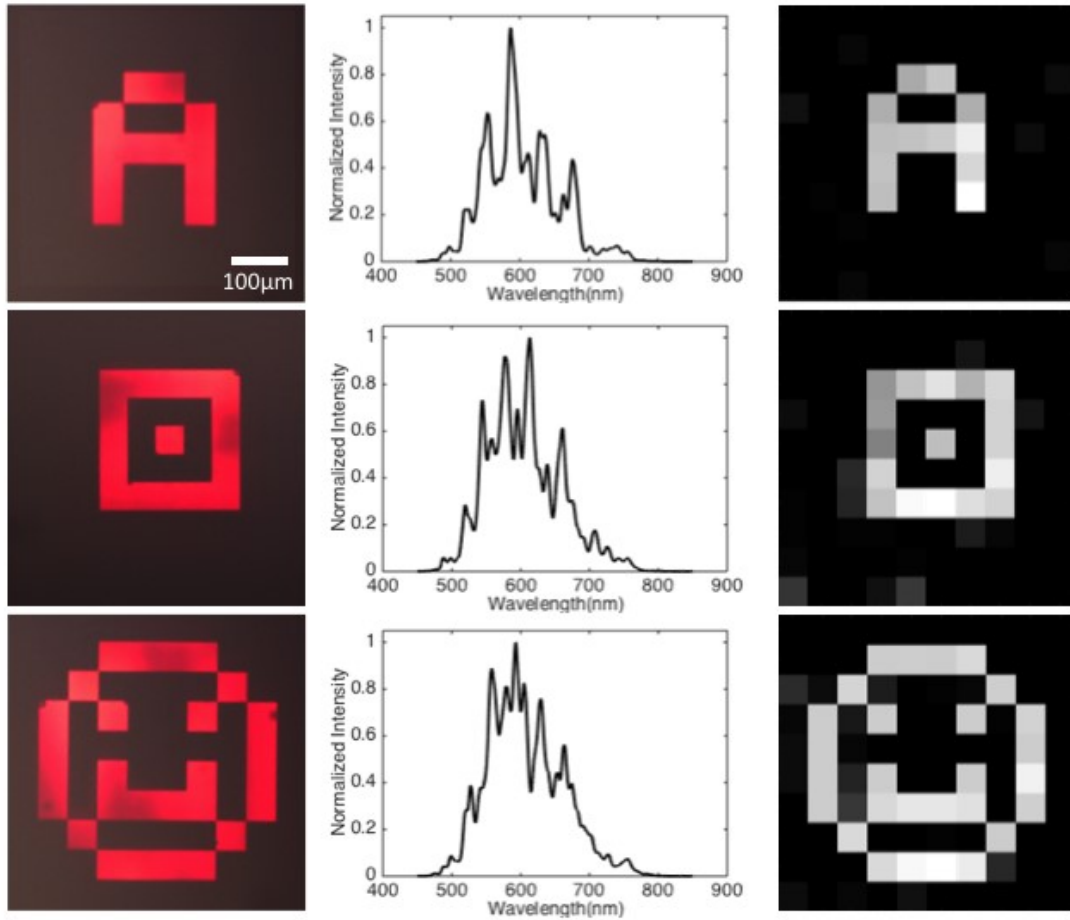
Figure 29: Compressed sensing results from spectral measurements. Left: CCD images of the masks used for the object. Middle: Detected spectra when the object was placed in the sample plane. Right: Recovered image from compressed sensing.

3.3.3 Temporal imaging results
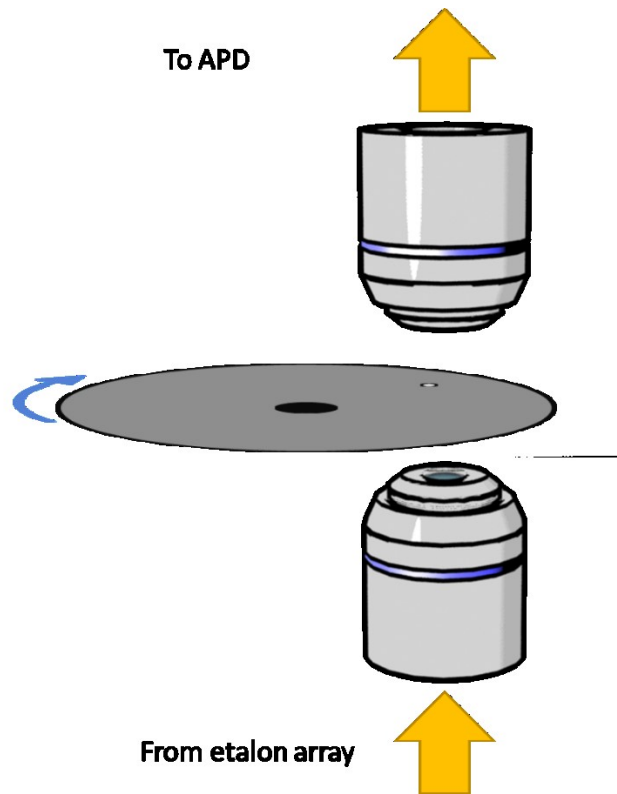
Figure 30: Imaging target for high-speed demonstration. A spinning disk with pinholes is placed in the object plane of the microscope.

      To demonstrate temporal imaging, we needed a high-speed imaging target. The target

that we chose was a mounted spinning disk with several pinholes cut into the disk (see Figure

30). Our frame rate was limited by the repetition rate of our laser, so we were able to

demonstrate this imaging at a 25 kHz. This means that our expected imaging result should show

a high-speed dot traversing the imaging area course of several frames. Afterwards, by using the

previously measured temporal responses as our sensing matrix, we can input the measured

voltages from the APD into our compressive sensing algorithm, and calculate the result. Figure 31 shows the experimentally obtained high-speed etalon array reconstructive imaging result.
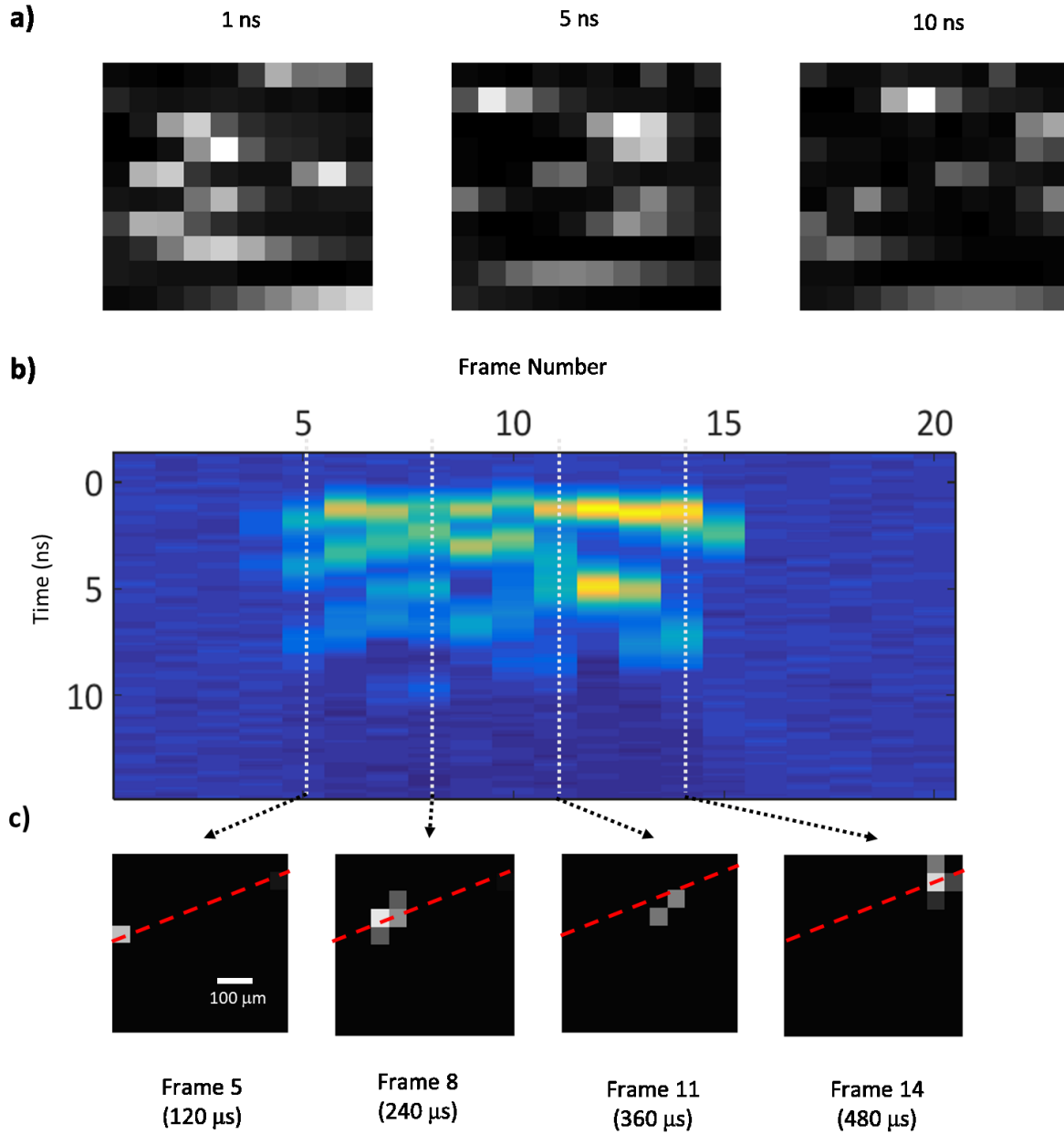
Figure 31: Compressed imaging results for time-based sensing. a) Based on the calibration, we know what the pattern of the etalon looks like at any given time. b) A sequence of APD measurements, with each column representing a single frame. c) The reconstructed image from certain frames, showing the dot traversing the imaging area.

Chapter 3, in part, is a reprint of the material as it appears in Scientific Reports, 2016, 6, 25240. Eric Huang, Qian Ma, Zhaowei Liu, "Ultrafast Imaging using Spectral Resonance Modulation". The dissertation author was the first author of this paper.

Chapter 4 – Ultrafast point localization

As demonstrated by our previous experiment, compressive sensing particularly excels in areas where the object is very sparse. For our next application of etalon array ultrafast imaging, we decided to apply this imaging technology to the area of high-speed microscopic particle tracking. To understand the motivations of this project, we will need to discuss some background.

4.1 Background

4.1.1 The diffraction limit

The development of optical microscopes has allowed us to see progressively smaller and smaller objects. However, there is a minimum size to which it is possible to resolve images optically. The reason behind this is that light is a wave, and so the diffraction of the wavefront sets this ultimate resolution limit.

There are several different metrics with which to characterize the diffraction limit, but it perhaps the most useful to consider the Rayleigh criterion [60], [61]. Since most optics are circular in profile, their physical size limitations means that we can consider them to be a circular aperture limitation in our optical system. By taking the Fraunhofer approximation [60], we can

the take the far-field intensity diffraction pattern to be the Fourier transform of the aperture.

Given a circular aperture of a radius r, the Fourier transform becomes

$$I(\theta) = I_o \left(\frac{2J_1(kr \sin \theta)}{kr \sin \theta} \right)^2 \qquad (4.1)$$

where I_0 is some arbitrary intensity constant, $J_1(x)$ is the first-order Bessel function of the first kind, and k is the wavenumber $k = \frac{2\pi}{\lambda}$ (see Figure 32). This pattern is known as an Airy disk, and can be easily seen in situations such as in the focused waist of a laser beam or, more relevantly, when looking at images of very small objects.
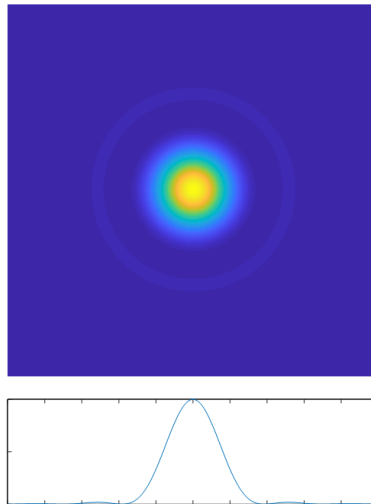
Figure 32: The Airy disk. For a diffraction-limited system with a circular aperture, the point spread function will be an Airy disk, with the characteristic dim ring surrounding the bright center.

The defining characteristic of the Airy disk is the bright center, surrounded by the alternating light and dark rings. For any well-behaved diffraction-limited imaging system, these Airy functions can be considered to be the fundamental building block of the image. If we consider the case of imaging two point-like objects, we will see two Airy disks. As they get closer together, the rings will begin to merge. The Rayleigh resolution criterion states that the

resolution of such an optical system is the point at which the center of one Airy disk occupies the distance to the first dark disk of the other Airy disk. From our Bessel function, we can say that the first dark ring (or intensity minimum) occurs where

$$\sin \theta = 1.22 \frac{\lambda}{r} \qquad (4.2$$

If the aperture in question is a lens, as in a microscope objective, we can relate this angle to the focal distance of the lens, and the Rayleigh criterion in space instead of angle now becomes

$$D = \frac{.61\lambda}{NA} \qquad (4.3)$$

Effectively what this means is that the resolution every microscope system is limited by the wavelength of the light and the numerical aperture of the imaging objective.

For many purposes, especially for biological applications, the wavelength of light is typically limited to the visible range, as shorter and more energetic wavelengths become damaging to the sample. For the case of numerical aperture, as the sin of the achievable angle can never go above 1, this means that the numerical aperture has a limit of the index of refraction of the surrounding medium. Since microscope samples are typically mounted on glass, this means that specialty index-matching oils along with oil immersion objectives can be used to reach a numerical aperture of 1.5. Some specialty objectives have managed to reach NAs of up to 1.7 by using special high-index immersion oils, cover slides, and objectives, but it is probably infeasible to achieve any significant improvement in this area. A back of the envelope calculation shows that for a wavelength of 500 nm and an NA of 1.5 will result in a Rayleigh resolution of around 200 nm. For conventional imaging, this represents a hard limit on the resolution of an image.

4.1.2 Point Localization Imaging

One shortcut around the diffraction limit, however, is single-particle localization microscopy[62]–[65]. If you have just a single isolated particle in your image, it will appear as an Airy disk. However, if you know that you are a) looking at a single particle and b) your particle is much smaller than the diffraction limit, this means that you have access to an even greater level of information. Although the Airy pattern itself may be 200 nm or more in diameter, you know that the molecule must be at the centroid of the Airy disk, and so you can know the position of the molecule to a much smaller radius of uncertainty. In practice, this is done by fitting the Airy function to a Gaussian curve, and finding the center (See Figure 33).
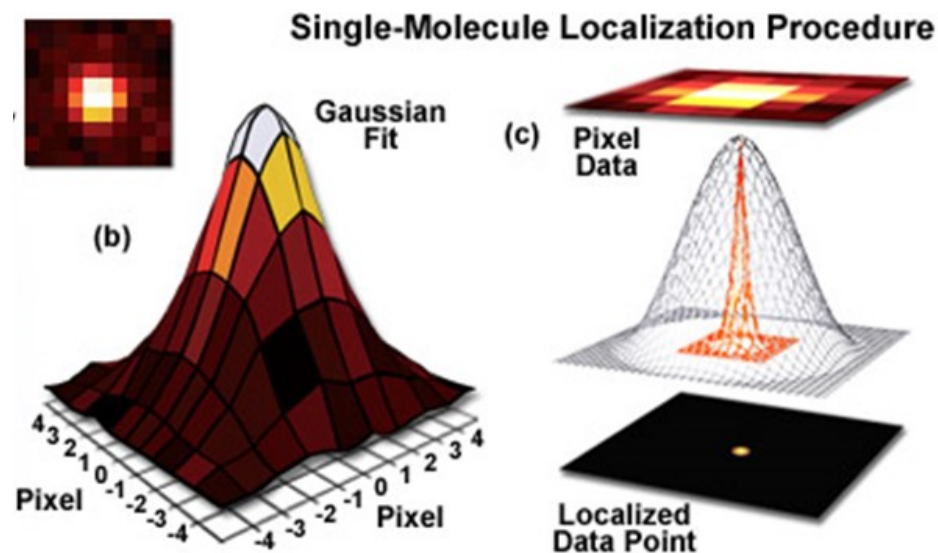
Figure 33: Single-Molecule Localization. On a camera image, an isolated molecule appears as a roughly Gaussian function. By this fitting, it is then possible to identify the center of the function to a much smaller scale than the Gaussian itself. [66]

Assume that a point-like particle is captured on camera and fit with a Gaussian curve. The image of the particle is taken using a camera with a pixel size *a*, and the image is fit to a

Gaussian function with a standard deviation of s. The uncertainty of the position of the particle will be equivalent to the standard error of the mean σ:

$$\sigma = \sqrt{\frac{s^2}{N} + \frac{\left(\frac{a^2}{12}\right)}{N} + \frac{4\sqrt{\pi}s^3 b^2}{aN^2}} \tag{4.4}$$

where N is the number of photons captured by the sensor and b is the standard error of the background of each pixel. In the case where the background noise is low, we can approximate this as

$$\sigma = \frac{s}{\sqrt{N}} \tag{4.5}$$

From this relationship, we can conclude a few things. As the standard deviation of the point spread function scales linearly with the Rayleigh criterion, single particle localization benefits from high-resolving microscopes the same as normal imaging does. Secondly, the localization accuracy scales as the square root of the number of photons collected, which means that the more light you capture, the more accurately you can localize the particle. For a back-of-the-envelope calculation, if you consider a microscopy system with a standard deviation of 200 nm and capturing only 100 photons, you would expect to be able to localize that particle to within 20 nanometers, a factor of 10 improvement. Of course, this only works well if the particle is well-isolated and there are no other particles within a diffraction limit. Techniques such as STORM and PALM have been developed for this case.

4.1.3 Plasmonic Brownian Microscopy

So, since isolated particles are naturally sparse objects, we can then imagine that our etalon array imaging method would be well-suited for particle localization. However, what application could this be useful for? A recently developed method called Plasmonic Brownian Microscopy [67] gives us a path for what might be possible with this kind of tracking system.
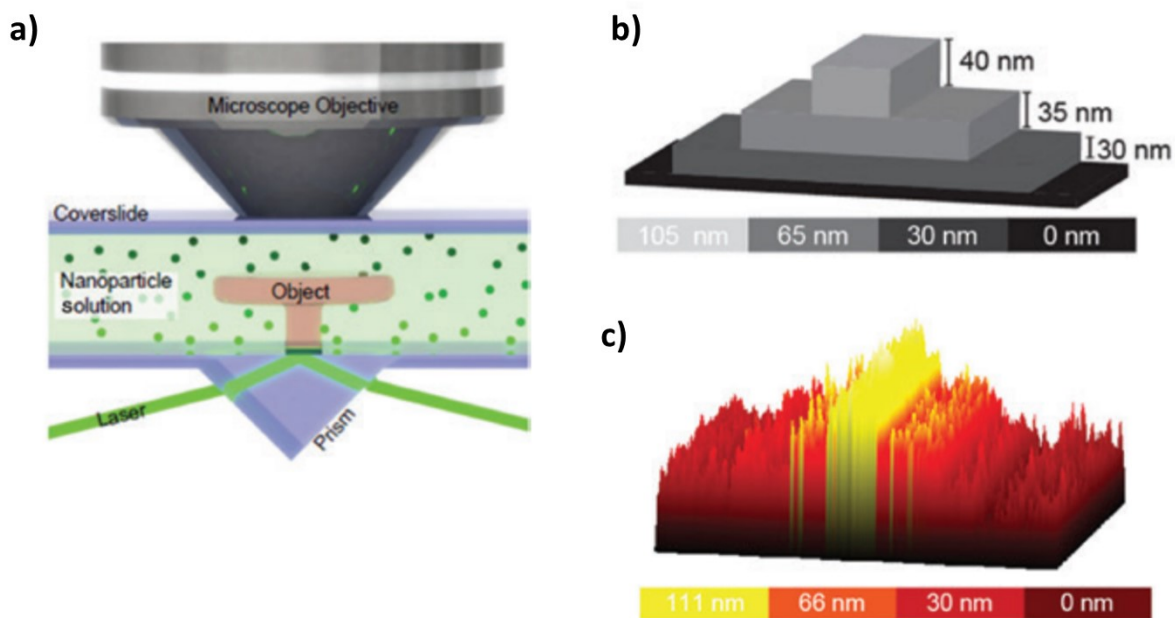
Figure 34: Plasmonic Brownian microscopy. a) Overview of the PBM setup. b) Fabricated object placed in the imaging plane of the microscope. c) Object profile recovered by PBM. [68]

Plasmonic Brownian Motion, or PBM, consists of a freely-diffusing fluid with plasmonic nanoparticles dispersed inside (see Figure 34). It is illuminated via total internal reflection, which will only illuminate particles that are very close to the boundary. Each particle is a 50 nm gold sphere, which is below the diffraction limit. Gold nanoparticles near the bottom surface will then scatter light into the microscope objective, and be imaged by a camera. Several hundred thousand images are taken over the course of many minutes For each image of the camera, there

will be many different particles in the imaging plane, which are then sent to a localization

algorithm to have their locations recorded. By building up an image composed of these many

thousands of points, it is then possible to recover information about the environment the particles

are floating in. For this paper, they were able to gather information about both the X-Y features

in their environment, as well as the Z-direction information. In short, the floating particles act

like freely-moving probes, and their Brownian motion in the fluid is used to sample their

environment to a high degree of detail.

It is here, though, that we can see some of the limits of PBT. Since PBT require the random

motion of particles to cover the entire area of interest it requires many images, sometimes in the

hundreds of thousands. Any improvement in the imaging speed will greatly speed up this

process.

Secondly, although the camera may be able to localize the particles, this neglects the fact

that Brownian diffusion happens on a multitude of different scales. If we look at Einstein's

Brownian diffusion equation [69]:

$$\overline{x^2} = 2Dt \tag{4.6}$$

where $\overline{x^2}$ is the second moment of the probability distribution of a diffusing particle, D is the

diffusivity of the particle, and t is the time that it is allowed to propagate. You can see from this

equation that we expect the second moment to be proportional to t, or in other words we expect

the distance that it travels away from the origin to be proportional to $\sqrt{t}$.

For a particle suspended in a fluid, we can model the diffusivity as:

$$D = \frac{RT}{6\pi\eta rN} \qquad (4.7)$$

where R is the universal gas constant, T is the temperature, η is the viscosity of the fluid, r is the particle radius, and N is Avogadro's number. For a 50 nm particle in water at room temperature, then we can expect to find the relationship of roughly $\sqrt{x^2} \approx 5 \times 10^{-6}\sqrt{t}\frac{m}{\sqrt{s}}$

For PBM, which operated at a frame rate of around 1 ms, this means that you can expect the particle to drift almost 160 nm during that time. So what you are measuring isn't really the location of the particle, but the average location of the particle. In order to get a truly high-resolution measurement of the environment with such a small particle, the imaging speed must be much faster.

4.2 Compressed sensing for particle localization

In order to do compressive sensing particle localization, a few things need to be considered. First, as mentioned in chapter 1, minimization of the l1 norm will lead the algorithm to a sparse solution. How, then, do we apply this to particle localization? The most straightforward way to do this is to utilize the fact that if we are projecting the pattern of the etalon arrays, this pattern is also subject to the diffraction limit. If we highly demagnify the image of our 10 x 10 etalon array, the pattern will be convolved with the point spread function. Since we are dealing with a discrete, rather than continuous, image, this means that the CS algorithm will converge towards the fewest number of pixels that are able to represent the recovered measurement. A further consequence of this is that our precision will be limited to the pixel size of our sensing matrix. Therefore, in order to convert our system into a particle

localization system, we will need to project a highly demagnified image of our etalon array, and measure the diffraction-limited sensing matrix at a high resolution. Figure 35 shows a simple simulation of this measurement process.
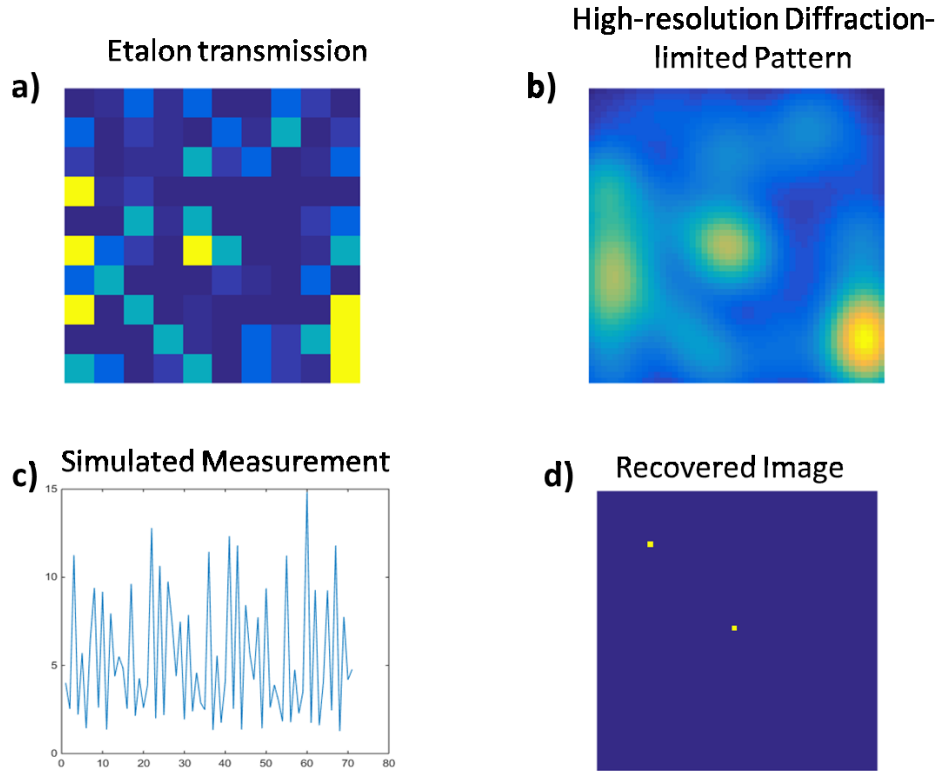
Figure 35: Simulated compressive localization imaging. a) An example of a projection pattern from a 10 x 10 array of etalons. b) What the image of the etalon array will look like if convolved by a high-resolution point spread function. c) A simulated measurement using the high-resolution pattern. d) The reconstructed image, showing the high-precision localization.

4.3 Experimental setup for high-speed Brownian etalon array imaging

In order to be able to measure these particles, we will need to be able to measure the optical signal from it. For sub-wavelength nanoparticles, this cross section can be very small- on

the order of only thousands of square nanometers [70], [71]. When given the fact that a diffraction-limited spot is already on the order of many tens of thousands of square nanometers, it becomes clear that we are going to want to be able to maximize our signal as much as possible.

Our first change was to replace our avalanche photodiode (MenloSystems APD210), which has a gain of roughly 2.5×10^5 V/W, with a photomultiplier tube (Horiba H10720), which when combined with an amplifier (Hamamatsu C6438-10) gives a gain of around 3.75×10^9 V/W, at the cost of a slower bandwidth (50 MHz vs 5 GHz). However, since our application is to be photon limited, this is a worthwhile tradeoff.

Secondly, we modified our optical setup. Since we now wished to do particle localization, and needed to deal with lower signal intensities, we wished to maximize both the numerical aperture and the magnification of our microscope objectives. The best commonly-available microscope objectives are 100x magnification with around 1.4 NA. As a result, however, they therefore have very small fields of view and focus depths, so it will be very difficult to align two of them in a confocal transmission setup. Therefore, we changed from a transmission mode setup to a reflection mode setup. Finally, since we are doing high-resolution localization, we also added additional 3x magnification lenses into both the projection and the detection paths. The new setup configuration is shown in Figure 36 and Figure 37.
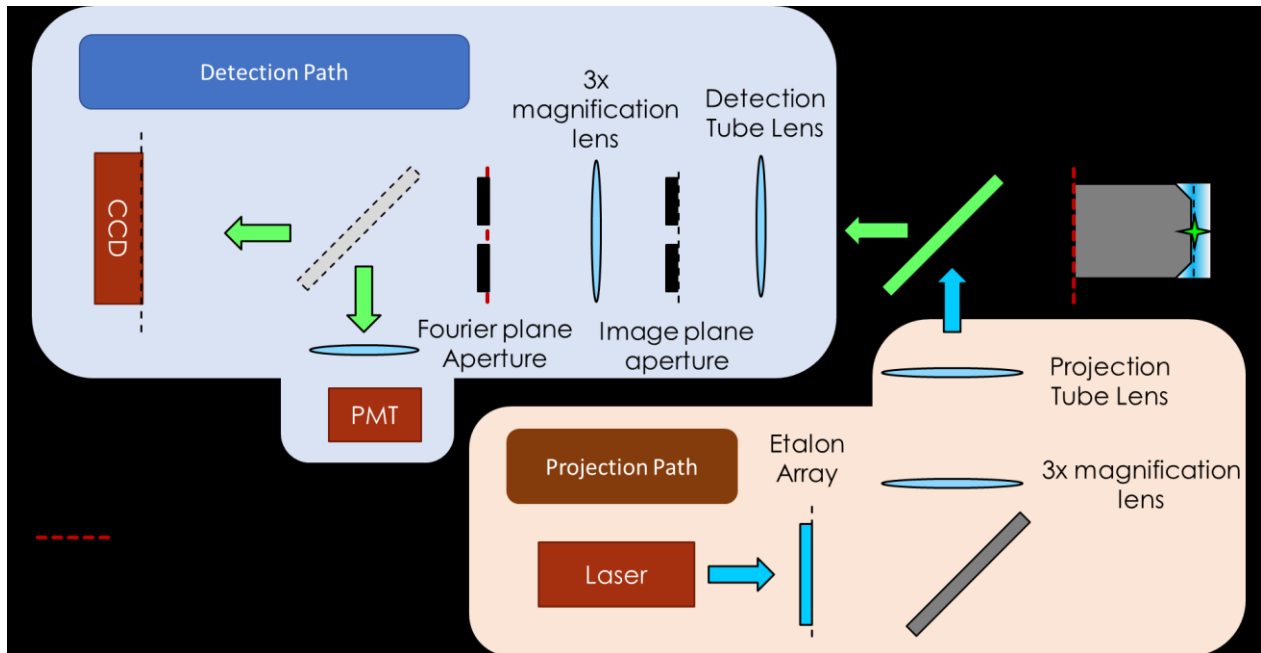
Figure 36: Overview of new optical setup for high-speed particle tracking
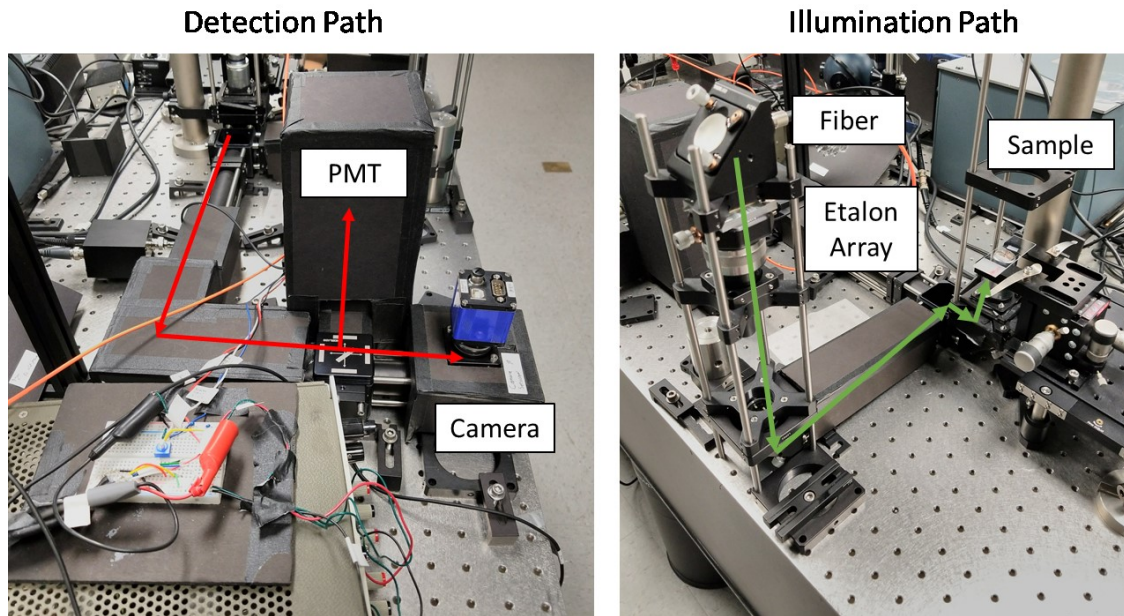
Figure 37: Photograph of optical system. Left: Detection path of the microscope. Emitted light from the sample is magnified and sent to a PMT for measurement, and a camera for alignment and focusing. Right: Illumination path. A fiber from the laser sends the light through an etalon array, after which its image is projected onto the sample plane.

4.4 High-speed tunable laser

Although we were able to use chromo-modal dispersion to get a 12 ns exposure time, this is insufficient for the type of localization we wished to do. First of all, inter-modal mixing meant that propagation lengths above 100 m of fiber resulted in no additional dispersion, but secondly, our laser, although it averaged around 25 mW in the visible range, this power was spread out throughout the entire visible spectrum, and so only had about .1 mW per nm, which would be a problem if we were limited to the bandwidth of a typical fluorescent probe (~50 nm).

Our requirement for our light source, then, was extremely high. As our sweep repetition rate would be the limiting factor of our imaging speed, we wanted something that could offer potentially a MHz sweep rate. This eliminated most forms of mechanical scanning, as they simply cannot reach those speeds. Secondly, it needed to have high power in a narrow bandwidth at each section of the sweep. Finally, we wanted it to be completely tunable, so that we could choose the laser parameters ourselves. The solution we found to this was to create a high-speed frequency-tunable external cavity diode laser.

4.4.1 External Cavity Diode Lasers
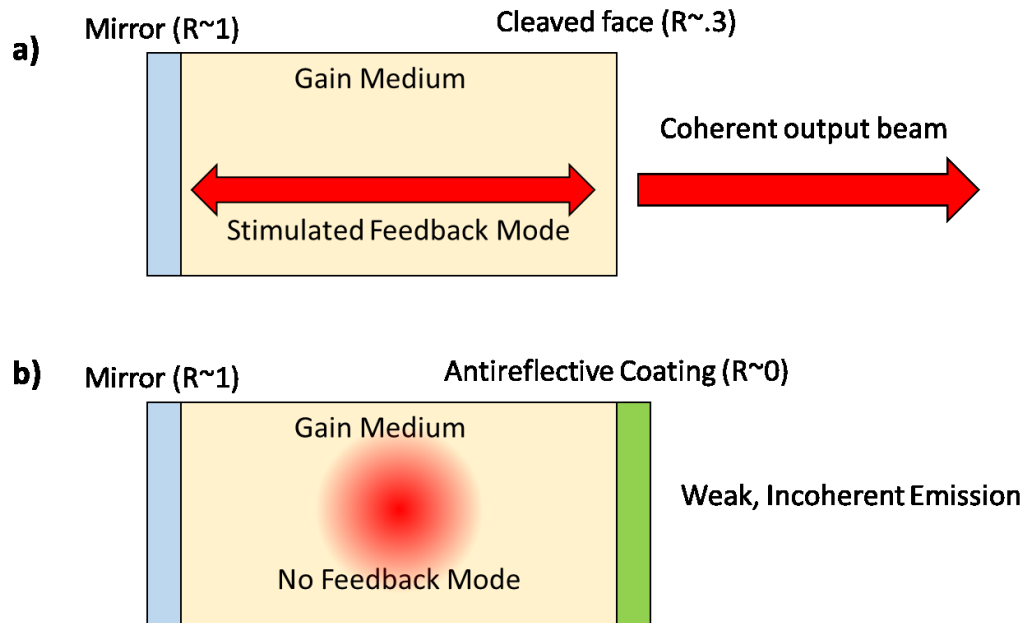
Figure 38: Laser diodes a) Typical laser diodes include a mirrored back face and a cleaved front face. The moderate reflectivity (~.3) of the front face is enough for stimulated emission. b) An anti-reflective coated laser diode has a low-reflectivity front face (R~0) and cannot lase on its own.

Typical laser diodes do not require an external cavity to lase. Since laser diodes have extremely high gain, they do not require a large cavity finesse in order to fulfil the conditions for stimulated emission. Therefore, the inherent reflectivity of the semiconductor material/air interface of a cleaved facet is enough to lase. However, laser diodes are also offered with an anti-reflective coating applied to the front face, which prevents any feedback into the gain medium. In order for an AR coated laser diode to produce a coherent laser, it must get this feedback from an optical system external to the laser, hence the term, 'external cavity diode laser', or ECDL [72]–[74].

There are many ways to introduce external feedback into the laser diode. The simplest is just a partially-reflective mirror (Figure 39a). This mirror, along with the laser diode, forms a

simple Fabry-Perot cavity, which then results in the stimulated emission. However, there are typically many spatial modes within the gain profile of the material, so it is difficult to predict which mode will dominate. Furthermore, this configuration has little control over the output wavelength.
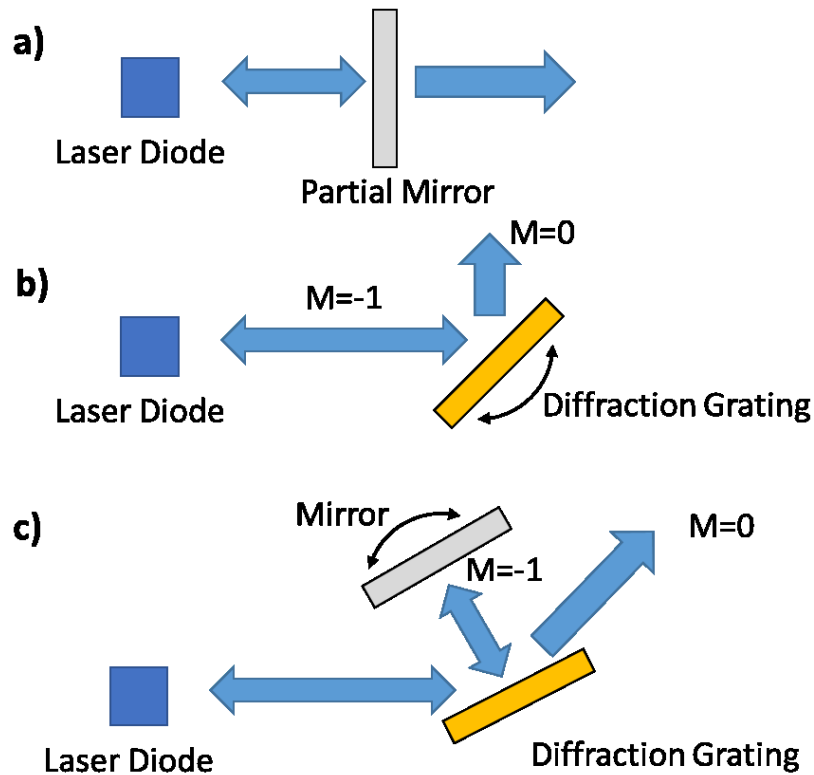
Figure 39: Common ECDL configurations. a) Simple etalon configuration. b) Littrow configuration. c) Littman-Metcalf configuration.

Indeed, the reason that external cavity diode lasers are so popular is that they can be constructed to select a specific output band. Two of the most common configurations, both using diffraction gratings, are shown in Figure 39 b,c. The first is the Littrow configuration [75], [76]. The Littrow configuration uses a diffraction grating in the beam path, for which diffraction orders follow the grating equation:

$$\sin\theta_1 - \sin\theta_2 = \frac{m\lambda}{d} \qquad (4.8)$$

where θ_1 and θ_2 are the input and output angles of the beams reflecting from the grating, m is an integer representing the order of the diffraction, λ is the wavelength of the light, and d is the distance between each groove in the grating. Since we want the grating to act as a retroreflector for the lasing wavelength, we will set $\theta = \theta_1 = -\theta_2$, so we can rewrite the equation as:

$$\frac{2d\sin\theta}{m} = \lambda \qquad (4.9)$$

From this equation, we can see that for a given angle and diffraction order, there will be only one wavelength that meets this condition. Since we typically want the highest efficiency reflection order, this means we usually choose m=1 (or equivalently m=-1). The result is that by simply changing the angle of the grating, we can tune the wavelength. In the simplest Littrow ECDLs, the 0 order output of the grating is then used as the output beam, since it is often the second most efficient order. The downside, however, is that the angle of the 0-order beam will change as the angle on the grating is tuned, which is not ideal for situations where the frequency has to be regularly adjusted.

Another configuration is the Littman-Metcalf configuration [77], where the first-order beam is sent to a mirror instead of reflecting back into the cavity. Instead of tuning the angle of the grating, the angle of the mirror is rotated to tune the wavelength. The derivation of the retroreflective condition is explored in the attached reference, but the ultimate result is this:

$$\lambda = \frac{d}{m}\left(\sin\theta_{grating} + \sin\theta_{mirror}\right) \qquad (4.10)$$

The advantage of the Littman-Metcalf configuration is that if using the m=0 output of the grating, then the angle of the output is independent of the wavelength of the laser. Furthermore, in the Littman-Metcalf configuration, the feedback path reflects off of the grating twice, which leads to a smaller line width of the laser.

So as demonstrated, external cavity diode lasers make it easy to create a laser with which one can tune the wavelength. However, all of the methods we have discussed require mechanical tuning of a diffraction grating. Both the Littman-Metcalf and the Littrow configuration cannot be used for high-speed tuning, so we have to create an ECDL with a faster tuning mechanism.

4.4.2 High-speed acousto-optic ECDL
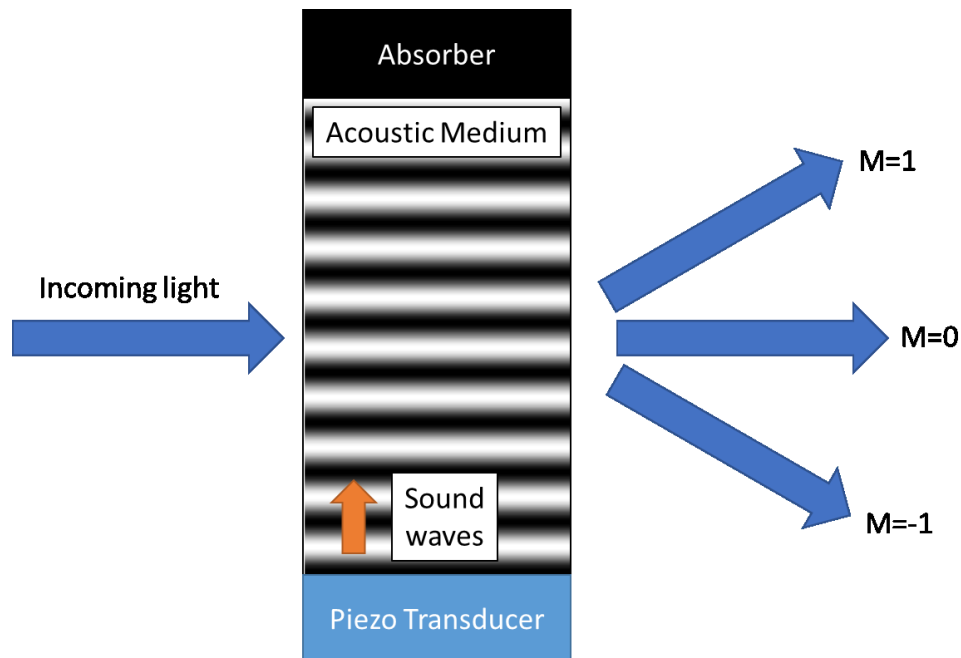
Figure 40: Acousto-optic Deflector. A transducer generates sound waves in a transparent material, and they travel down the length of the material before being absorbed at the other end. The sound waves form an electrically tunable diffraction grating.

The key element for our high-speed tunable laser is the acousto-optic is the acousto-optic

deflector (AOD) (see Figure 40). A piezoelectric transducer converts an RF electrical signal into

an ultrasonic acoustic wave in a transparent material. This acoustic wave travels down the

material and is absorbed at the other end. The index of refraction of the material is slightly

altered by the local pressure, and so forms a period index variation. The grating period will be

equal to the wavelength of the sound in the material:

$$\Lambda = \frac{v}{f} \tag{4.11}$$

where Λ is the wavelength of the acoustic wave, f is the RF frequency sent to the tranducer, and

v is the speed of sound in the material. Therefore, an AOD is essentially a diffraction grating that

can be tuned at high-speed by an electronic signal.

We can use the high-speed ability of the AOD in the following configuration [78], [79]:
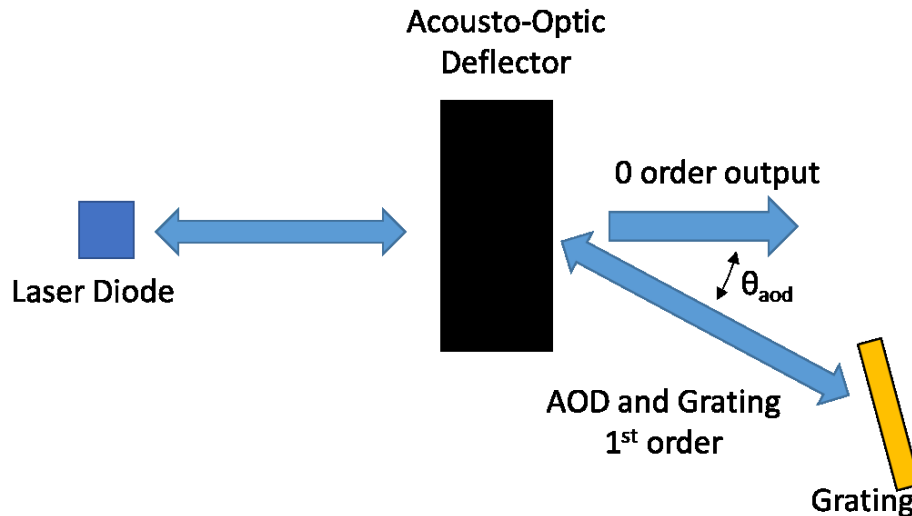
Figure 41: High-speed acousto-optic tunable ECDL.

The acousto-optic deflector splits the light into multiple diffraction orders. We then use an additional grating at an appropriate angle to reflect the wavelength that we desire back into the cavity. The 0-order transmission mode will be the output beam of the laser. To make the setup easier, we typically know both the frequency of highest efficiency on the AOD, as well as the peak wavelength of the laser diode that we will use. Therefore, to construct this laser, we can use the following relations assuming that the AOD is at an approximately normal angle:

$$\sin \theta_{AOD} = \frac{\lambda_{max}}{\Lambda} = \frac{\lambda_{max} f_{max}}{v}, \ 2d \sin \theta_{grating} = \lambda_{max} \tag{4.12}$$

where θ_{AOD} is the angle between the m=1 and m=0 mode, λ_{max} is the peak gain wavelength of the laser diode, f_{max} is the peak efficiency frequency of the AOD, v is the speed of sound in the AOD medium, d is the grating period, and $\theta_{grating}$ is the angle between the m=1 mode and the grating. This should be the peak power output of the laser, and we can then tune the wavelength of the laser around that point by tuning the frequency of the electronic RF signal.

4.4.3 Speed limit of the acousto-optic tunable laser

There are two fundamental limits to the speed at which we can tune the laser. The first is that since the AOD operates on acoustic waves, the fastest it can change the deflection is the time it takes for the acoustic wave to cross the diameter of the beam:

$$\tau_{aod} = \frac{D}{v} \tag{4.13}$$

where D is the diameter of the beam and v is the speed of sound in the material. For a back of the envelope calculation, we assume that our laser beam has a diameter of roughly 2 mm, and our AOD material is TeO$_2$, which has a v=4250 m/s, giving us an approximate τ_{aod}=470 ns, corresponding to a frequency cutoff of 2.1 MHz.

The other limit is that of our laser cavity itself. Since the laser itself is a resonator, the speed at which the light in it can be changed is related to the photon lifetime inside the cavity. Similar to the etalon we can calculate this photon lifetime:

$$\tau_{photon} = \frac{\tau_{round\ trip}}{1 - surival\ fraction} \tag{4.14}$$

$$= \frac{2L}{c\left(1 - R_{grating}(T_{aod})^2\right)}$$

where L is the cavity length, c is the speed of light in a vacuum, R$_{grating}$ is the reflective efficiency of the M=1 mode, and T$_{aod}$ is the transmission efficiency of the M=1 mode in the acousto-optic deflector. Note that T$_{aod}$ is squared, since the beam must travel through the AOD twice in a round trip. If we assume that a L=10 cm, R$_{grating}$=.7, and T$_{aod}$=.6, we can estimate that τ_{photon}=8.9x10^{-10} seconds, or around 1 GHz. So between the two factors, we anticipate the acousto-optic device to be the limiting factor.

4.4.4 Laser construction and testing
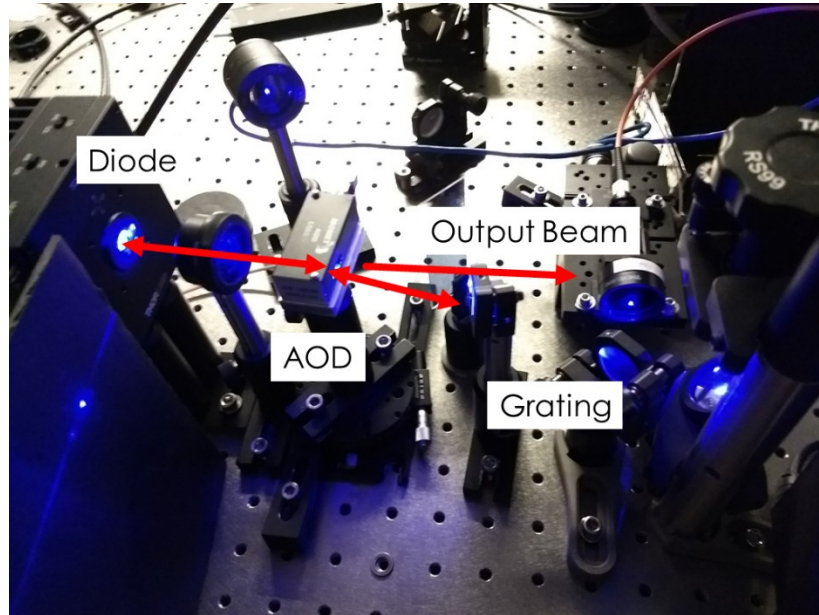
Figure 42: Photograph of the completed setup with a blue (450nm) laser diode.
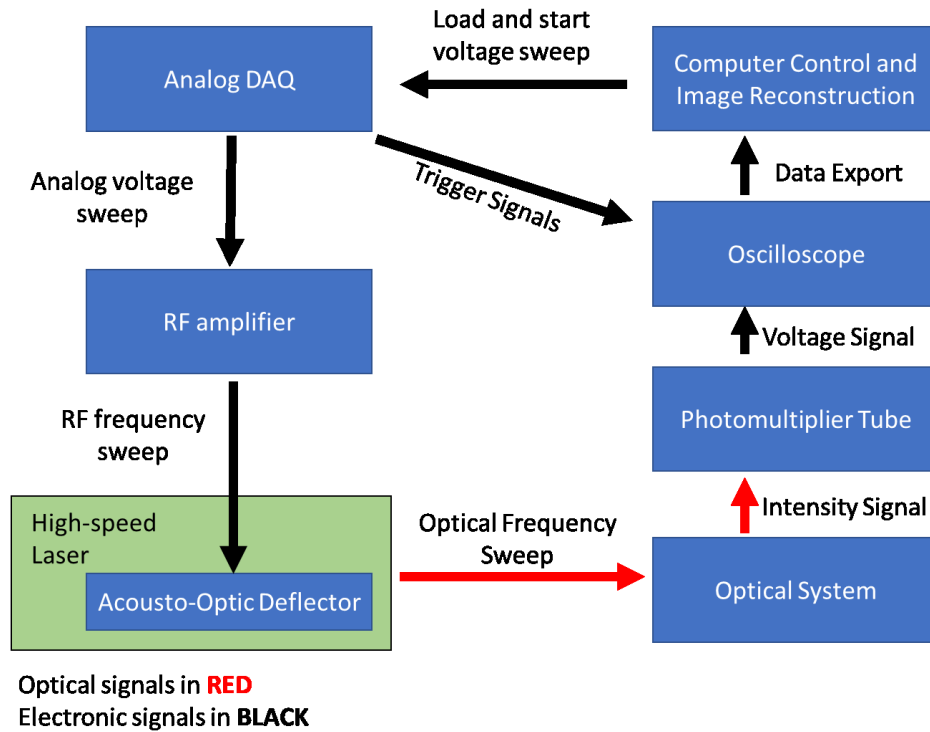
Figure 43: Diagram of control electronics

Figure 42 shows the image of our tunable high-speed laser. Our laser was constructed

using a temperature controlled diode housing (Thorlabs DCLDM9) driven by a diode controller

(Thorlabs LDC200C) and a temperature controller (TED200C). An AOD (Isomet LS55-75V)

was used driven by an RF driver (Isomet 620C-75). The grating was a 1200/mm ruled grating

with a 500nm blaze (Thorlabs GR13-120S). Over the course of the build we were able to test two

different diodes, a 460 nm center blue diode (Nichia NDBA116T) and a 670 nm centered red

diode (Eagleyard EYP-RWE-0670-00702-1000-SOT02-0000). The RF driver was controlled by

an analog voltage from a DAQ (MccDAQ USB-1208HS-4A0) that was controlled by a computer

(see Figure 43).

After roughly aligning the optical components together, we then tuned the alignment of the grating until maximum lasing intensity was achieved. After lasing was achieved, we adjusted the power of the AOD to reach the maximum output power. Unfortunately, the Nichia laser diode was damaged during alignment, so the following results only include measurements for the Eagleyard diode.
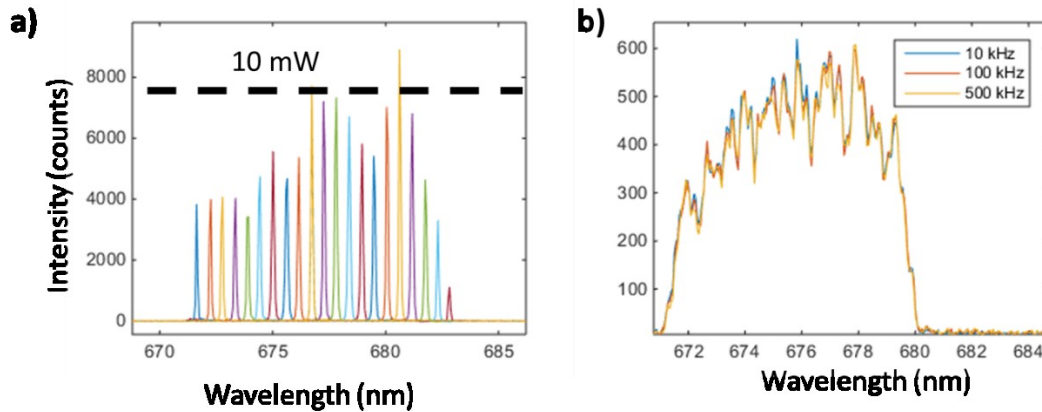
Figure 44: High-speed scanning ECDL spectrometer measurements. a) Spectrometer output for a full sweep of the lasing output. The dotted line represents a 10 mW power output. b) Spectrum results for a full sweep of 100 different voltages/frequencies at different speeds.

The spectral output of the high-speed ECDL is shown in Figure 44. We can see that the laser maintains a relatively high power for a roughly 11 nm bandwidth, and that its spectral output and power do not decrease for scans up to 500 kHz (the maximum speed due to limitations of the DAQ). The high-speed scanning demonstration of the laser is shown in Figure 45. By scanning the laser across a wide variety of scanning speeds, we can see that the detected intensity is independent of the scanning speed, showing that the laser is working at the currently highest achievable speed of 500 kHz, limited by our DAQ output speed.
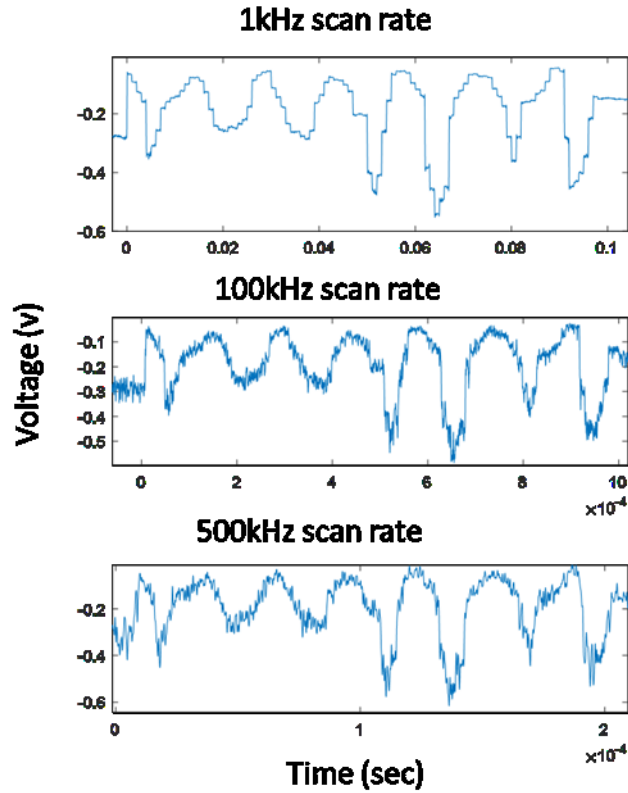
Figure 45: Time performance of the high-speed ECDL under different scanning rates with a random mask.

4.5 New etalon array and calibration

Our previous etalon array was designed around a bandwidth from roughly 500-700 nm, and so was relatively thin (1.5-3.5 um). However, we are now using a laser with a much smaller bandwidth (~10 nm), and so our etalons must be correspondingly thicker. This was done by fabricating the new etalons around a standard cover slip (~150 um glass) and using the same grayscale electron beam lithography method as described before. In addition, as we wish to use these etalons patterns to be slightly diffraction-limited, we fabricated them at a smaller lateral size of 30 um. This way, when they were sent through a 3x demagnifier and the 100x objective lens, they would be projected at a resolution of only 100 nm, which is below the 200 nm

diffraction-limited resolution of a 1.5 NA oil immersion lens. In order to characterize this high-resolution imaging pattern, we then place a reflective silver sample into the sample holder and focus onto the image of the etalon array. We then step through each individual wavelength that we wish to use and take a camera image of the resulting transmission pattern. This gives us our sensing matrix.
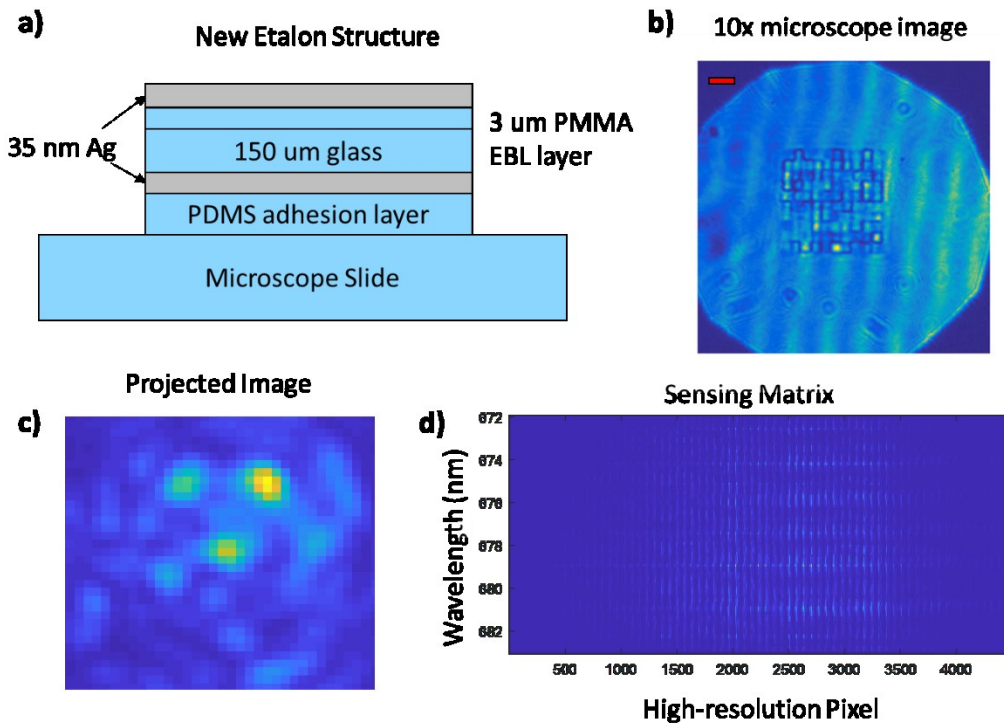
Figure 46: Thick etalon overview. a) Diagram of the etalon array structure. b) 10x microscope transmission image of the etalon. The red scale bar is 100 um. c) An example of a diffraction-limited projection pattern that is focused onto the sample plane. d) The collected sensing matrix for the entire ECDL wavelength range.

4.6 Preliminary results and discussion

In this section, we have demonstrated the potential benefits of particle tracking imaging with the discussion of plasmonic Brownian microscopy, and how the etalon array compressive sensing imager is uniquely suited for a high-speed particle tracking technology. In order to adapt

our system for particle tracking we designed and constructed a high-speed external cavity diode laser with frequency control via an acousto-optic deflector that has a maximum theoretical switching speed of 2 MHz and a frequency range from 672-683 nm at a power of roughly 10 mW.
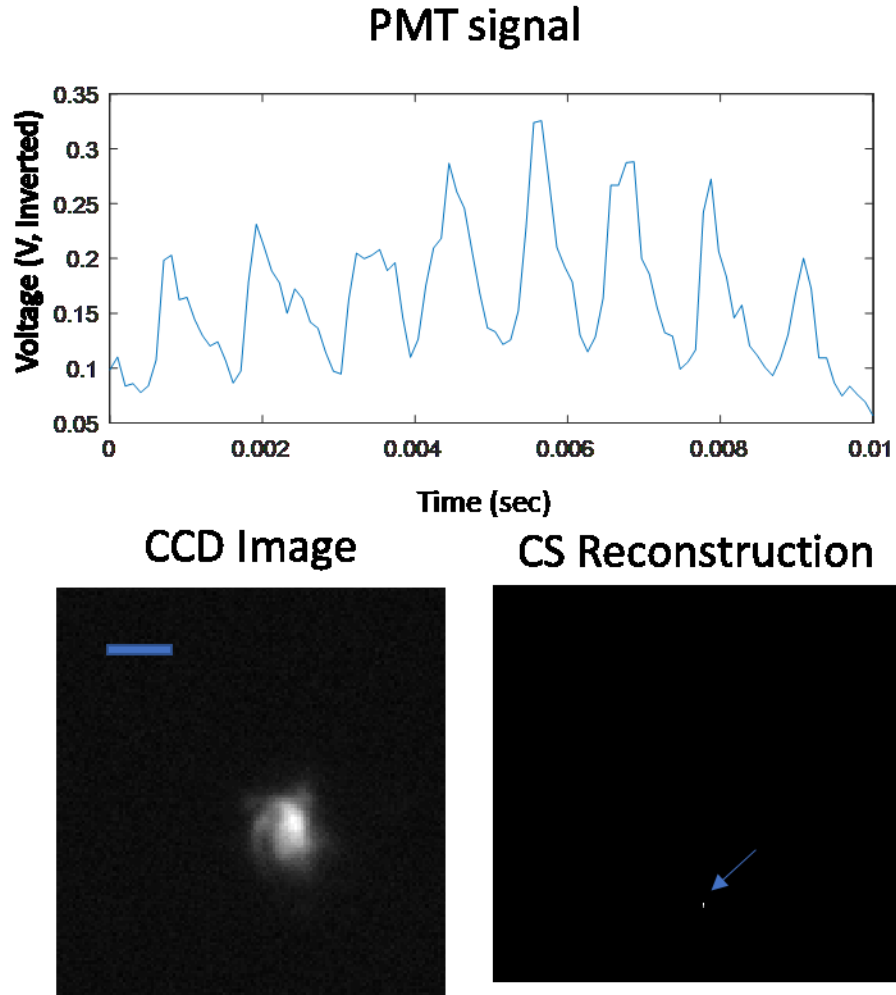
Figure 47: Preliminary Results. Top: The PMT signal detected during a frequency sweep. Bottom left: An image of a fluorescent bead cluster in the sample plane. The scale bar is 400 nm. Bottom right: Compressive Sensing localization of the data. The pixel size is approximately 20 nm.

Preliminary results are shown in Figure 47. Although some individual test images have been demonstrated, we are continuing to work on producing the full-scale Brownian motion microscopy.

Chapter 5 – Etalon Array Reconstructive Spectrometry

In the previous part, we discussed the use of compressive sensing and a frequency-dependent mask in order to form an image. In a sense, we were using a known light spectrum and a known frequency-to-space encoder to reconstruct spatial information. However, it is entirely possible to reverse this process, and use known spatial information, and a known frequency-to-space encoder, to recover the frequency information of the incoming light. As spectrometry is used in nearly every field of scientific research, there is a constant effort to produce spectrometers that are cheaper, more compact, and lighter. This chapter explains how we use our etalon array to do reconstructive spectrometry, instead of imaging.

5.1 Background on spectrometry
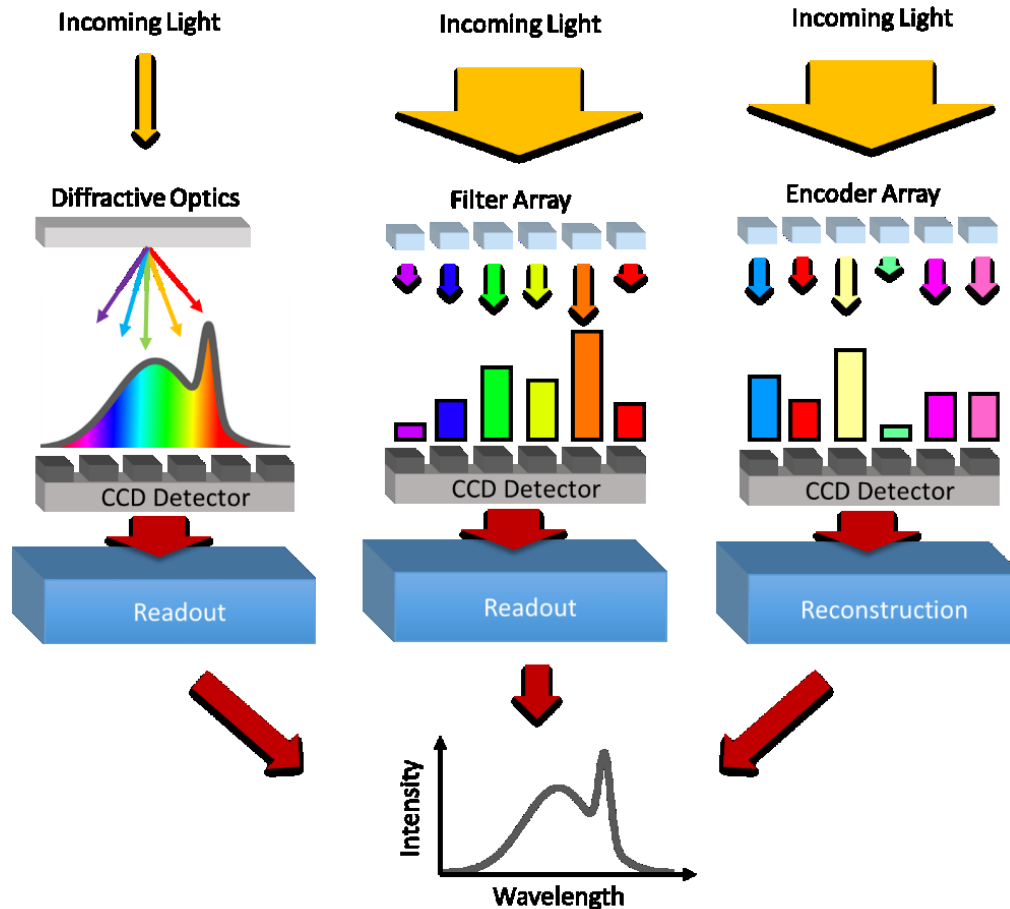
Figure 48: Overview of typical spectrometer technologies. Left: A grating-based spectrometer uses a diffraction grating to spread wavelengths out in space. Center: A filter-array spectrometer uses individual bandpass filters for each pixel measurement. Right: A reconstructive spectrometer uses an array of encoders to scramble the wavelengths of the incoming light, and the spectrum is reconstructed with a computer algorithm. [80]

The most common type of spectrometer in use is the grating-based spectrometer [81]. In a grating spectrometer, a diffraction grating is used to split incoming light into component colors, and then those colors are focused onto a linear detector array so that each pixel measures a specific wavelength (Figure 48). However, these spectrometers require light to be propagated after the diffractive element in order to separate the light, so there are some challenges in making a

spectrometer in a compact geometry. One method, however, of creating compact spectrometers can be found using filter array spectrometers [82], [83]. Instead of separating out the light with diffraction, these spectrometers instead use an array of filters in front of each camera element, which allows them to be placed directly on the sensor for a robust and compact package. Both methods traditionally map each pixel to a wavelength band for direct one-to-one mapping of the spectrum, but reconstructive spectrometry, much like reconstructive imaging, has been developing recently [84]–[88]. Instead of a simple one-to-one mapping, reconstructive spectrometers instead spatially encode the incoming light using wavelength-sensitive elements, and then the original spectrum is recovered via a computer reconstruction.

5.2 Theory of Etalon Array Spectrometry

The method of reconstructive spectrometry is very similar to reconstructive imaging. If an incoming spectrum $S(\lambda)$ is encoded by a series of m optical elements with known transmission spectra $T_i(\lambda)$, then the transmitted intensity for each optical element I_i will be:

$$I_i = \int T_i(\lambda)S(\lambda)d\lambda, i = 1,2,\dots m \tag{5.1}$$

With the wavelength basis discretized, it can be seen that it can also be written as

$$I_i = [T]_{i,\lambda}S_\lambda \tag{5.2}$$

which matches the form for compressive sensing as described above. In essence, the difference between etalon array reconstructive imaging and etalon array reconstructive spectrometry is that the sensing matrices are transposes of each other. In the former, we are using a spatial mask to

encode information in frequency, while in the latter we are using it to transform information in frequency into information in space.

The resolution limit of a spectrometer based on multiple order etalon transmission has been previously explored in other work [88], and so we can say that the Nyquist-limited resolution is expected to be:

$$\Delta\sigma > \frac{1}{2d_r F} \tag{5.3}$$

where d_r is the range of cavity lengths and $F = \pi\sqrt{R}/(1 - R)$ is the finesse of the cavity, with R as the reflectivity of the etalon surfaces. One can see that the result of this is that increasing the thickness or finesse of the cavity will increase the spectral resolution. A back of the envelope calculation shows that if we use our experimentally obtained parameters, (d_r=2000 nm and R=.7), we can expect a Nyquist resolution close to 10 nm at a wavelength of 600nm.

To test this, we simulated an etalon array spectrometry measurement on a Gaussian spectrum with a peak at 600 nm. We then varied the resolution of the spectrum basis in the wavelength space, and attempted reconstruction (See Figure 49). We can see that while the simulation is successful for sampling periods above to 4 nm, period below that will begin to diverge from the original spectrum. The sampling period is half of the Nyquist resolution, so we can empirically estimate the resolution limit of our fabricated etalon array to be around 8 nm, which is close to the estimated value. From the observed etalon spectra, this seems reasonable, as we expect the resolution to be close to the etalon spectrum full-width half maximum (FWHM), which we measured to be around 7 nm.
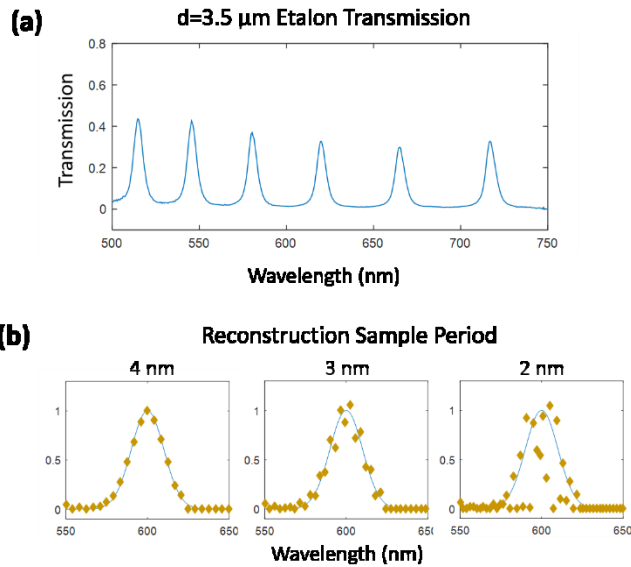
Figure 49: Simulation of resolution limit for our etalon array. a) An example measured transmission from an etalon, showing a full-width half maximum of around 7 nm. b) Simulated spectroscopy of a spectrum at different resolutions. [89]

5.3 Experimental Imaging Setup
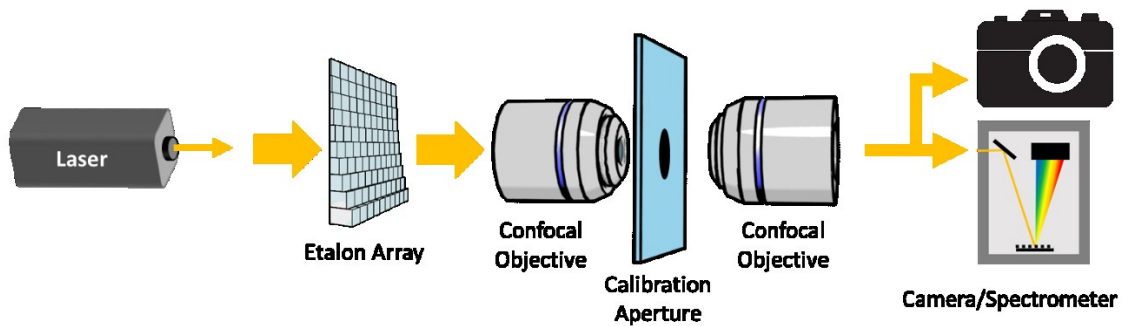
Figure 50: Overview of the etalon array reconstructive spectrometer. [89]

Our method for etalon array reconstructive spectrometry is shown in Figure 50. We fabricate an etalon array using the same methods discussed in Chapter 3, and place it in the imaging

plane of a camera sensor. The parameters of the etalon array are the same as in chapter 3, with 1.5-3.5 um cavity thicknesses distributed across a 10 x 10 array, and surrounded with 30 nm silver films on both sides. In order to measure the transmission properties of the etalon, we similarly use an aperture to directly measure the transmission spectrum of each etalon individually.

Our measurement process is the following: we take a light source of interest, and couple it into a fiber. Afterwards, the image of the etalon array is projected onto our camera sensor, and a picture is taken. We can then process the image to obtain one intensity value for each etalon, and use it in the reconstruction algorithm along with the known transmission sensing matrix.

5.4 Experimental Results
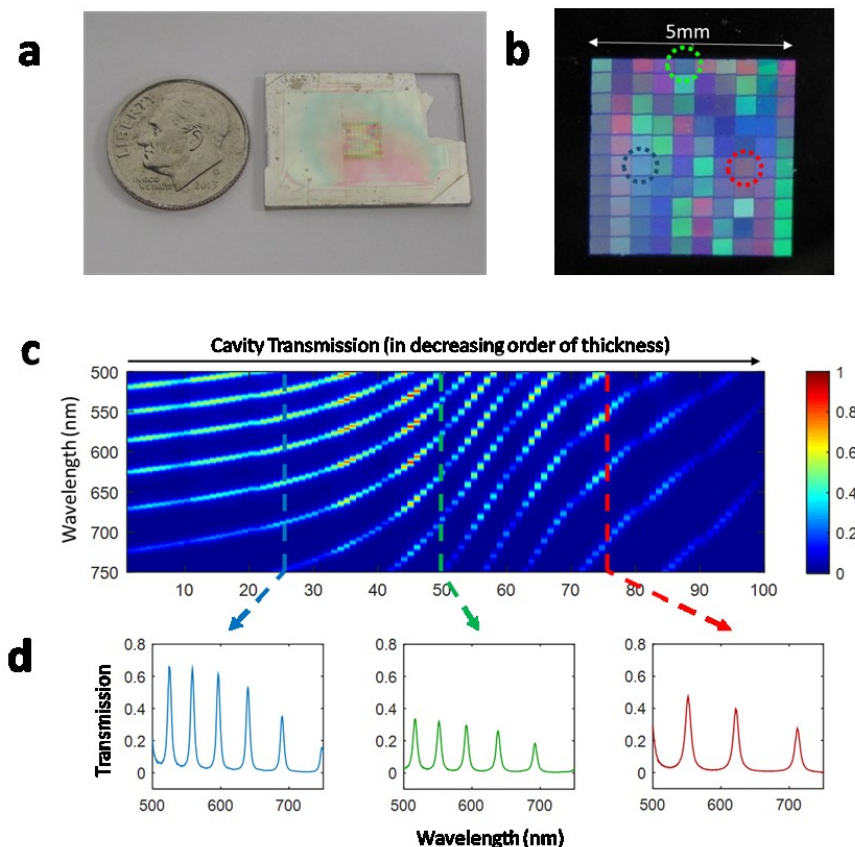
Figure 51: Etalon array properties and sensing matrix. a) Photograph of our fabricated etalon array next to a dime for scale. b) Close-up of the etalon array area back-illuminated by fluorescent lighting. c) Measured cavity transmission for each etalon across the visible band. d) Example transmissions showing different etalon resonance spacings. [89]

The experimental spectrometry obtained is illustrated in Figure XXXX. Our sensing matrix was measured using our spectrometer (Andor Shamrock SR-303i, measured from 400-970nm at a resolution of .55nm). To provide sample spectra for measuring, we used a tunable bandpass filter with our supercontinuum laser (NKT SuperK COMPACT with VARIA tunable filter), and set it to a variety of different output spectra. The reconstruction results are shown in Figure 52. In

practice, we were able to achieve a reconstruction resolution of around 4 nm, which is equal to a Nyquist-limited resolution of 8 nm.
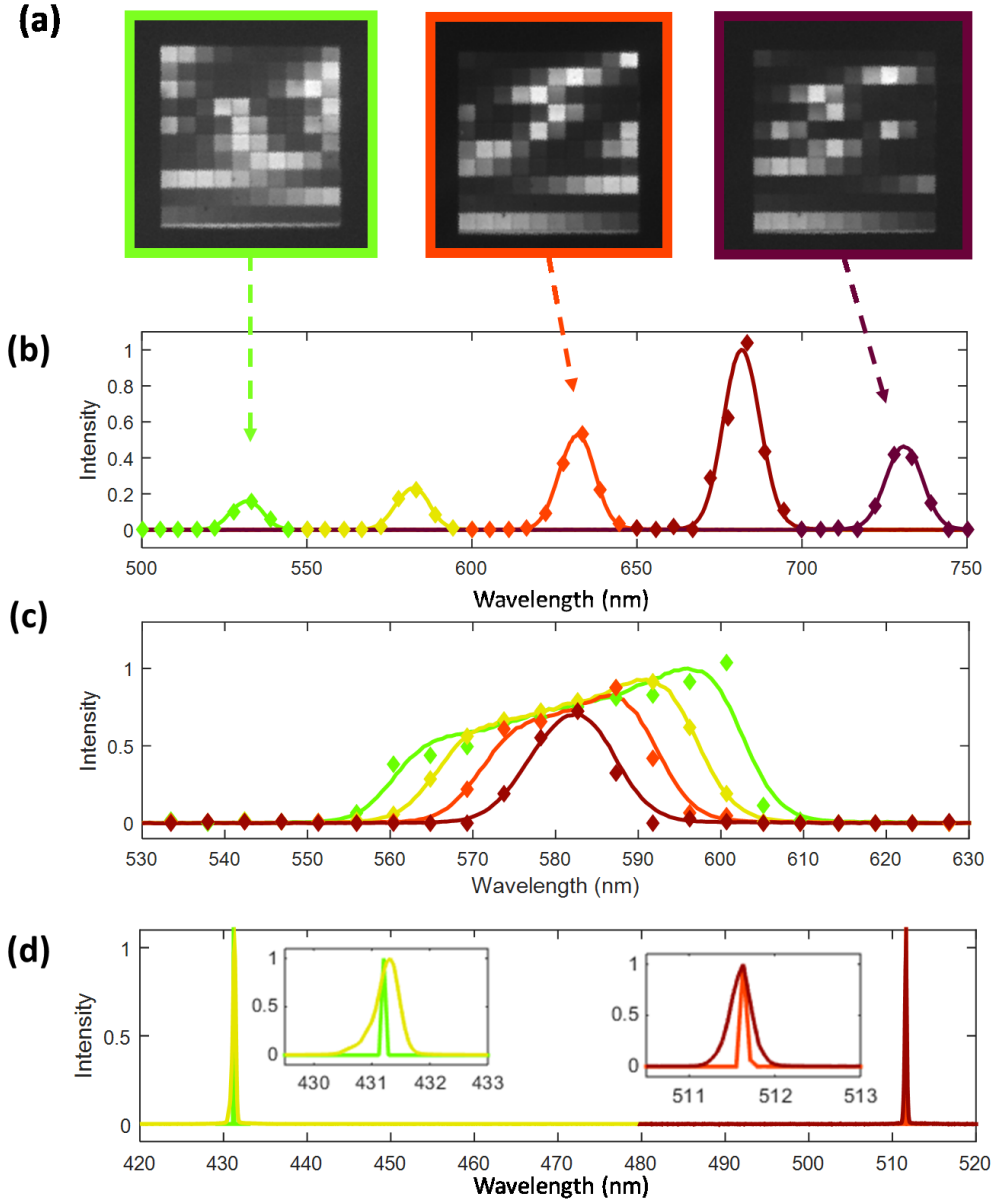
Figure 52: Experimental spectrometry results. a) Three different camera images take for the reconstructive spectrometry measurement. b) Five different reconstructed spectra at different wavelengths. Reconstruction is shown as diamonds, and the spectrometer comparsion is shown as solid lines. The of the corresponding camera images are shown with arrows. c) Reconstruction results for several different bandwidths. d) Reconstruction vs spectrometer measurements for two laser spectra.

One advantage of our spectrometry system is also that we can take prior information into account during the reconstruction. Since we are using a compressed sensing algorithm, if we know that our signal is a roughly monochromatic or extremely sparse signal, than we can be extremely aggressive in our reconstruction. Figure 52d shows the spectrometry result of two different lasers. By setting the sparsity constraints to be high, we were able to accurately localize the spectrum of the laser to within .12 nm, far below the conventional resolution limit. For the case of peak wavelength localization, the limit then is on the accuracy of our calibration.

Chapter 5, in part, is a reprint of the material as it appears in Scientific Reports, 2017, 7, 25240. Eric Huang, Qian Ma, Zhaowei Liu, "Ultrafast Imaging using Spectral Resonance Modulation". The dissertation author was the first author of this paper.

Chapter 6: Future direction and summary

In this work, we have demonstrated the use of etalon arrays as a key component in both high-speed imaging and spectrometry. Etalons provide a highly tunable method for creating unique spectral fingerprints, and so are ideal for use in encoding light. Using grayscale electron beam lithography, we are able to fabricate 3D staircase structures, allowing us to precisely shape the etalon resonators for the appropriate transmission spectra. Combining our etalon array with reconstructive sensing and imaging provides for many unique capabilities.

The ultrafast etalon array reconstructive imaging technique uses an array of etalons to perform a high-sped frequency to space encoding. When combined with a high-speed frequency sweep and a single photodetector, it combines both the speed advantages from the increased measurement efficiency due to compressed sensing, as well as taking advantage of the imaging speed allowed due to the high speed frequency sweep. Using chromo-modal dispersion and a

supercontinuum laser, we were able to image at a speed of 25 kHz and an exposure time of 12 nanoseconds.

The properties of high speed etalon array imaging makes it ideal for high-speed particle tracking and localization. Due to the inherent sparsity of the expected images, the compressive sensing algorithm can be run very aggressively. Furthermore, techniques such as dual-stage localization can be used to assist in recovering results. We have demonstrated the working principle behind this technology, and has great promise in the type of high-speed particle tracking that will allow us to do real-time Brownian motion tracking.

Finally, the etalon array concept can also be used for spectrometry instead of imaging. Whereas the imager can be thought of as taking a known spectrum and mask to recover an unknown image, the etalon array reconstructive spectrometer instead uses a known spatial pattern and mask to recover an unknown spectrum. This type of instrument can be fabricated by putting the etalon array directly on top of a camera sensor, allowing for the resulting spectrometer to be lightweight, compact, and durable. When combined with an etalon array constructed of inexpensive material, this means that the entire spectrometer can also be low-cost. We were able to demonstrate general spectrometry across a wide bandwidth range, as well as demonstrate wavelength localization of sparse spectral signals. Further work remains to adapt this technology to other areas such as hyperspectral imaging.

Bibliography

[1] S. Manley, J. Gillette, G. Patterson, … H. S.-N., and undefined 2008, "High-density mapping of single-molecule trajectories with photoactivated localization microscopy," *nature.com*.

[2] H. Shroff, H. White, and E. Betzig, "Photoactivated Localization Microscopy (PALM) of Adhesion Complexes," in *Current Protocols in Cell Biology*, Hoboken, NJ, USA: John Wiley & Sons, Inc., 2013.

[3] E. Betzig, G. Patterson, … R. S.-, and undefined 2006, "Imaging intracellular fluorescent proteins at nanometer resolution," *science.sciencemag.org*.

[4] M. Rust, M. Bates, X. Z.-N. methods, and undefined 2006, "Sub-diffraction-limit imaging by stochastic optical reconstruction microscopy (STORM)," *nature.com*.

[5] M. G. L. Gustafsson, "Surpassing the lateral resolution limit by a factor of two using structured illumination microscopy," vol. 198, no. January, pp. 82–87, 2000.

[6] S. Hell, J. W.-O. letters, and undefined 1994, "Breaking the diffraction resolution limit by stimulated emission: stimulated-emission-depletion fluorescence microscopy," *osapublishing.org*.

[7] "Eadweard Muybridge - Sallie Gardner at a Gallop." [Online]. Available: http://www.sfmuseum.org/hist3/sallie.html. [Accessed: 06-Mar-2018].

[8] P. W. W. Fuller, "An introduction to high speed photography and photonics," *Imaging Sci. J.*, vol. 57, no. 6, pp. 293–302, Dec. 2009.

[9] K. Nakagawa, A. Iwasaki, Y. Oishi, R. Horisaki, A. Tsukamoto, A. Nakamura, K. Hirosawa, H. Liao, T. Ushida, K. Goda, F. Kannari, and I. Sakuma, "Sequentially timed all-optical mapping photography (STAMP)," *Nat. Photonics*, vol. 8, no. 9, pp. 695–700, Sep. 2014.

[10] M. El-Desouki, M. Jamal Deen, Q. Fang, L. Liu, F. Tse, and D. Armstrong, "CMOS Image Sensors for High Speed Applications," *Sensors*, vol. 9, no. 12, pp. 430–444, Jan. 2009.

[11] R. Kodama, P. A. Norreys, K. Mima, A. E. Dangor, R. G. Evans, H. Fujita, Y. Kitagawa, K. Krushelnick, T. Miyakoshi, N. Miyanaga, T. Norimatsu, S. J. Rose, T. Shozaki, K. Shigemori, A. Sunahara, M. Tampo, K. A. Tanaka, Y. Toyama, T. Yamanaka, and M. Zepf, "Fast heating of ultrahigh-density plasma as a step towards laser fusion ignition," *Nature*, vol. 412, no. 6849, pp. 798–802, Aug. 2001.

[12] H. R. Petty, "Spatiotemporal chemical dynamics in living cells: From information trafficking to cell physiology," *Biosystems*, vol. 83, no. 2–3, pp. 217–224, Feb. 2006.

[13] A. Grinvald, R. D. Frostig, R. M. Siegel, and E. Bartfeld, "High-resolution optical imaging of functional brain architecture in the awake monkey.," *Proc. Natl. Acad. Sci.*,

vol. 88, no. 24, pp. 11559–11563, Dec. 1991.

[14]   T. M. Squires and S. R. Quake, "Microfluidics: Fluid physics at the nanoliter scale," *Rev. Mod. Phys.*, vol. 77, no. 3, pp. 977–1026, Oct. 2005.

[15]   T. G. ETOH, C. VO LE, Y. HASHISHIN, N. OTSUKA, K. TAKEHARA, H. OHTAKE, T. HAYASHIDA, and H. MARUYAMA, "Evolution of Ultra-High-Speed CCD Imagers," *Plasma Fusion Res.*, vol. 2, no. S1021, pp. S1021–S1021, 2007.

[16]   "Operating principle of a digital streak camera." [Online]. Available: https://www.researchgate.net/figure/Operating-principle-of-a-digital-streak-camera_fig1_291697545. [Accessed: 06-Mar-2018].

[17]   A. Takahashi, M. Nishizawa, Y. Inagaki, M. Koishi, and K. Kinoshita, "New Femtosecond Streak Camera with Temporal Resolution of 180fs," *Proc. SPIE 2116*, pp. 275–284, May 1994.

[18]   A. Velten, T. Willwacher, … O. G.-N., and undefined 2012, "Recovering three-dimensional shape around a corner using ultrafast time-of-flight imaging," *nature.com*.

[19]   A. Velten, E. Lawson, A. Bardagjy, … M. B.-A. S. 2011, and undefined 2011, "Slow art with a trillion frames per second camera," *dl.acm.org*.

[20]   G. Gariepy, N. Krstajić, R. Henderson, … C. L.-N., and undefined 2015, "Single-photon sensitive light-in-fight imaging," *nature.com*.

[21]   C. Buehler, C. Y. Dong, P. T. So, T. French, and E. Gratton, "Time-resolved polarization imaging by pump-probe (stimulated emission) fluorescence microscopy.," *Biophys. J.*, vol. 79, no. 1, pp. 536–49, Jul. 2000.

[22]   C. Porneala and D. A. Willis, "Observation of nanosecond laser-induced phase explosion in aluminum," *Appl. Phys. Lett.*, vol. 89, no. 21, p. 211121, Nov. 2006.

[23]   A. Barty, S. Boutet, M. Bogan, … S. H.-R.-N., and undefined 2008, "Ultrafast single-shot diffraction imaging of nanoscale dynamics," *nature.com*.

[24]   M. M. Gabriel, J. R. Kirschbrown, J. D. Christesen, C. W. Pinion, D. F. Zigler, E. M. Grumstrup, B. P. Mehl, E. E. M. Cating, J. F. Cahoon, and J. M. Papanikolas, "Direct Imaging of Free Carrier and Trap Carrier Motion in Silicon Nanowires by Spatially-Separated Femtosecond Pump–Probe Microscopy," *Nano Lett.*, vol. 13, no. 3, pp. 1336–1340, Mar. 2013.

[25]   K. Goda, K. K. Tsia, and B. Jalali, "Serial time-encoded amplified imaging for real-time observation of fast dynamic phenomena.," *Nature*, vol. 458, no. 7242, pp. 1145–9, Apr. 2009.

[26]   D. R. Solli, J. Chou, and B. Jalali, "Amplified wavelength–time transformation for real-time spectroscopy," *Nat. Photonics*, vol. 2, no. 1, pp. 48–51, Jan. 2008.

[27]   K. Goda and B. Jalali, "Dispersive Fourier transformation for fast continuous single-shot measurements," *Nat. Photonics*, vol. 7, no. 2, pp. 102–112, Jan. 2013.

[28]   K. Tsia, K. Goda, D. Capewell, B. J.-O. express, and undefined 2010, "Performance of

serial time-encoded amplified microscope," *osapublishing.org*.

[29] E. D. Diebold, B. W. Buckley, D. R. Gossett, and B. Jalali, "Digitally synthesized beat frequency multiplexing for sub-millisecond fluorescence microscopy," *Nat. Photonics*, vol. 7, no. 10, pp. 806–810, Sep. 2013.

[30] E. J. Candes and M. B. Wakin, "An Introduction To Compressive Sampling," *IEEE Signal Process. Mag.*, vol. 25, no. 2, pp. 21–30, Mar. 2008.

[31] Y. Eldar and G. Kutyniok, *Compressed sensing: theory and applications*. 2012.

[32] J. M. Bioucas-dias, M. A. T. Figueiredo, S. Member, and A. Iterative, "A New TwIST : Two-Step Iterative Shrinkage / Thresholding Algorithms for Image Restoration," pp. 1–13, 2007.

[33] M. Figueiredo, … R. N.-I. J. of selected, and undefined 2007, "Gradient projection for sparse reconstruction: Application to compressed sensing and other inverse problems," *ieeexplore.ieee.org*.

[34] D. L. Donoho, "Compressed sensing," *IEEE Trans. Inf. Theory*, vol. 52, no. 4, pp. 1289–1306, Apr. 2006.

[35] S. B. Kwangmoo Koh, Seung-Jean Kim, K. Koh, S.-J. Kim, S. P. Boyd, and S. B. Kwangmoo Koh, Seung-Jean Kim, "An interior-point method for large-scale l1-regularized logistic regression.," *J. Mach. Learn. Res.*, vol. 8, no. 8, pp. 1519–1555, 2007.

[36] S. S. Chen, D. L. Donoho, and M. A. Saunders, "Atomic Decomposition by Basis Pursuit," *SIAM Rev.*, vol. 43, no. 1, pp. 129–159, Jan. 2001.

[37] A. Beck and M. Teboulle, "A Fast Iterative Shrinkage-Thresholding Algorithm for Linear Inverse Problems," *SIAM J. Imaging Sci.*, vol. 2, no. 1, pp. 183–202, Jan. 2009.

[38] M. F. Duarte, M. A. Davenport, D. Takhar, J. N. Laska, K. F. Kelly, and R. G. Baraniuk, "Single-Pixel Imaging via Compressive Sampling," *IEEE Signal Process. Mag.*, vol. 25, no. 2, pp. 83–91, Mar. 2008.

[39] M. B. Wakin, J. N. Laska, M. F. Duarte, D. Baron, S. Sarvotham, D. Takhar, K. F. Kelly, and R. G. Baraniuk, "AN ARCHITECTURE FOR COMPRESSIVE IMAGING Michael B. Wakin, Jason N. Laska, Marco F Duarte, Dror Baron Shriram Sarvotham, Dharmpal," *Current*, pp. 1273–1276, 2006.

[40] M. Pavlović, F. L.-J. de Physique, and undefined 1970, "Étude d'une nouvelle méthode permettant d'orienter, par pompage optique, des niveaux atomiques excités. Application à la mesure de la structure hyperfine de," *jphys.journaldephysique.org*.

[41] P. Jacquinot, "The Luminosity of Spectrometers with Prisms, Gratings, or Fabry-Perot Etalons," *J. Opt. Soc. Am.*, vol. 44, no. 10, p. 761, 1954.

[42] S. Ashkenazi, Y. Hou, T. Buma, and M. O'Donnell, "Optoacoustic imaging using thin polymer étalon," *Appl. Phys. Lett.*, vol. 86, no. 13, p. 134102, Mar. 2005.

[43] T. B. Jr, J. U.-O. communications, and undefined 1983, "Solid Fabry-Perot etalons for x-rays," *Elsevier*.

[44] J. V.-L. electronics/2nd edition/, by J. Verdeyen, and undefined 1989, "Laser electronics," *adsabs.harvard.edu*.

[45] M. S. Ünlü and S. Strite, "Resonant cavity enhanced photonic devices," *J. Appl. Phys.*, vol. 78, no. 2, pp. 607–639, Jul. 1995.

[46] J. A.-A. optics and undefined 1982, "Phase retardance of periodic multilayer mirrors," *osapublishing.org*.

[47] P. Zalicki and R. N. Zare, "Cavity ring-down spectroscopy for quantitative absorption measurements," *J. Chem. Phys.*, vol. 102, no. 7, pp. 2708–2717, Feb. 1995.

[48] M. Wheeler, S. Newman, … A. O.-E.-J. of the, and undefined 1998, "Cavity ring-down spectroscopy," *pubs.rsc.org*.

[49] G. Berden, R. Peeters, and G. Meijer, "Cavity ring-down spectroscopy: Experimental schemes and applications," *Int. Rev. Phys. Chem.*, vol. 19, no. 4, pp. 565–607, Oct. 2000.

[50] A. Abramovici, W. Althouse, R. Drever, Y. Gürsel, S. Kawamura, F. Raab, D. Shoemaker, L. Sievers, R. Spero, K. Thorne, R. Vogt, R. Weiss, S. Whitcomb, and M. Zucker, "LIGO: The Laser Interferometer Gravitational-Wave Observatory," *Science (80-.).*, vol. 256, no. 5055, pp. 325–333, 1719.

[51] B. P. Abbott, R. Abbott, T. D. Abbott, F. Acernese, K. Ackley, C. Adams, T. Adams, P. Addesso, R. X. Adhikari, V. B. Adya, C. Affeldt, M. Afrough, B. Agarwal, M. Agathos, K. Agatsuma, N. Aggarwal, O. D. Aguiar, L. Aiello, A. Ain, P. Ajith, B. Allen, G. Allen, A. Allocca, P. A. Altin, A. Amato, A. Ananyeva, S. B. Anderson, W. G. Anderson, S. Antier, S. Appert, K. Arai, M. C. Araya, J. S. Areeda, N. Arnaud, K. G. Arun, S. Ascenzi, G. Ashton, M. Ast, S. M. Aston, P. Astone, P. Aufmuth, C. Aulbert, K. AultONeal, A. Avila-Alvarez, S. Babak, P. Bacon, M. K. M. Bader, S. Bae, P. T. Baker, F. Baldaccini, G. Ballardin, S. W. Ballmer, S. Banagiri, J. C. Barayoga, S. E. Barclay, B. C. Barish, D. Barker, F. Barone, B. Barr, L. Barsotti, M. Barsuglia, D. Barta, J. Bartlett, I. Bartos, R. Bassiri, A. Basti, J. C. Batch, C. Baune, M. Bawaj, M. Bazzan, B. Bécsy, C. Beer, M. Bejger, I. Belahcene, A. S. Bell, B. K. Berger, G. Bergmann, C. P. L. Berry, D. Bersanetti, A. Bertolini, J. Betzwieser, S. Bhagwat, R. Bhandare, I. A. Bilenko, G. Billingsley, C. R. Billman, J. Birch, R. Birney, O. Birnholtz, S. Biscans, A. Bisht, M. Bitossi, C. Biwer, M. A. Bizouard, J. K. Blackburn, J. Blackman, C. D. Blair, D. G. Blair, R. M. Blair, S. Bloemen, O. Bock, N. Bode, M. Boer, G. Bogaert, A. Bohe, F. Bondu, R. Bonnand, B. A. Boom, R. Bork, V. Boschi, S. Bose, Y. Bouffanais, A. Bozzi, C. Bradaschia, P. R. Brady, V. B. Braginsky, M. Branchesi, J. E. Brau, T. Briant, A. Brillet, M. Brinkmann, V. Brisson, P. Brockill, J. E. Broida, A. F. Brooks, D. A. Brown, D. D. Brown, N. M. Brown, S. Brunett, C. C. Buchanan, A. Buikema, T. Bulik, H. J. Bulten, A. Buonanno, D. Buskulic, C. Buy, R. L. Byer, M. Cabero, L. Cadonati, G. Cagnoli, C. Cahillane, J. Calderón Bustillo, T. A. Callister, E. Calloni, J. B. Camp, M. Canepa, P. Canizares, K. C. Cannon, H. Cao, J. Cao, C. D. Capano, E. Capocasa, F. Carbognani, S. Caride, M. F. Carney, J. Casanueva Diaz, C. Casentini, S. Caudill, M. Cavaglià, F. Cavalier, R. Cavalieri, G. Cella, C. B. Cepeda, L. Cerboni Baiardi, G. Cerretani, E. Cesarini, S. J. Chamberlin, M. Chan, S. Chao, P. Charlton, E. Chassande-Mottin, D. Chatterjee, K. Chatziioannou, B. D. Cheeseboro, H. Y. Chen, Y. Chen, H.-P. Cheng, A. Chincarini, A.

Chiummo, T. Chmiel, H. S. Cho, M. Cho, J. H. Chow, N. Christensen, Q. Chu, A. J. K. Chua, S. Chua, A. K. W. Chung, S. Chung, G. Ciani, R. Ciolfi, C. E. Cirelli, A. Cirone, F. Clara, J. A. Clark, F. Cleva, C. Cocchieri, E. Coccia, P.-F. Cohadon, A. Colla, C. G. Collette, L. R. Cominsky, M. Constancio, L. Conti, S. J. Cooper, P. Corban, T. R. Corbitt, K. R. Corley, N. Cornish, A. Corsi, S. Cortese, C. A. Costa, M. W. Coughlin, S. B. Coughlin, J.-P. Coulon, S. T. Countryman, P. Couvares, P. B. Covas, E. E. Cowan, D. M. Coward, M. J. Cowart, D. C. Coyne, R. Coyne, J. D. E. Creighton, T. D. Creighton, J. Cripe, S. G. Crowder, T. J. Cullen, A. Cumming, L. Cunningham, E. Cuoco, T. Dal Canton, S. L. Danilishin, S. D'Antonio, K. Danzmann, A. Dasgupta, C. F. Da Silva Costa, V. Dattilo, I. Dave, M. Davier, D. Davis, E. J. Daw, B. Day, S. De, D. DeBra, E. Deelman, J. Degallaix, M. De Laurentis, S. Deléglise, W. Del Pozzo, T. Denker, T. Dent, V. Dergachev, R. De Rosa, R. T. DeRosa, R. DeSalvo, J. Devenson, R. C. Devine, S. Dhurandhar, M. C. Díaz, L. Di Fiore, M. Di Giovanni, T. Di Girolamo, A. Di Lieto, S. Di Pace, I. Di Palma, F. Di Renzo, Z. Doctor, V. Dolique, F. Donovan, K. L. Dooley, S. Doravari, I. Dorrington, R. Douglas, M. Dovale Álvarez, T. P. Downes, M. Drago, R. W. P. Drever, J. C. Driggers, Z. Du, M. Ducrot, J. Duncan, S. E. Dwyer, T. B. Edo, M. C. Edwards, A. Effler, H.-B. Eggenstein, P. Ehrens, J. Eichholz, S. S. Eikenberry, R. A. Eisenstein, R. C. Essick, Z. B. Etienne, T. Etzel, M. Evans, T. M. Evans, M. Factourovich, V. Fafone, H. Fair, S. Fairhurst, X. Fan, S. Farinon, B. Farr, W. M. Farr, E. J. Fauchon-Jones, M. Favata, M. Fays, H. Fehrmann, J. Feicht, M. M. Fejer, A. Fernandez-Galiana, I. Ferrante, E. C. Ferreira, F. Ferrini, F. Fidecaro, I. Fiori, D. Fiorucci, R. P. Fisher, R. Flaminio, M. Fletcher, H. Fong, P. W. F. Forsyth, S. S. Forsyth, J.-D. Fournier, S. Frasca, F. Frasconi, Z. Frei, A. Freise, R. Frey, V. Frey, E. M. Fries, P. Fritschel, V. V. Frolov, P. Fulda, M. Fyffe, H. Gabbard, M. Gabel, B. U. Gadre, S. M. Gaebel, J. R. Gair, L. Gammaitoni, M. R. Ganija, S. G. Gaonkar, F. Garufi, S. Gaudio, G. Gaur, V. Gayathri, N. Gehrels, G. Gemme, E. Genin, A. Gennai, D. George, J. George, L. Gergely, V. Germain, S. Ghonge, A. Ghosh, A. Ghosh, S. Ghosh, J. A. Giaime, K. D. Giardina, A. Giazotto, K. Gill, L. Glover, E. Goetz, R. Goetz, S. Gomes, G. González, J. M. Gonzalez Castro, A. Gopakumar, M. L. Gorodetsky, S. E. Gossan, M. Gosselin, R. Gouaty, A. Grado, C. Graef, M. Granata, A. Grant, S. Gras, C. Gray, G. Greco, A. C. Green, P. Groot, H. Grote, S. Grunewald, P. Gruning, G. M. Guidi, X. Guo, A. Gupta, M. K. Gupta, K. E. Gushwa, E. K. Gustafson, R. Gustafson, B. R. Hall, E. D. Hall, G. Hammond, M. Haney, M. M. Hanke, J. Hanks, C. Hanna, M. D. Hannam, O. A. Hannuksela, J. Hanson, T. Hardwick, J. Harms, G. M. Harry, I. W. Harry, M. J. Hart, C.-J. Haster, K. Haughian, J. Healy, A. Heidmann, M. C. Heintze, H. Heitmann, P. Hello, G. Hemming, M. Hendry, I. S. Heng, J. Hennig, J. Henry, A. W. Heptonstall, M. Heurs, S. Hild, D. Hoak, D. Hofman, K. Holt, D. E. Holz, P. Hopkins, C. Horst, J. Hough, E. A. Houston, E. J. Howell, Y. M. Hu, E. A. Huerta, D. Huet, B. Hughey, S. Husa, S. H. Huttner, T. Huynh-Dinh, N. Indik, D. R. Ingram, R. Inta, G. Intini, H. N. Isa, J.-M. Isac, M. Isi, B. R. Iyer, K. Izumi, T. Jacqmin, K. Jani, P. Jaranowski, S. Jawahar, F. Jiménez-Forteza, W. W. Johnson, N. K. Johnson-McDaniel, D. I. Jones, R. Jones, R. J. G. Jonker, L. Ju, J. Junker, C. V. Kalaghatgi, V. Kalogera, S. Kandhasamy, G. Kang, J. B. Kanner, S. Karki, K. S. Karvinen, M. Kasprzack, M. Katolik, E. Katsavounidis, W. Katzman, S. Kaufer, K. Kawabe, F. Kéfélian, D. Keitel, A. J. Kemball, R. Kennedy, C. Kent, J. S. Key, F. Y. Khalili, I. Khan, S. Khan, Z. Khan, E. A. Khazanov, N. Kijbunchoo, C. Kim, J. C. Kim, W. Kim, W. S. Kim, Y.-M. Kim, S. J. Kimbrell, E. J. King, P. J. King, R. Kirchhoff, J. S. Kissel, L.

Kleybolte, S. Klimenko, P. Koch, S. M. Koehlenbeck, S. Koley, V. Kondrashov, A. Kontos, M. Korobko, W. Z. Korth, I. Kowalska, D. B. Kozak, C. Krämer, V. Kringel, B. Krishnan, A. Królak, G. Kuehn, P. Kumar, R. Kumar, S. Kumar, L. Kuo, A. Kutynia, S. Kwang, B. D. Lackey, K. H. Lai, M. Landry, R. N. Lang, J. Lange, B. Lantz, R. K. Lanza, A. Lartaux-Vollard, P. D. Lasky, M. Laxen, A. Lazzarini, C. Lazzaro, P. Leaci, S. Leavey, C. H. Lee, H. K. Lee, H. M. Lee, H. W. Lee, K. Lee, J. Lehmann, A. Lenon, M. Leonardi, N. Leroy, N. Letendre, Y. Levin, T. G. F. Li, A. Libson, T. B. Littenberg, J. Liu, R. K. L. Lo, N. A. Lockerbie, L. T. London, J. E. Lord, M. Lorenzini, V. Loriette, M. Lormand, G. Losurdo, J. D. Lough, G. Lovelace, H. Lück, D. Lumaca, A. P. Lundgren, R. Lynch, Y. Ma, S. Macfoy, B. Machenschalk, M. MacInnis, D. M. Macleod, I. Magaña Hernandez, F. Magaña-Sandoval, L. Magaña Zertuche, R. M. Magee, E. Majorana, I. Maksimovic, N. Man, V. Mandic, V. Mangano, G. L. Mansell, M. Manske, M. Mantovani, F. Marchesoni, F. Marion, S. Márka, Z. Márka, C. Markakis, A. S. Markosyan, E. Maros, F. Martelli, L. Martellini, I. W. Martin, D. V. Martynov, J. N. Marx, K. Mason, A. Masserot, T. J. Massinger, M. Masso-Reid, S. Mastrogiovanni, A. Matas, F. Matichard, L. Matone, N. Mavalvala, R. Mayani, N. Mazumder, R. McCarthy, D. E. McClelland, S. McCormick, L. McCuller, S. C. McGuire, G. McIntyre, J. McIver, D. J. McManus, T. McRae, S. T. McWilliams, D. Meacher, G. D. Meadors, J. Meidam, E. Mejuto-Villa, A. Melatos, G. Mendell, R. A. Mercer, E. L. Merilh, M. Merzougui, S. Meshkov, C. Messenger, C. Messick, R. Metzdorff, P. M. Meyers, F. Mezzani, H. Miao, C. Michel, H. Middleton, E. E. Mikhailov, L. Milano, A. L. Miller, A. Miller, B. B. Miller, J. Miller, M. Millhouse, O. Minazzoli, Y. Minenkov, J. Ming, C. Mishra, S. Mitra, V. P. Mitrofanov, G. Mitselmakher, R. Mittleman, A. Moggi, M. Mohan, S. R. P. Mohapatra, M. Montani, B. C. Moore, C. J. Moore, D. Moraru, G. Moreno, S. R. Morriss, B. Mours, C. M. Mow-Lowry, G. Mueller, A. W. Muir, A. Mukherjee, D. Mukherjee, S. Mukherjee, N. Mukund, A. Mullavey, J. Munch, E. A. M. Muniz, P. G. Murray, K. Napier, I. Nardecchia, L. Naticchioni, R. K. Nayak, G. Nelemans, T. J. N. Nelson, M. Neri, M. Nery, A. Neunzert, J. M. Newport, G. Newton, K. K. Y. Ng, T. T. Nguyen, D. Nichols, A. B. Nielsen, S. Nissanke, A. Nitz, A. Noack, F. Nocera, D. Nolting, M. E. N. Normandin, L. K. Nuttall, J. Oberling, E. Ochsner, E. Oelker, G. H. Ogin, J. J. Oh, S. H. Oh, F. Ohme, M. Oliver, P. Oppermann, R. J. Oram, B. O'Reilly, R. Ormiston, L. F. Ortega, R. O'Shaughnessy, D. J. Ottaway, H. Overmier, B. J. Owen, A. E. Pace, J. Page, M. A. Page, A. Pai, S. A. Pai, J. R. Palamos, O. Palashov, C. Palomba, A. Pal-Singh, H. Pan, B. Pang, P. T. H. Pang, C. Pankow, F. Pannarale, B. C. Pant, F. Paoletti, A. Paoli, M. A. Papa, H. R. Paris, W. Parker, D. Pascucci, A. Pasqualetti, R. Passaquieti, D. Passuello, B. Patricelli, B. L. Pearlstone, M. Pedraza, R. Pedurand, L. Pekowsky, A. Pele, S. Penn, C. J. Perez, A. Perreca, L. M. Perri, H. P. Pfeiffer, M. Phelps, O. J. Piccinni, M. Pichot, F. Piergiovanni, V. Pierro, G. Pillant, L. Pinard, I. M. Pinto, M. Pitkin, R. Poggiani, P. Popolizio, E. K. Porter, A. Post, J. Powell, J. Prasad, J. W. W. Pratt, V. Predoi, T. Prestegard, M. Prijatelj, M. Principe, S. Privitera, G. A. Prodi, L. G. Prokhorov, O. Puncken, M. Punturo, P. Puppo, M. Pürrer, H. Qi, J. Qin, S. Qiu, V. Quetschke, E. A. Quintero, R. Quitzow-James, F. J. Raab, D. S. Rabeling, H. Radkins, P. Raffai, S. Raja, C. Rajan, M. Rakhmanov, K. E. Ramirez, P. Rapagnani, V. Raymond, M. Razzano, J. Read, T. Regimbau, L. Rei, S. Reid, D. H. Reitze, H. Rew, S. D. Reyes, F. Ricci, P. M. Ricker, S. Rieger, K. Riles, M. Rizzo, N. A. Robertson, R. Robie, F. Robinet, A. Rocchi, L. Rolland, J. G. Rollins, V. J. Roma, J. D. Romano, R. Romano, C. L. Romel, J. H. Romie, D. Rosińska, M. P. Ross, S. Rowan,

A. Rüdiger, P. Ruggi, K. Ryan, M. Rynge, S. Sachdev, T. Sadecki, L. Sadeghian, M. Sakellariadou, L. Salconi, M. Saleem, F. Salemi, A. Samajdar, L. Sammut, L. M. Sampson, E. J. Sanchez, V. Sandberg, B. Sandeen, J. R. Sanders, B. Sassolas, B. S. Sathyaprakash, P. R. Saulson, O. Sauter, R. L. Savage, A. Sawadsky, P. Schale, J. Scheuer, E. Schmidt, J. Schmidt, P. Schmidt, R. Schnabel, R. M. S. Schofield, A. Schönbeck, E. Schreiber, D. Schuette, B. W. Schulte, B. F. Schutz, S. G. Schwalbe, J. Scott, S. M. Scott, E. Seidel, D. Sellers, A. S. Sengupta, D. Sentenac, V. Sequino, A. Sergeev, D. A. Shaddock, T. J. Shaffer, A. A. Shah, M. S. Shahriar, L. Shao, B. Shapiro, P. Shawhan, A. Sheperd, D. H. Shoemaker, D. M. Shoemaker, K. Siellez, X. Siemens, M. Sieniawska, D. Sigg, A. D. Silva, A. Singer, L. P. Singer, A. Singh, R. Singh, A. Singhal, A. M. Sintes, B. J. J. Slagmolen, B. Smith, J. R. Smith, R. J. E. Smith, E. J. Son, J. A. Sonnenberg, B. Sorazu, F. Sorrentino, T. Souradeep, A. P. Spencer, A. K. Srivastava, A. Staley, M. Steinke, J. Steinlechner, S. Steinlechner, D. Steinmeyer, B. C. Stephens, S. P. Stevenson, R. Stone, K. A. Strain, G. Stratta, S. E. Strigin, R. Sturani, A. L. Stuver, T. Z. Summerscales, L. Sun, S. Sunil, P. J. Sutton, B. L. Swinkels, M. J. Szczepańczyk, M. Tacca, D. Talukder, D. B. Tanner, M. Tápai, A. Taracchini, J. A. Taylor, R. Taylor, T. Theeg, E. G. Thomas, M. Thomas, P. Thomas, K. A. Thorne, K. S. Thorne, E. Thrane, S. Tiwari, V. Tiwari, K. V. Tokmakov, K. Toland, M. Tonelli, Z. Tornasi, C. I. Torrie, D. Töyrä, F. Travasso, G. Traylor, D. Trifirò, J. Trinastic, M. C. Tringali, L. Trozzo, K. W. Tsang, M. Tse, R. Tso, D. Tuyenbayev, K. Ueno, D. Ugolini, C. S. Unnikrishnan, A. L. Urban, S. A. Usman, K. Vahi, H. Vahlbruch, G. Vajente, G. Valdes, M. Vallisneri, N. van Bakel, M. van Beuzekom, J. F. J. van den Brand, C. Van Den Broeck, D. C. Vander-Hyde, L. van der Schaaf, J. V. van Heijningen, A. A. van Veggel, M. Vardaro, V. Varma, S. Vass, M. Vasúth, A. Vecchio, G. Vedovato, J. Veitch, P. J. Veitch, K. Venkateswara, G. Venugopalan, D. Verkindt, F. Vetrano, A. Viceré, A. D. Viets, S. Vinciguerra, D. J. Vine, J.-Y. Vinet, S. Vitale, T. Vo, H. Vocca, C. Vorvick, D. V. Voss, W. D. Vousden, S. P. Vyatchanin, A. R. Wade, L. E. Wade, M. Wade, R. M. Wald, R. Walet, M. Walker, L. Wallace, S. Walsh, G. Wang, H. Wang, J. Z. Wang, M. Wang, Y.-F. Wang, Y. Wang, R. L. Ward, J. Warner, M. Was, J. Watchi, B. Weaver, L.-W. Wei, M. Weinert, A. J. Weinstein, R. Weiss, L. Wen, E. K. Wessel, P. Weßels, T. Westphal, K. Wette, J. T. Whelan, B. F. Whiting, C. Whittle, D. Williams, R. D. Williams, A. R. Williamson, J. L. Willis, B. Willke, M. H. Wimmer, W. Winkler, C. C. Wipf, H. Wittel, G. Woan, J. Woehler, J. Wofford, K. W. K. Wong, J. Worden, J. L. Wright, D. S. Wu, G. Wu, W. Yam, H. Yamamoto, C. C. Yancey, M. J. Yap, H. Yu, H. Yu, M. Yvert, A. Zadrożny, M. Zanolin, T. Zelenova, J.-P. Zendri, M. Zevin, L. Zhang, M. Zhang, T. Zhang, Y.-H. Zhang, C. Zhao, M. Zhou, Z. Zhou, X. J. Zhu, A. Zimmerman, M. E. Zucker, and J. Zweizig, "GW170104: Observation of a 50-Solar-Mass Binary Black Hole Coalescence at Redshift 0.2," *Phys. Rev. Lett.*, vol. 118, no. 22, p. 221101, Jun. 2017.

[52]   A. Lipson, S. Lipson, and H. Lipson, *Optical physics*. 2010.

[53]   E. D. Diebold, N. K. Hon, Z. Tan, J. Chou, T. Sienicki, C. Wang, and B. Jalali, "Giant tunable optical dispersion using chromo-modal excitation of a multimode waveguide," *Opt. Express*, vol. 19, no. 24, p. 23809, 2011.

[54]   Y. I. Yang, Y. I. Yang, and E. Engineering, "Gray-Scale Electron-Beam Lithography."

[55]   J. Kim, D. Joy, S. L.-M. Engineering, and undefined 2007, "Controlling resist thickness

and etch depth for fabrication of 3D structures in electron-beam grayscale lithography," *Elsevier*.

[56]   A. Schleunitz and H. Schift, "Fabrication of 3D nanoimprint stamps with continuous reliefs using dose-modulated electron beam lithography and thermal reflow," *J. Micromechanics Microengineering*, vol. 20, no. 9, p. 95002, Sep. 2010.

[57]   F. Hu, S. L.-J. of V. S. & T. B, and undefined 2003, "Dose control for fabrication of grayscale structures using a single step electron-beam lithographic process," *avs.scitation.org*.

[58]   W. Yu, X. Y.-O. express, and undefined 2003, "Fabrication of refractive microlens in hybrid SiO2/TiO2 sol-gel glass by electron beam lithography," *osapublishing.org*.

[59]   S. Lee, K. A.-J. of V. S. & T. B, and undefined 2007, "Accurate control of remaining resist depth for nanoscale three-dimensional structures in electron-beam grayscale lithography," *avs.scitation.org*.

[60]   M. Born and E. Wolf, *Principles of optics : electromagnetic theory of propagation, interference and diffraction of light*. Cambridge University Press, 1999.

[61]   F. R. S. L. Rayleigh, "XXXI. *Investigations in optics, with special reference to the spectroscope*," *London, Edinburgh, Dublin Philos. Mag. J. Sci.*, vol. 8, no. 49, pp. 261–274, Oct. 1879.

[62]   J. Gelles, B. J. Schnapp, and M. P. Sheetz, "Tracking kinesin-driven movements with nanometre-scale precision," *Nature*, vol. 331, no. 6155, pp. 450–453, Feb. 1988.

[63]   A. . van Oijen, J. Köhler, J. Schmidt, M. Müller, and G. . Brakenhoff, "3-Dimensional super-resolution by spectrally selective imaging," *Chem. Phys. Lett.*, vol. 292, no. 1–2, pp. 183–187, Jul. 1998.

[64]   R. E. Thompson, D. R. Larson, and W. W. Webb, "Precise nanometer localization analysis for individual fluorescent probes.," *Biophys. J.*, vol. 82, no. 5, pp. 2775–2783, 2002.

[65]   A. Yildiz, "Myosin V Walks Hand-Over-Hand: Single Fluorophore Imaging with 1.5-nm Localization," *Science (80-.).*, vol. 300, no. 5628, pp. 2061–2065, Jun. 2003.

[66]   "ZEISS Microscopy Online Campus | Introduction to Superresolution Microscopy." [Online]. Available: http://zeiss-campus.magnet.fsu.edu/articles/superresolution/introduction.html. [Accessed: 10-Mar-2018].

[67]   A. Labno, C. Gladden, J. Kim, D. Lu, X. Yin, Y. Wang, and Z. L.- Nanophotonics, "Three-dimensional nanoscale imaging by plasmonic Brownian microscopy," *degruyter.com*.

[68]   A. Labno, C. Gladden, J. Kim, D. Lu, X. Yin, Y. Wang, Z. Liu, and X. Zhang, "Letter Three-dimensional nanoscale imaging by plasmonic Brownian microscopy," *Nanophotonics*, vol. 7, no. 2, pp. 489–495, 2018.

[69]   A. Einstein, *Investigations on the Theory of the Brownian Movement*. 1956.

[70]   M. A. van Dijk, A. L. Tchebotareva, M. Orrit, M. Lippitz, S. Berciaud, D. Lasne, L. Cognet, and B. Lounis, "Absorption and scattering microscopy of single metal nanoparticles," *Phys. Chem. Chem. Phys.*, vol. 8, no. 30, p. 3486, Jul. 2006.

[71]   P. K. Jain, K. S. Lee, I. H. El-Sayed, and M. A. El-Sayed, "Calculated absorption and scattering properties of gold nanoparticles of different size, shape, and composition: Applications in biological imaging and biomedicine," *J. Phys. Chem. B*, vol. 110, pp. 7238–7248, 2006.

[72]   C. V.-O. letters and undefined 1977, "External-cavity-controlled 32-MHz narrow-band cw GaAlAs-diode lasers," *osapublishing.org*.

[73]   M. Fleming, A. M.-I. J. of Q. Electronics, and undefined 1981, "Spectral characteristics of external-cavity controlled semiconductor lasers," *ieeexplore.ieee.org*.

[74]   F. Duarte, *Tunable lasers handbook*. 1996.

[75]   A. Arnold, J. Wilson, M. B.-R. of Scientific, and undefined 1998, "A simple extended-cavity diode laser," *aip.scitation.org*.

[76]   L. Ricci, M. Weidemüller, T. Esslinger, A. H.-… Communications, and undefined 1995, "A compact grating-stabilized diode laser system for atomic physics," *Elsevier*.

[77]   M. G. Littman and H. J. Metcalf, "Spectrally narrow pulsed dye laser without beam expander."

[78]   T. Suzuki, R. Nagai, O. Sasaki, and S. Choi, "Rapid wavelength scanning based on acousto-optically tuned external-cavity laser diode," *OPTICS*, vol. 284, no. 19, pp. 4615–4618, 2011.

[79]   T. Suzuki, S. Abe, S. C.-O. S. D. 2015, and undefined 2015, "Two-dimensional thickness measurement using acousto-optically tuned external cavity laser diode," *spiedigitallibrary.org*.

[80]   E. Huang, Q. Ma, and Z. Liu, "Spectrum Engineering for Reconstructive Spectroscopy," in *CLEO: Applications and Technology*, 2016, p. AM1J--7.

[81]   S. H. Kong, D. D. L. Wijngaards, and R. F. Wolffenbuttel, "Infrared micro-spectrometer based on a diffraction grating," *Sensors and Actuators a-Physical*, vol. 92, no. 1–3, pp. 88–95, 2001.

[82]   X. Gan, N. Pervez, I. Kymissis, F. Hatami, and D. Englund, "A high-resolution spectrometer based on a compact planar two dimensional photonic crystal cavity array," *Appl. Phys. Lett.*, vol. 100, no. 23, 2012.

[83]   S.-W. Wang, C. Xia, X. Chen, W. Lu, M. Li, H. Wang, W. Zheng, and T. Zhang, "Concept of a high-resolution miniature spectrometer using an integrated filter array.," *Opt. Lett.*, vol. 32, no. 6, pp. 632–634, 2007.

[84]   J. Bao and M. G. Bawendi, "A colloidal quantum dot spectrometer," *Nature*, vol. 523, no. 7558, pp. 67–70, 2015.

[85] T. Yang, C. Xu, H. Ho, Y. Zhu, X. Hong, Q. Wang, Y. Chen, X. Li, X. Zhou, M. Yi, and W. Huang, "Miniature spectrometer based on diffraction in a dispersive hole array," *Opt. Lett.*, vol. 40, no. 13, pp. 3217–3220, 2015.

[86] C.-C. Chang and H.-N. Lee, "On the estimation of target spectrum for filter-array based spectrometers," *Opt. Express*, vol. 16, no. 2, pp. 1056–1061, 2008.

[87] J. Oliver, W. Lee, S. Park, and H. Lee, "Improving resolution of miniature spectrometers by exploiting sparse nature of signals.," *Opt. Express*, vol. 20, no. 3, pp. 2613–25, 2012.

[88] M. K. Yetzbacher, C. W. Miller, a. J. Boudreau, M. Christophersen, and M. J. Deprenger, "Multiple-order staircase etalon spectroscopy," *SPIE Sens. Technol. Appl.*, vol. 9101, p. 910104, 2014.

[89] E. Huang, Q. Ma, and Z. Liu, "Etalon Array Reconstructive Spectrometry," *Sci. Rep.*, vol. 7, p. 40693, 2017.